THE JOURNAL OF THE INSTITUTION OF ENGINEERS, MALAYSIA

KDN PP5476/10/2012 (030203)
ISSN 0126-513X
Vol. 72, No.4
December 2011

IEM JOURNAL

Vol. 72, No. 4, December 2011
KDN PP5476/10/2012 (030203) ISSN 0126-513X

CONTENTS

THE INSTITUTION OF ENGINEERS, MALAYSIA
Bangunan Ingenieur, Lots 60 & 62, Jalan 52/4,
P.O.Box 223 (Jalan Sultan),
46720 Petaling Jaya, Selangor Darul Ehsan.
Tel: 03-7968 4001/4002
Fax: 03-7957 7678
E-mail: sec@iem.org.my Homepage: http://www.myiem.org.my

Printed by: WISE ORGANISATION (M) SDN. BHD. (888671-H)
No. 5, Jalan Industri PBP 11, Taman Industri Pusat Bandar Puchong,
47100 Puchong, Selangor Darul Ehsan.
Tel: 603-5891 7363 Fax: 603-5891 7232
E-mail: weprint.wise@gmail.com

PRINT QUANTITY: *5,500 Copies*

INVESTIGATION BEST NUMBER OF TANKS FOR HYDROLOGICAL TANK MODEL FOR RURAL CATCHMENT IN HUMID REGION

(Date received:29.6.2010/Date accepted:3.8.2011)

Kuok King Kuok[1], Sobri Harun[2] and Po-Chan Chiu[3]

[1,2]Department of Hydraulics and Hydrology, Faculty of Civil Engineering,
Universiti Teknologi Malaysia,81310 UTM, Johor
[3]Department of Information Systems, Faculty of Computer Science and Information Technology,
Universiti Malaysia Sarawak, 97000 Samarahan, Sarawak
E-mail: [1]kelvinkuok100@gmail.com

ABSTRACT

Hydrological Tank model has proven more capable than many other models in modeling the hydrologic responses from a wide range of humid watershed. Many hydrologists are using this model due to its simplicity of concept and computation while achieving forecasting accuracy comparable with more sophisticated models. Throughout the years, various types of Tank model have been developed. The best was found to be storages series type. However, there is no general agreement regarding the best number of series storage tanks for rural catchment in humid region. In this study, three types of series storage tanks were selected to model the daily and hourly runoff for Bedup Basin, a rural catchment in humid region. These three Tank models that consist of three, four and five series storages tanks are named as 3-Tank-D, 4-Tank-D, 5-Tank-D respectively for daily model, and 3-Tank-H, 4-Tank-H, 5-Tank-H respectively for hourly model. The model performance is evaluated with coefficient of correlation (R) and Nash-sutcliffe coefficient (E^2). Results revealed that the best number of tank is four, where average R and E^2 yield to 0.6833 and 0.6620 respectively for daily runoff simulation, 0.8985 and 0.8214 respectively for hourly runoff simulation. Besides, sensitivity analysis also demonstrated the infiltration coefficient from forth to fifth tank (C9) has minor impact to runoff peak discharge and side outlet coefficient for fifth tank (C10) doesn't have any significant impact to runoff peak discharge for both daily and hourly runoff simulation. Thus, these two parameters can be ignored. This result further confirmed that the best number of tanks for daily and hourly runoff simulation for rural catchment in humid region is four.

Keywords: *Coefficient of Correlation (R), Conceptual Rainfall-runoff Model, Hydrological Tank Model, Nash-Sutcliffe Coefficient (E^2)*

1.0 INTRODUCTION

Hydrologic Tank model, a conceptual rainfall-runoff (CRR) model, was developed by Sugawara and Funiyuki (1956)[1]. It consists of a set of linear storages in series or parallel with side and bottom outlets. This CRR model presents the complicated and nonlinearity of rainfall-runoff processes through interconnected storages and simple equations to represent the water movement among the storages tanks.

Tank model has proven more capable than many other models in modeling the hydrologic responses from a wide range of humid watershed. Many hydrologists are using this model [2-5] due to its simple analytical structure and computation while achieving forecasting accuracy comparable with more sophisticated models. Department of Irrigation and Drainage Malaysia (DID) [6] used Tank model to forecast flood levels of the Kelantan River at the Guillemard Bridge during the Northeast Monsoon. Huang *et al.* (2006)[7] applied Tank model for application of middleware technique in web of flood forecasting System of Gan River, JiangXi province, China. Sothea *et al.* (2006)[8] applied the "3*4+1" type Tank model to calculate the runoff of the Lower Mekong River Basin from Chiang Saen to Kompong Cham and its sub catchments at Mekong Delta, Cambodia. Besides, Chen and Barry (2006) [9] coupled semidistributed Tank model with ANNs to explore the nonlinear transformation of the runoff generated from the individual subcatchments into the total runoff at the entire Miyun reservoir outlet, Beijing, China. However, Tank model is not designed to use parameters that are directly measured in field. Their parameters are usually obtained by calibration.

Prior conducting the calibration process, the structure and the best number of tanks for Hydrological Tank model for the study area need to be determined. The determination of best number of tanks will ensure and lead to the best fit between the observed and estimated flow hydrograph. As review back the history of Tank model, Sugawara (1957)[10] had developed various types of Tank model to derive discharge from precipitation. Among the types of Tank model developed are a) Exponential Type, b) Parallel Exponential Type, c) Overflow Type, d) Storage Type and e) Series Storage Type. Sugawara (1957)[10] proclaimed that the best type of model was the series storage type Tank model.

The original development of the model was based on the assumption that two water storage tanks were required to represent both surface runoff and intermediate runoff. Despite the original Tank model is generally considered to be lacking of physical meaning, as the model undergoes various developments, the physics of the model has been enhanced. The evolution of the Tank model has occurred over decades and variations of the model have been proposed.

In the subsequent development of the model (Sugawara 1967)[2], four storages tank were introduced. According to this configuration, runoff generated from side outlets of the top tank is considered as surface runoff, runoff from the second tank as intermediate runoff, whereas runoff generated from the side outlets of the third and fourth tanks are referred to subbase runoff and base flow, respectively.

Besides, Sugawara (1974)[11] also proposed the 4*4 type Tank model to be applied for the watershed having dry season. The model also modified by Sothea *et al.* (2006)[3] to form the "3*4+1" type Tank model to forecast the flow at Lower Mekong River Basin, Cambodia. Meanwhile, Sugawara (1984)[4] also further developed the Tank model with including the snow component. In an attempt to consider variations in soil moisture content especially in the arid or semiarid areas, additional structures were added to the bottom layer of the top tank to represent effect of the primary and secondary soil moisture storage [5].

Meanwhile, Cooper *et. al.* (1997 and 2007)[12, 13] had calibrated 2-Tank series storage type to simulate runoff in Canada. A simple 2-Tank model with an upper and lower tank was also used by Chen and Barry (2006)[9] for simulating surface and groundwater generation. Concurrently, used four-layered Tank model for simulating runoff in their respective studies [14-21].

From that above statement, there is no general agreement among the researchers the best and appropriate number of tanks for simulating runoff accurately. Therefore, the present study was undertaken to determine the best number of tanks of Tank model that provide reliable and accurate estimates of runoff for rural catchment in humid region. Manual trial and error method is selected for Tank model calibration.

2.0 STUDY AREA

The selected study area is Sungai Bedup Basin in humid region. It is located at upper stream of Batang Sadong where tidal is unreachable. The basin area is approximately 47.5 km^2 and the elevation varies from 8m to 686m above mean sea level [22]. The vegetation cover is mainly of shrubs, low plant and forest. Sungai Bedup's basin has a dendritic type channel system. The maximum stream length for the basin is approximately 10km, which is measured from the most remote area point of the stream to the basin outlet.

This basin is selected as there are five rainfall stations within the catchment and a water level stations at basin outlet. The historical long series, good quality rainfall and water level data are available since 1977. Moreover, the rating curve for Bedup Basin is available from Department of Irrigation and Drainage (DID) Sarawak [6].

The locality plan of Sungai Bedup Basin was presented in Figure 1. Figure 1a shows the location of Sadong Basin. Main boundary of the Sadong Basin, rainfall and river stage gauging stations within Sadong Basin, are shown in Figure 1b. Figure 1c presents the 5 rainfall gauging stations available in Sungai Bedup Basin, namely, Bukit Matuh (BM), Semuja Nonok (SN), Sungai Busit (SB), Sungai Merang (SM) and Sungai Teb (ST), and one river stage gauging station at Sungai Bedup located at the outlet of the basin.

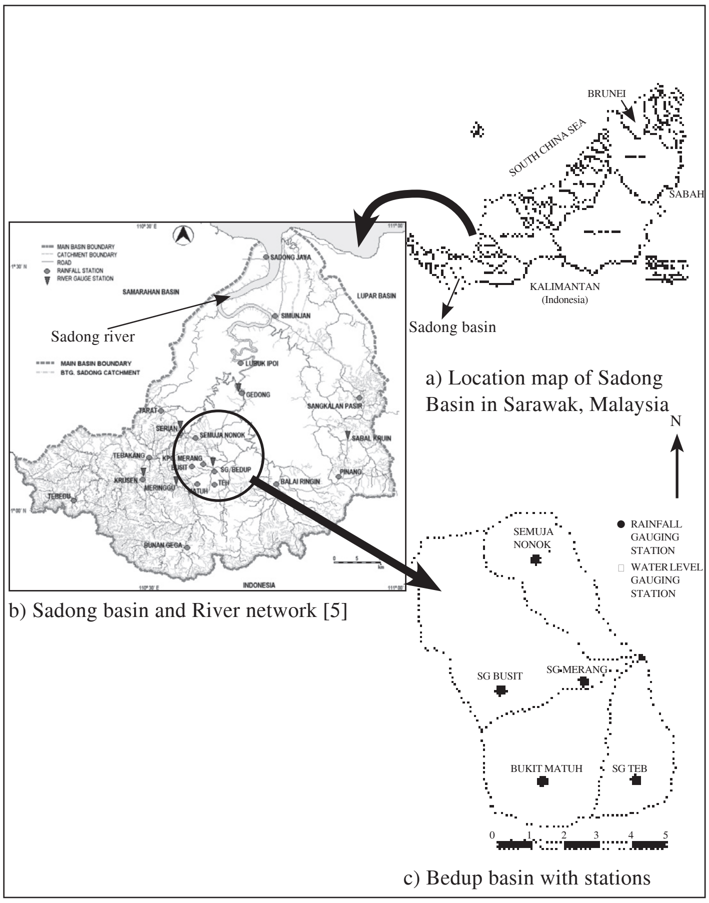

Figure 1: Locality map of Bedup basin, sub-basin of Sadong basin, Sarawak, Malaysia

For Tank model calibration, the input data used are weighted areal daily or hourly rainfall data obtained from Thiessen Polygon Analysis. The daily or hourly rainfall data from the 5 rainfall stations are processed, formatted and fed into the Thiessen Polygon analysis worksheet to calculate an weighted areal rainfall throughout the catchment. The area weighted precipitation for BM, SN, SB, SM, ST are found to be 0.17, 0.16, 0.17, 0.18 and 0.32 respectively. The weighted areal daily or hourly rainfall data for that time step is then fed into the Tank model. The calibrated Tank model will then carry out computations to simulate the daily or hourly discharges for Bedup Outlet.

3.0 SELECTION NUMBER OF TANKS

Since different catchment required different number of tanks for flow simulation, it is important to find the most suitable and appropriate Tank model for the study catchment. Through preliminary study, 2-Tank model was found unable to simulate runoff accurately for rural catchment in humid region. Thus, the investigation of 2-Tank model was not presented in this study. 3 types of series storage Tank models selected for manual calibration are named as 3-Tank, 4-Tank and 5-Tank. Specifically, 3-Tank-D, 4-Tank-D, 5-Tank-D for daily runoff simulation and 3-Tank-H, 4-Tank-H, 5-Tank-H for hourly runoff simulation. The schematic diagrams for investigated 3-Tank, 4-Tank and 5-Tank models are presented in Figures 2, 3 and 4 respectively. The complexity of Tank model increased as the number of tanks increased from 3 to 5. 10 parameters need to be calibrated for 3-Tank model are named as C1, C2, C3, C4, C5, C6, X1, X2, X3 and X4. Meanwhile, the parameters calibrated for 4-Tank model are C1, C2, C3, C4, C5, C6, C7, C8, X1, X2, X3, X4 and X5. Besides, 16 parameters are calibrated for 5-Tank model namely C1, C2, C3, C4, C5, C6, C7, C8, C9, C10, X1, X2, X3, X4, X5 and X6. However, the values for X3, X4, X5 and X6 always found to be 0 through preliminary study. Thus, these parameters are not calibrated for investigation of best number of tank for rural catchment in humid region. The description of Tank model parameters are presented in Table 1.

Table 1: Description of tank model parameters

Parameters	Description
C1	Site outlet coefficient No.1 for first tank
C2	Site outlet coefficient No.2 for first tank
C3	Infiltration coefficient from first tank to second tank
C4	Site outlet coefficient for second tank
C5	Infiltration coefficient from second to third tank
C6	Site outlet coefficient for third tank
C7	Infiltration coefficient from third to forth tank
C8	Site outlet coefficient for forth tank
C9	Infiltration coefficient from forth to fifth tank
C10	Site outlet coefficient for fifth tank
X1	Height of side outlet No.1 for first tank
X2	Height of side outlet No.2 for first tank
X3	Height of side outlet for second tank
X4	Height of side outlet for third tank
X5	Height of side outlet for forth tank
X6	Height of side outlet for fifth tank

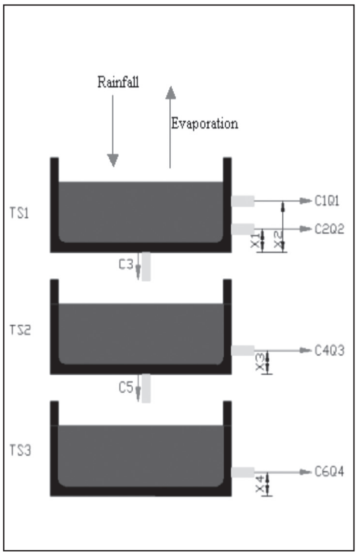

Figure 2: Schematic diagram of 3-Tank model

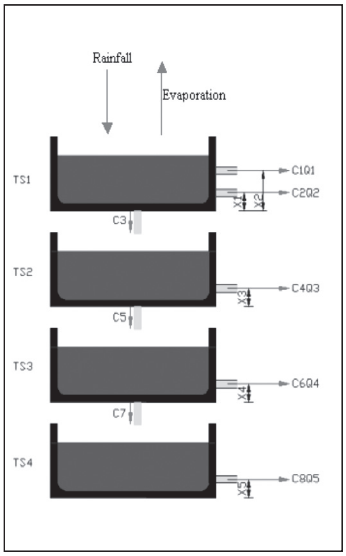

Figure 3: Schematic diagram of 4-Tank model

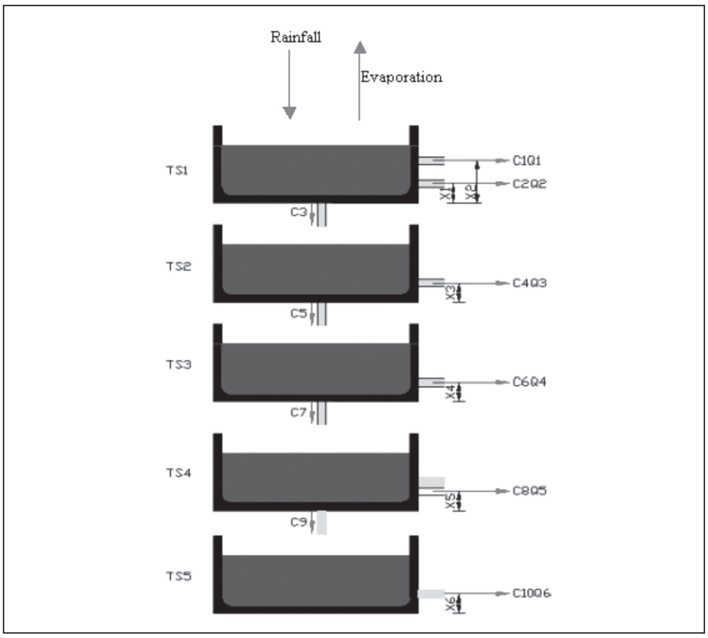

Figure 4: Schematic diagram of 5-Tank model

4.0 METHODOLOGY

4.1 Model Development and Learning Mechanism

In general, the model development for both daily and hourly runoff simulation can be categorised into calibration stage and validation stage. During calibration stage, a pair of rainfall runoff data was calibrated to search for the optimal parameters through trial and error method. The optimal parameters obtained are validated using different pairs of rainfall-runoff data to ensure the parameters obtained will provide the best fit between the observed and simulated runoff.

Daily rainfall-runoff data from January to March 2000 in Table 1 is used for model calibration. The optimal parameters obtained are then validated with three different pairs of daily rainfall-runoff data dated April to June 2000, July to September 2000 and October to November 2000 as tabulated in Table 2.

Table 2: Daily calibration and validation data used for determining best number of tanks

Item	Data Period	Data Description
1	Jan to Mar 2000	Calibration
2	Apr to Jun 2000	Validation
3	Jul to Sep 2000	Validation
4	Oct to Nov 2000	Validation

Similarly for hourly Tank model calibration and validation, the optimal number of tank was calibrated and validated using the data as shown in Table 3. Hourly data from 1 to 7 January 1999 in Table 3 is used for model calibration. The validation data used are Items 2 to 8 as presented in Table 2.

Table 3: Hourly calibration and validation data used for determining best number of tanks

Item	Data Period	Data Description
1	1-7 Jan 99	Calibration
2	5-8 Apr 99	Validation
3	5-8 Feb 99	Validation
4	8-12 Aug 98	Validation
5	9-12 Sep 98	Validation
6	15-18 Mar 99	Validation
7	20-24 Jan 99	Validation
8	26-31 Jan 99	Validation

4.2 Sensitivity Analysis

Sensitivity analysis is important for better understanding and estimating values and thus reduced uncertainty [23]. Knowing the sensitivity of parameters can also reduced the time spent on the non-sensitive one. Therefore, sensitivity analysis is an technique used for the assessment of the input parameters with respect to their impact on model output, which is useful not only for model development, but also for model validation and reduction of uncertainty[24].

In this study, sensitivity analysis is conducted for 3-Tank, 4-Tank and 5-Tank models for both daily and hourly runoff simulation. The parameters investigated for 3-Tank model are C1, C2, C3, C4, C5, C6, X1 and X2. Meanwhile, the sensitivity for C1, C2, C3, C4, C5, C6, C7, C8, X1 and X2 are investigated for 4-Tank model. Subsequently, 12 parameters named as C1, C2, C3, C4, C5, C6, C7, C8, C9, C10, X1 and X2 are investigated for 5-Tank model.

While conducting the sensitivity analysis, the parameter investigated is changing from ±5%, ±10%, ±20%, ±30%, ±50% to ±75%, while the other parameters are remained constant. The effect of each parameters investigated to model outputs are recorded. The sensitivity for daily runoff is analysed based on coefficient of correlation (R) and Nash-Sutcliffe coefficient (E^2) values, whereas sensitivity analysis for hourly runoff is based on the runoff peak discharge.

4.3 Performance Criteria

R and E^2 will measure the overall differences between the simulated and observed runoff. R and E^2 values of 1.0 implies a perfect fit. The formulas of these two coefficients are given in Table 4.

Table 4: Statistics for model comparison

Coefficient	Symbol	Formula
Coefficient of Correlation	R	$\frac{\sum (obs - \overline{obs})(pred - \overline{pred})}{\sqrt{\sum (obs - \overline{obs})^2 \sum (pred - \overline{pred})^2}}$
Nash-Sutcliffe Coefficient	E^2	$E^2 = 1 - \frac{\sum_{i}^{j} (obs - pred)^2}{\sum_{k^i}^{j} (obs - \overline{obs})^2}$

where obs = observed value, pred = predicted value, $\overline{obs}$ = mean observed values, $\overline{pred}$ = mean predicted values and j = number of values.

Besides, the formula for peak discharge is presented is Equation 1.

$$\textit{runoff\_peak\_discharge} = \frac{\textit{simulated\_peak\_observed\_peak}}{\textit{observed\_peak}} \times 100\% \qquad (1)$$

5.0 RESULTS AND DISCUSSION

5.1 Determination Number of Tank for Daily Runoff

Table 5 shows the optimum parameters obtained for 3-Tank-D, 4-Tank-D and 5-Tank-D using trial and error method. The performance of different configuration of Tank model as validated with three different time periods is presented in Table 6. Figure 5 presents comparison between observed and simulated runoff for 4-Tank-D Model using optimal parameters that calibrated through trial and error method.

Table 5: Optimum parameters calibrated for different configuration of Tank models

Parameters	3-Tank-D Model	4-Tank-D Model	5-Tank-D Model
C1	0.001	0.001	0.001
C2	0.002	0.002	0.002
C3	0.34	0.42	0.62
C4	0.0005	0.055	0.055
C5	0.6	0.6	0.6
C6	0.05	0.055	0.05
C7	-	0.83	0.83
C8	-	0.000001	0.00001
C9	-	-	0.00001
C10	-	-	0.00001
X1	10.00	10.00	10.00
X2	20.00	20.00	20.00

Table 6: Performance of different tank models validated with different data

Tank Configuration	Data Period	R	E^2
3-Tank-D Model	Jan to Mar 2000	0.714	0.7675
	Apr to Jun 2000	0.565	0.5803
	Jul to Sep 2000	0.511	0.3659
	Oct to Nov 2000	0.744	0.5510
Average		0.6335	0.5662
4-Tank-D Model	Jan to Mar 2000	0.758	0.8238
	Apr to Jun 2000	0.620	0.6920
	Jul to Sep 2000	0.574	0.3860
	Oct to Nov 2000	0.781	0.7461
Average		0.6833	0.6620
5-Tank-D Model	Jan to Mar 2000	0.714	0.7670
	Apr to Jun 2000	0.566	0.5794
	Jul to Sep 2000	0.512	0.2767
	Oct to Nov 2000	0.738	0.5845
Average		0.6325	0.5519

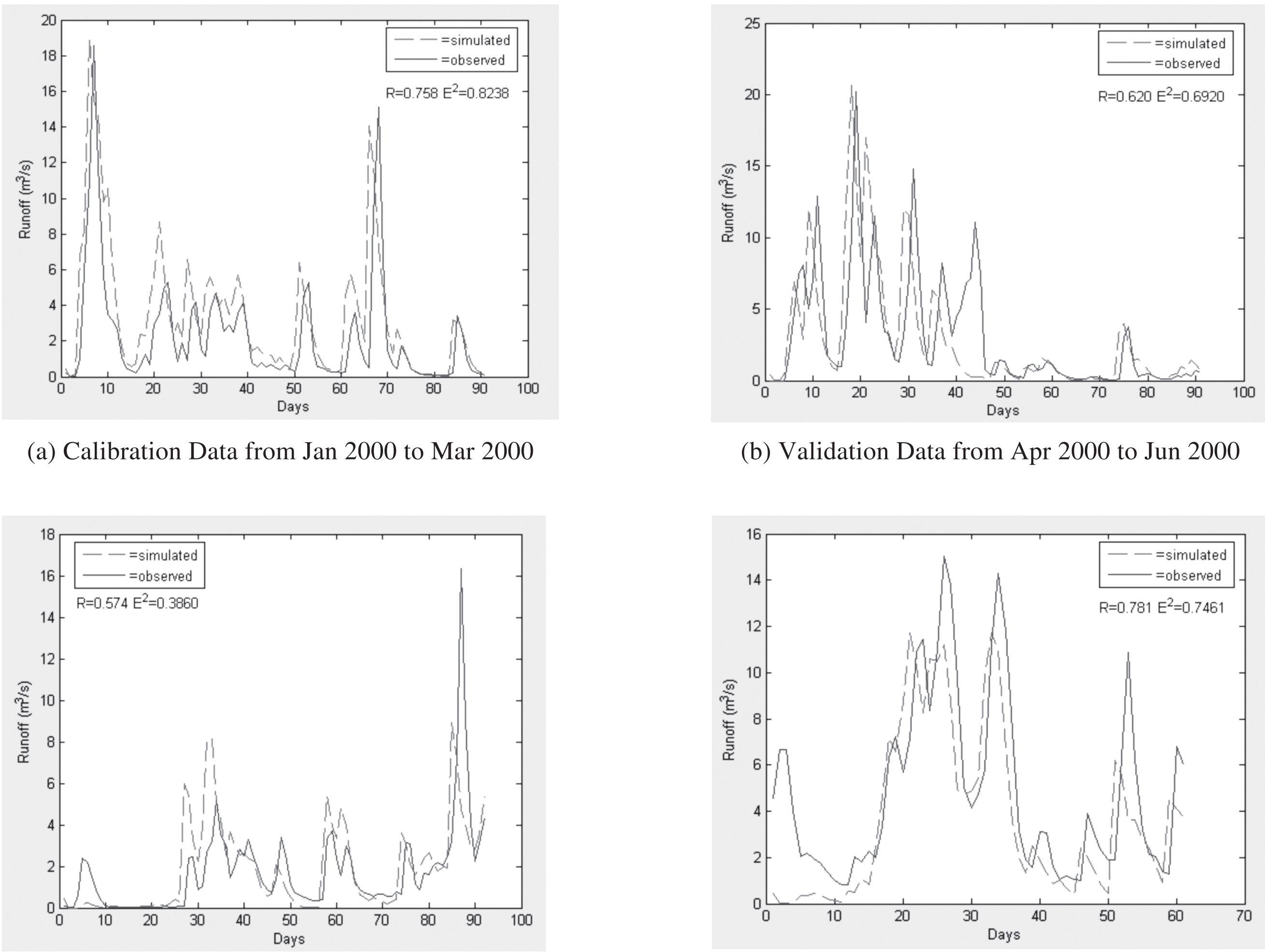

(a) Calibration Data from Jan 2000 to Mar 2000

(b) Validation Data from Apr 2000 to Jun 2000

(c) Validation Data from Jul 2000 to Sep 2000

(d) Validation Data from Oct 2000 to Nov 2000

Figure 5: Comparison between observed and simulated runoff for 4-Tank-D model using optimal parameters calibrated manually

The average R and E^2 obtained for 3-Tank-D model through manual calibration are recorded as 0.6335 and 0.5662 respectively, with configuration of X1=10, X2=20, C1=0.001, C2=0.002, C3=0.34, C4=0.0005, C5=0.6 and C6=0.05. The simulation result is improved significantly using 4-Tank-D model where average R and E^2 yield to 0.6833 and 0.6620 respectively with the configuration of X1=10, X2=20, C1=0.001, C2=0.002, C3=0.42, C4=0.055, C5=0.6, C6=0.055, C7=0.83 and C8=0.000001. As the Tank model is further investigated using 5-Tank-D, the performance of 5-Tank-D model is slightly decreased to average R=0.6325 and E2=0.5519. The optimal configuration for 5-Tank-D model were found to be X1=10, X2=20, C1=0.001, C2=0.002, C3=0.62, C4=0.055, C5=0.6, C6=0.05, C7=0.83, C8=0.000001, C9=0.000001 and C10=0.000001. It was found that the parameters C9 and C10 for 5-Tank-D Model are not improving the simulation results. Moreover, the optimum C9 and C10 values obtained through trial and error method are very small where both are depicted as low as 0.00001. Hence, it is concluded that the best number of tanks for simulating daily runoff in this study is 4 (4-Tank-D Model).

5.2 Sensitivity Analysis for Daily Runoff

Sensitivity analysis was conducted for 3-Tank-D, 4-Tank-D and 5-Tank-D models, to determine the effect and impact each of the parameters to model output in terms of R and E^2.

5.2.1 Sensitivity Analysis for 3-Tank-D Model

Figure 6 illustrates the results of sensitivity analysis of 3-Tank-D Model for R and E^2 values.

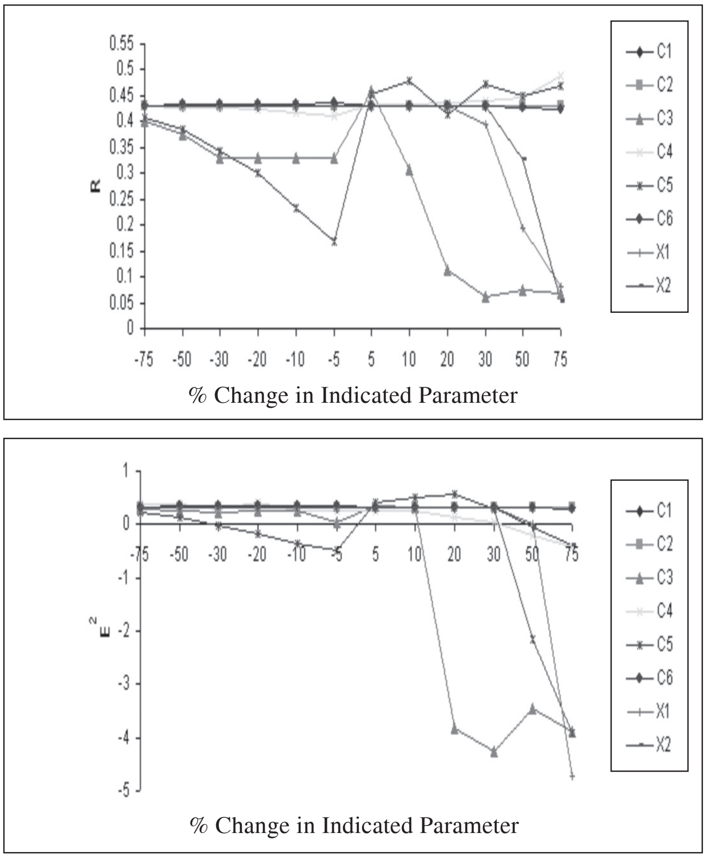

Figure 6: Sensitivity analysis of 3-Tank-D model for R values

From the results of sensitivity analysis, it appears that the change of C1 and C2 from 75% to –75% didn't affect the accuracy of the simulation results. Besides, the accuracy of the simulation results is slightly affected by parameters C4 and C6 as these two parameters changed from 75% to –75%. The infiltration parameters C3 and C5 have significant impact to the accuracy of the simulation results. Meanwhile, X1 and X2 were found not affecting the accuracy of simulation results as these two parameters changed from –75% to 30%. However, the simulation results were decreased significantly as X1 and X2 values increased to 50% and 75%.

5.2.2 Sensitivity Analysis for 4-Tank-D Model

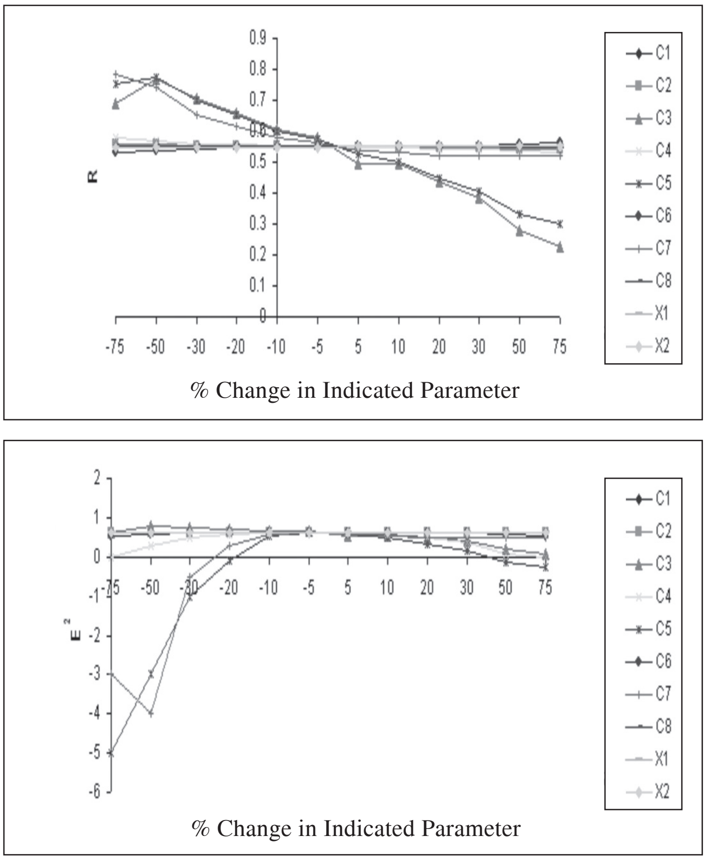

Figure 7: Sensitivity analysis of 4-Tank-D model for R and E^2 values

Sensitivity analysis for 4-Tank-D (illustrated in Figure 7) presents that parameters C1, C2, C6, C8, X1 and X2 didn't affect the simulation results significantly as these parameters changed from –75% to 75%. However, the infiltration parameters C3, C5 and C7 did show great impact to the accuracy of simulation results as these coefficients changed from –75% to 75%. Meanwhile, side outlet coefficient C4 has also affected the E^2 result with the changes of C4 from –75% to 75%.

5.2.3 Sensitivity Analysis for 5-Tank-D Model

The results of sensitivity analysis of 5-Tank-D Model for R and E2 values are illustrated in Figure 8. The results show that parameters C1, C9 and C10 are not sensitive to the change from 75% to –75%. Coefficient C2, C6, C8, X1 and X2 are slightly affecting the accuracy of the simulation results with the change from 75% to –75% of these parameters. Meanwhile, parameters C3, C4, C5 and C7 had significant impact to the simulation results as these parameters changed from 75% to –75%.

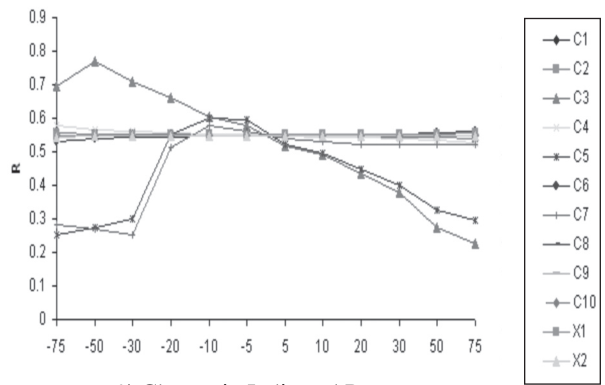

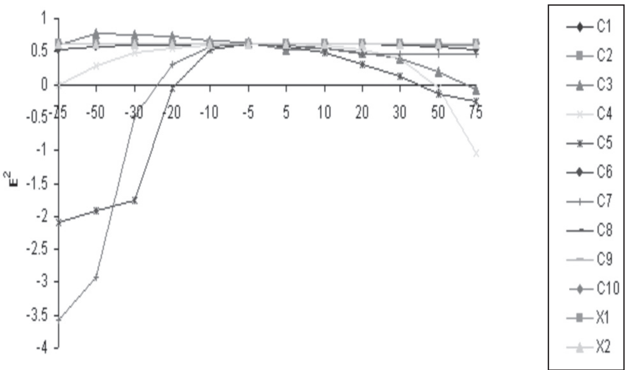

Figure 8: Sensitivity analysis of 5-Tank-D model for R and E^2 values

Since the result show that both C9 and C10 don't have any impact to simulation results, these two parameters which are the infiltration coefficient from forth to fifth tank and side outlet coefficient for fifth tank respectively, can be ignored. Therefore, it is concluded that the best number of tank for daily runoff simulation for Bedup Basin is four.

5.3 Determination Number of Tanks for Hourly Runoff

Three configurations of Tank model are investigated for hourly runoff simulation, named as 3-Tank-H, 4-Tank-H and 5-Tank-H. The optimum parameters obtained for 3-Tank-H, 4-Tank-H and 5-Tank-H models calibration are presented in Table 7. Table 8 shows the performance of 3-Tank-H, 4-Tank-H and 5-Tank-H when simulating 8 separate storm events using optimal parameters obtained. Figure 9 presents comparison between observed and simulated runoff for 4-Tank-H Model using optimum parameters obtained.

For hourly runoff simulation, all 3-Tank-H, 4-Tank-H and 5-Tank-H are able to simulate hourly runoff accurately. The optimal parameters obtained for 3-Tank-H model are C1 = 0.01, C2 = 0.002, C3 = 0.1, C4 = 0.01, C5 = 0.08, C6 = 0.05, X1 = 10 and X2 = 30, where average R and E^2 yield to 0.8916 and 0.7492 respectively. It was found that the performance of Tank model is slightly increased as the number of tank increased from 3 to 4.

Table 7: The optimum parameters calibrated for different configuration of tank models

Parameters	3-Tank-H Model	4-Tank-H Model	5-Tank-H Model
C1	0.010	0.010	0.001
C2	0.002	0.002	0.002
C3	0.100	0.100	0.070
C4	0.010	0.010	0.020
C5	0.080	0.080	0.040
C6	0.050	0.050	0.050
C7	-	0.030	0.030
C8	-	0.050	0.050
C9	-	-	0.030
C10	-	-	0.002
X1	10	10	10
X2	30	40	40

Table 8: The performance of different configuration of tank model

Tank Configuration	Data Period	R	E^2
3-Tank-H Model	1-7 Jan 99	0.945	0.8560
	5-8 Apr 99	0.891	0.3901
	5-8 Feb 99	0.864	0.7586
	8-12 Aug 98	0.743	0.7720
	9-12 Sep 98	0.984	0.8772
	15-18 Mar 99	0.978	0.9473
	20-24 Jan 99	0.836	0.8532
	26-31 Jan 99	0.892	0.5388
Average		0.8916	0.7492
4-Tank-H Model	1-7 Jan 99	0.946	0.8399
	5-8 Apr 99	0.916	0.5096
	5-8 Feb 99	0.857	0.8979
	8-12 Aug 98	0.776	0.8387
	9-12 Sep 98	0.971	0.9701
	15-18 Mar 99	0.977	0.9851
	20-24 Jan 99	0.853	0.8966
	26-31 Jan 99	0.892	0.6331
Average		0.8985	0.8214
5-Tank-H Model	1-7 Jan 99	0.947	0.8552
	5-8 Apr 99	0.891	0.3901
	5-8 Feb 99	0.864	0.7553
	8-12 Aug 98	0.743	0.7720
	9-12 Sep 98	0.986	0.8727
	15-18 Mar 99	0.979	0.9456
	20-24 Jan 99	0.836	0.8531
	26-31 Jan 99	0.892	0.5388
Average		0.8923	0.7479

The average R and E^2 were found improved to 0.8985 and 0.8214 respectively with the configuration of C1 = 0.01, C2 = 0.002, C3 = 0.1, C4 = 0.01, C5 = 0.08, C6 = 0.05, C7 = 0.03, C8 = 0.05, X1 = 10 and X2 = 40. Besides, the best configuration obtained for 5-Tank-H model are C1 = 0.001, C2 = 0.002, C3 = 0.07, C4 = 0.02, C5 = 0.04, C6 = 0.05, C7 = 0.03, C8 = 0.05, C9 = 0.03, C10 = 0.002, X1 = 10 and X2 = 40.

However, the performance of 5-Tank-H model is slightly decreased with average R=0.8923 and E^2=0.7479. This reflected that the optimum numbers of Tank model for hourly runoff calibration is 4 (4-Tank-H model) for Bedup Basin.

5.4 Sensitivity Analysis for Hourly Runoff

Sensitivity Analysis was conducted for 3-Tank-H, 4-Tank-H and 5-Tank-H models. The aim is to determine the effect and impact each of the parameters to runoff peak discharge.

5.4.1 Sensitivity Analysis for 3-Tank-H Model

The result of sensitivity analysis of 3-Tank-H Model for Runoff Peak Discharge was illustrated in Figure 10. From the results of sensitivity analysis, it appears that the change of C1 and C2 from 75% to –75% didn't affect the runoff peak discharge. Besides, it was also observed that the parameter C4, X1 and X2 also not affecting the runoff peak discharge much. However, the sensitivity analysis shows that the infiltration coefficient C3, C5 and side outlet coefficient C6 are the three dominant parameters that control the runoff peak discharge. The results show that these three parameters have significant impact to the runoff peak discharge as these three parameters change from 75% to –75%.

5.4.2 Sensitivity Analysis for 4-Tank-H Model

Figure 11 presents the results of sensitivity analysis of 4-Tank-H Model for runoff peak discharge. Sensitivity analysis for 4-Tank-H illustrates that parameters C1, C2, C7, X1 and X2 are not sensitive to the runoff peak discharge as these parameters change from –75% to 75%. Meanwhile, parameter C4 has minor effect to the runoff peak discharge. However, the results show that the four main parameters that controlled the runoff peak discharge are C3, C5, C6 and C8.

These four parameters did show great impact to the runoff peak discharge as the coefficients changed from –75% to 75%.

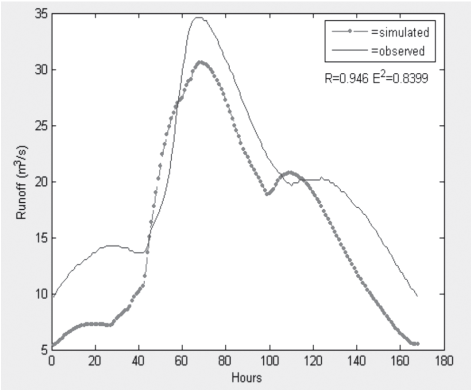

(a) Calibration data from 1 Jan 1999 to 7 Jan 1999

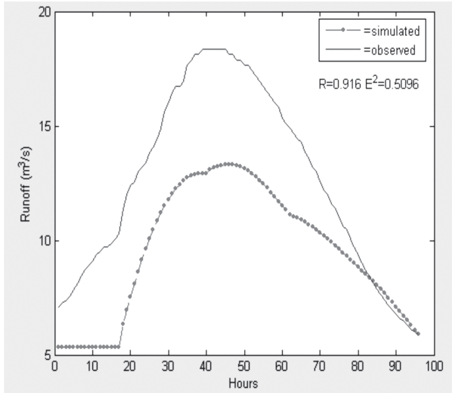

(b) Validation data from 5 Apr 1999 to 8 Apr 1999

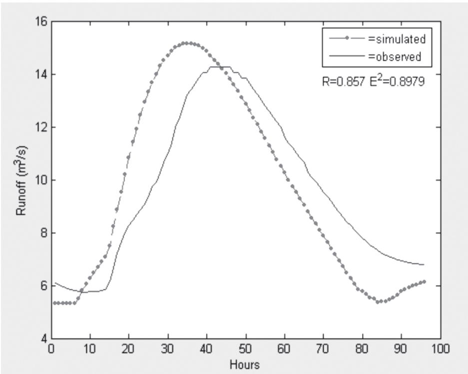

(c) Validation data from 5 Feb 1999 to 8 Feb 1999

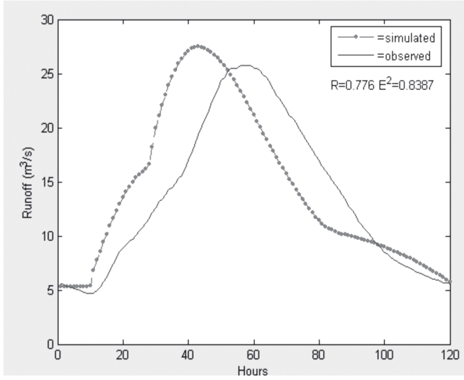

(d) Validation data from 8 Aug 1998 to 12 Aug 1998

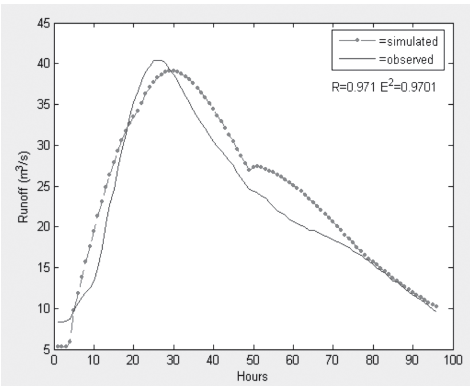

(e) Validation data from 9 Sep 1998 to 12 Sep 1998

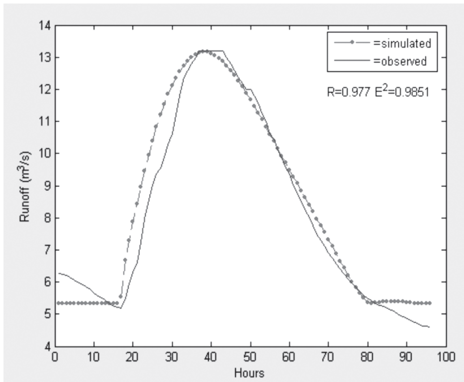

(f) Validation data from 15 Mar 1999 to 18 Mar 1999

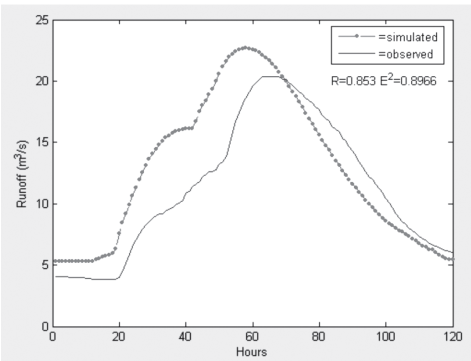

(g) Validation data from 20 Jan 1999 to 24 Jan 1999

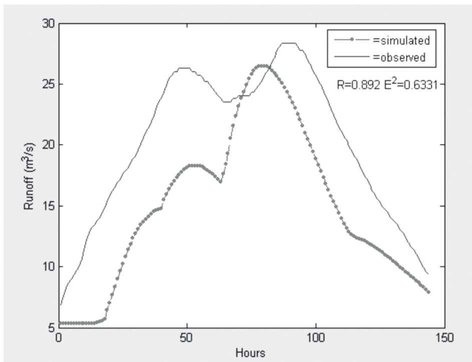

(h) Validation data from 26 Jan 1999 to 31 Jan 1999

Figure 9: Comparison between observed and simulated runoff for 4-Tank-H model using optimum parameters obtained

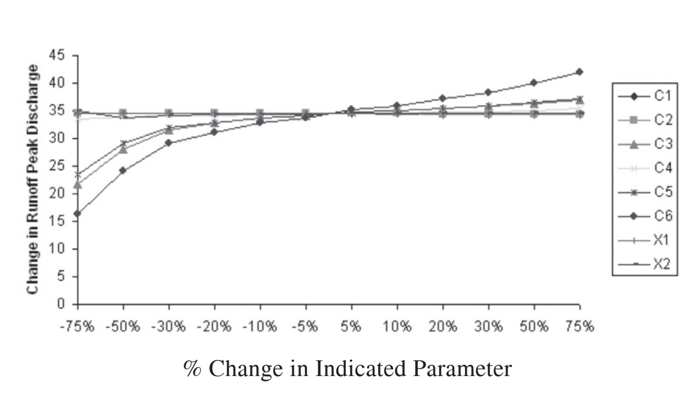

Figure 10: Sensitivity analysis of 3-Tank-H model for runoff peak discharge

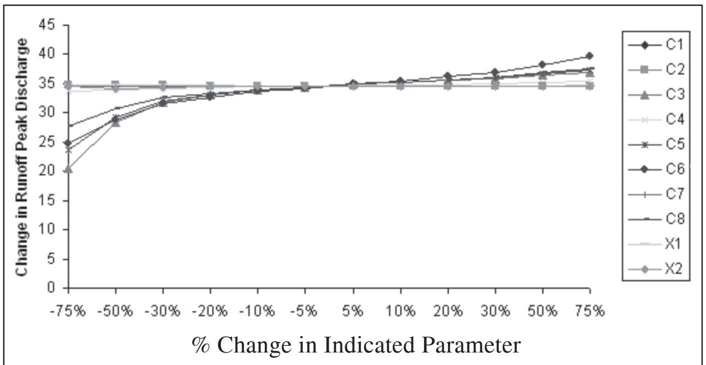

Figure 11: Sensitivity analysis of 4-Tank-H model for runoff peak discharge

5.4.3 Sensitivity Analysis for 5-Tank-H Model

The results of sensitivity analysis of 5-Tank-H Model for runoff peak discharge are illustrated in Figure 12. The results show that parameters C1, C2, C10, X1 and X2 do not affect the runoff peak discharge as these coefficients change from 75% to –75%. It was observed that coefficients C7 and C9 have minor impact to the runoff peak discharge as these values change from -75% to 75%. Results also show that five major coefficients that are controlling the runoff peak discharge are C3, C4, C5, C6 and C8.

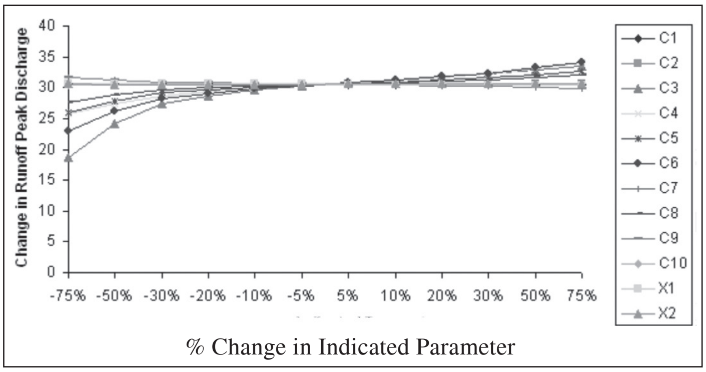

Figure 12: Sensitivity analysis of 5-Tank-H model for runoff peak discharge

As the result show that C9 has minor impact to runoff peak discharge and C10 doesn't have any impact to runoff peak discharge, these two parameters which are the infiltration coefficient from forth to fifth tank and side outlet coefficient for fifth tank respectively, can be ignored. Therefore, it is concluded that the optimum number of tank for hourly runoff simulation for Bedup Basin is four.

6.0 CONCLUSIONS

Results revealed that the best number of tank for rural catchment in humid region was found to be four for both daily and hourly runoff simulation. The average R and E^2 obtained are yielding to 0.6833 and 0.6620 respectively obtained from 4-Tank-D, with the configuration of X1 = 10, X2 = 20, C1 = 0.001, C2 = 0.002, C3 = 0.42, C4 = 0.055, C5 = 0.6, C6 = 0.055, C7 = 0.83 and C8 = 0.000001. For hourly runoff simulation, the best average R and E^2 obtained are 0.8985 and 0.8214 respectively through 4-Tank-H model, with the configuration of C1 = 0.01, C2 = 0.002, C3 = 0.1, C4 = 0.01, C5 = 0.08, C6 = 0.05, C7 = 0.03, C8 = 0.05, X1 = 10 and X2 = 40.

The sensitivity analysis for daily runoff simulation also indicated that both infiltration coefficient from forth to fifth tank (C9) and side outlet coefficient for fifth tank (C10), have very little impact to simulation results. Thus, these two parameters can be neglected and ignored. This clearly confirmed that the fifth tank is not necessary and the best number of tank for rural catchment in humid region is four. ■

REFERENCES

[1] Sugawara M and Funiyuki M. (1956). A Method of Revision of the River Discharge by Means of a Rainfall Model. Collection of Research Papers about Forecasting Hydrologic variables: 14-18.

[2] Sugawara, M. (1967). The Flood Forecasting by a Series Storage Type Model. Int. Symposium Floods and their Computation, International Association of Hydrologic Sciences, 1–6.

[3] Sugawara, M. (1979). Automatic Calibration of the Tank Model. Hydrological Sciences-Bulletin. 24. No.3.

[4] Sugawara, M. (1984). Tank Model with Snow Component. Research Note of the National Research Center for Disaster Prevention, No. 65, 1–293.

[5] Sugawara, M. (1995). Chapter 6: Tank model. Computer models of watershed hydrology, V. P. Singh, ed., Water Resources Publications, Littleton, Colo.

[6] Department of Drainage and Irrigation Sarawak, Malaysia: DID (2007). Hydrological Year Book Year 2007.

[7] Huang, M.C., Xie, J.C., Cai, Y., Wang, N. and Zhang, Y.J. (2006). Application of Middleware Technique in Web of Flood Forecasting System with Multiple Models. International Conference on Hybrid Information Technology (ICHIT'06), IEEE Computer Society.

[8] Sothea. K., Goto, A. and Mizutani, M. (2006). A hydrologic Analysis on Inundation in the Flooding Area of the Mekong Delta, Cambodia-The Combined Deterministic and Stochastic Models for Flood Forecasting. World Environmental and Water Resources Congress 2006, ASCE: 1-10

[9] Chen, J.Y., and Barry, J. A. (2006). Semidistributed Form of the Tank Model Coupled with Artificial Neural Networks. Journal of Hydrologic Engineering, Vol. 11, No. 5, September 1, 2006. ASCE: 408-417

[10] Sugawara, M. (1957). On the Analysis of Runoff Structure About Several Japanese Rivers. Research memoir of the Ins. of statistical math: 1-76.

[11] Sugawara, M., et al. (1974). Tank model and Its Application to Bird Creek, Wollombi Brook, Bikin River, Kitsu River, Sanga River and Nam Mune. Research Note, National Research Center for Disaster Prevention, No. 11, Kyoto, Japan, 1–64.

[12] Cooper, V.A., Nguyen, V-T-V. and J.A. Nicell (1997). Evaluation of Global Optimization Methods for Conceptual Rainfall-Runoff Model Calibration. Water Sci. Technol. 36(5):53-60.

[13] Cooper, V., Nguyen, V-T-V. and Nicell, J. (2007). Calibration of Conceptual Rainfall-Runoff Models using Global Optimization Methods with Hydrologic Process-based Parameter Constraints. Journal of Hydrologic, Vol. 334, No. 3-4, pp. 455-466.

[14] Yokoo, Y., Kazama, S., Sawamoto, M. and Nishimura, H. (2001). Regionalization of Lumped Water Balance Model Parameters Based on Multiple Regression. Journal of Hydrology. 246 (2001), 209-222.

[15] Setiawan, B.I., Fukuda, T., and Nakano. Y. (2003). Developing Procedures for Optimization of Tank Model's Parameters. CIGR Journal of Scientific Research and Development. June:1-13.

[16] Paik, K., Kim, J.H., and Lee, D.R. (2005). A Conceptual Rainfall-runoff Model Considering Seasonal Variation. Wiley InterScience 19:3837-3850.

[17] Chen, R.S., Pi, L.C., and Hsieh, C.C. (2005). A Study on Automatic Calibration of Parameters in Tank Model. Journal of the American Water Resources Association (JAWRA), April, 2005: 389-402.

[18] Kuok, K.K., Harun, S., and Shamsuddin, S.M. (2007). Optimization of Tank Model's Parameters Using Global Optimization Methods. Proceedings of 2nd International Conference on Managing Rivers in the 21st Century (Rivers'07), 6-8 June 2007, Kuching, Sarawak.

[19] Kuok, K.K., Harun, S., Shamsuddin, S.M., and Chiu, P.C. (2008). Tank Model's Parameters Optimization Using Particle Swarm Optimization Technique and Shuffle Complex Evolution Technique. Proceedings of Curtin University of Technology Science and Engineering International Conference (CUTSE'08), 24th - 27th November 2008, Miri, Sarawak.

[20] Kuok, K.K., Harun, S., Shamsuddin, S.M., and Chiu, P.C. (2009). Optimization of Tank Model's Parameters Using Particle Swarm Optimization approach. Proceedings of International Conference on Engineering and Education in the 21st Century (ICEE), 23rd - 25th Mac 2009, Kuching, Sarawak.

[21] Kuok, K.K., Harun, S., and Shamsuddin, S.M. (2010). Global Optimization Methods for Calibration and Optimization of the Hydrologic Tank Model's Parameters. Canadian Journal on Environmental, Construction and Civil Engineering, Vol. 1 No. 1, February 2010, pp. 1-14.

[22] *Jabatan Ukur dan Pemetaan Malaysia*: JUPEM (1975). Scale 1:50,000

[23] Hamby, D.M. (1994). A Review of Techniques for Parameter Sensitivity Analysis of Environmental Models. Journal of Environmental Monitoring. 32(2). 135-154

[24] Lenhart, T., Eckhardt, K., Fohrer, N., and Frede, H.G. (2002). Comparison of Two Different Approaches of Sensitivity Analysis. Journal of Physics and Chemistry of Earth, 27(9-10), 645-654.

PROFILES

IR. DR KUOK KING KUOK holds Bachelor of Civil Engineering with honours from UTM, Master of Engineering major in Hydrology from UNIMAS, PhD in Hydrology and Water Resources from UTM. He is also a Professional Engineer registered with BEM, EMF International Professional Engineer (MY), Asean Chartered Professional Engineer. He is also a corporate member of Institution of Engineers Malaysia, ASEAN Engineer and APEC Engineer. Currently he is lecturing at Swinburne University of Technology (Sarawak Campus).

ASSOCIATE PROFESSOR DR SOBRI HARUN holds Bachelor of Science major in Civil Engineering with Honours from Salford University, UK, Master of Science in Engneering Hydrology from Imperial College London and PhD in Hydrology and Water Resource from UTM. Currently he is the head of Department of Hydraulics and Hydrology, Faculty of Civil Engineering, Universiti Teknologi Malaysia.

MDM. CHIU PO CHAN currently is a lecturer in Faculty of Computer Science and Information Technology, UNIMAS. She holds Bachelor of Information Technology major in Software Engineering, Master of Science in Computer Science major in Human Computer Interaction.

PHYSICAL, GEOTECHNICAL AND MORPHOLOGICAL CHARACTERISTICS OF PEAT SOILS FROM SARAWAK

(Date received:25.5.2009/Date approved:10.8.2011)

Aminur M. R.[1], Kolay P. K.[2], Taib S. N. L.[3], Mohd Zain, M. I. S.[4] and Kamal, A. A.[5]

[1,3,4,5]Department of Civil Engineering, Universiti Malaysia Sarawak, 94300 Kota Samarahan, Sarawak

[2]Asst. Professor, Department of Civil and Environmental Engineering, Southern Illinois University Carbondale, 1230 Lincoln Drive, MC 6603, Carbondale 62901, Illinois, USA

E-mail: [1]aminur83@gmail.com, [2]pkolay@siu.edu, [3]tlinda@feng.unimas.my, [4]mzmisafawi@qad.unimas.my, [5]aakamal@feng.unimas.my

Ph. 01-618-453-7843; Fax: 01-618-453-3044

ABSTRACT

In Malaysia, Sarawak has the largest area of peat-land in the country, covering approximately 1.66 million hectares. With the rapid industrialisation and population growth, construction is scheduled almost all over the place including the area of peat-land. As peat or highly organic soil is a major problem in infrastructure development of the tropical and coastal regions, we should initially discern the physical and geotechnical properties of these soils. The current study describes the physical and geotechnical properties of tropical peat soils from Matang, Sarawak. Different physical properties e.g. organic content (OC), liquid limit (LL), fiber content (FC), and specific gravity (G_s) and geotechnical properties e.g. compaction, and Unconfined Compressive Strength (UCS) test have been conducted on remoulded peat soil samples. The results show that peat has very high moisture content and organic content; low specific gravity, dry unit weight and UCS value. Also, Scanning Electron Microscope (SEM) images were taken for some peat soil samples in order to study their microstructures.

Keywords: *Geotechnical Properties, Physical Properties, SEM, Tropical Peat Soil*

1.0 INTRODUCTION

The state of Sarawak is crossed by deep rivers and contains extensive freshwater wetlands and salty mangrove peat swamps or soils. These peat soils have been identified as one of the major groups of soil found here and it has the largest peat land area in Malaysia which is about 16,500 km^2, of which about 90% of the peat is more than 1 m in depth [1], which contributes difficulties in construction industries. High rain fall intensity of 120 inches per year makes peat soils become extremely soft and wet. Figure 1 shows the distribution of peat land in Sarawak [2].

Peat soil is a major problem in the infrastructure development of the coastal areas in Sarawak and generally considered as problematic soil in any construction project, because of its high compressibility and very low shear strength [3]. With the rapid industrialisation and population growth, it has become a necessary to have infrastructure facilities in peat-land as well. Before endorsing any types of construction on it, we should determine the physical and geotechnical properties of these soils.

Several researchers have studied on the soft or peat soil stabilisation and their physical properties [4-12]. Few researchers have discussed on the morphological investigation of clay and peat soils [13-17]. However, most of these studies concentrate on the stabilisation and very few studies are available on physical or geotechnical properties of original peat or soft soil from East Malaysia especially from Sarawak. Hence, the present study concentrates on determining the physical, geotechnical and morphological characteristics of peat soil samples from Matang, Sarawak, Malaysia, for better understanding of the behavior of these peat soils.

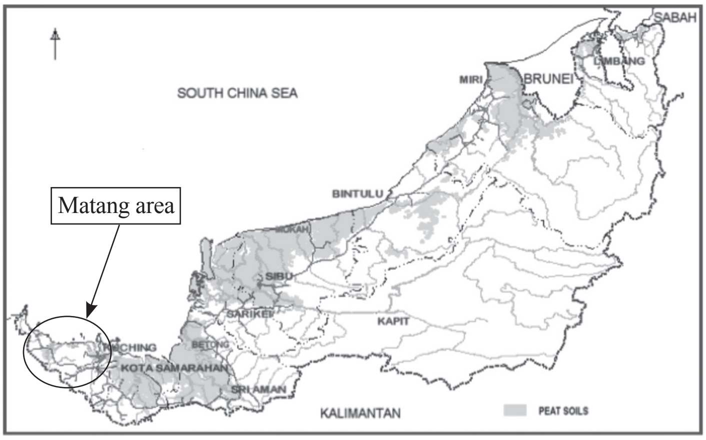

Figure 1: Peat soil distribution map in Sarawak, Malaysia [2]

2.0 TEST MATERIALS AND METHODOLOGY

Different types of peat soils were collected from six different locations (e.g., L_1 to L_6) in Matang area (from 0.40 to 0.80 m depth) designated as M_1 to M_6, respectively. The locations of sampling are shown in Table 1, as global coordinate. First the peat soil was sundried, grinded and passed through specific sieve and used for various physical and engineering properties test.

Table 1: Global coordinate or position of peat soil samples collected

Sample Location	Designation	Position
Taman Malihah-1	M_1	N 01˚ 33.986'; E 110˚ 15.464'
Taman Malihah-2	M_2	N 01˚ 33.997'; E 110˚ 15.415'
Kopodim-1	M_3	N 01˚ 34.782'; E 110˚ 16.396'
Kopodim-2	M_4	N 01˚ 34.914'; E 110˚ 16.400'
SMK Matang-1	M_5	N 01˚ 34.030'; E 110˚ 15.326'
SMK Matang-2	M_6	N 01˚ 35.730'; E 110˚ 16.440'

2.1 Physical Properties

The natural moisture content of peat soil samples has been determined as per BS 1377: Part 2: 1990 [18]. The Loss on Ignition has been determined as a percentage of oven-dried mass as per ASTM D 2974 [19]. The moist sample is first dried in the oven at a temperature of 105°C for 24 hours then the oven dried sample was kept in a muffle furnace at temperature of 550°C for 4 to 5 hours. The sample was then cooled at room temperature and the change in weight is calculated as Loss on Ignition. Organic content (H) is calculated according to an equation proposed by Skempton and Petley [20] as follows:

$$H\ \% = 100 - C\ (100 - N) \qquad (1)$$

Where, C is the correction factor (=1.04 for temperature 550°C; Edil [21]) and N is the loss on ignition in percent. The degree of decomposition is generally assessed by means of the Von Post scale. There are 10 degrees of humification (H_1 to H_{10}) in the Von Post system [22]. The specific gravity (G_s) of the highly organic or peat soil is determined based on procedure stated in BS 1377: Part 2: 1990 [18]. In this test, Gs is determined by using small pyknometer and the average Gs is obtained from the results of three tests. The fiber content (FC) is determined from dry weight of fibers retained on ASTM sieve no. 100 (>0.15 mm opening size) as a percentage of oven dried mass [23]. In this study, cone penetrometer method has been used to determine the liquid limit (LL) of peat soil sample. The LL and pH test have been conducted as per guidelines based on BS 1377: Part 2: 1990 [18].

2.2 Engineering Properties

Standard Proctor test has been conducted as per BS 1377-1990: Part 4 [18] to determine the maximum dry density (MDD) (γd) and the optimum moisture content (OMC) of the peat soil sample. To determine the undrained shear strength of the original remolded peat soil, the UCS test has been conducted according to the guidelines provided by ASTM D 2166 [24]. The size of the mould used in this study was 38 mm in diameter and 76 mm in height. A rate of strain of 1.27 mm/min has been maintained throughout the tests. For the sake of consistent results, a minimum of 3 samples have been tested. The prepared specimens were kept for 1 hour at room temperature in open space and then tested.

2.3 Microstructure Analysis

The SEM micrographs of only M_1, M_3 and M_6 peat soil samples (with the highest, medium and lowest fiber/organic content, respectively) have been conducted to study the morphology of the samples. SEM can produce high resolution three dimensional image of specimen surface. SEM consists of an electron gun (V-shaped tungsten filament) which emits electron beam thermionically when heated to a certain temperature and because of the application of high negative voltage this electron beam is directed towards anode (electron gun acts as cathode). The electron beam is refined by a system of electromagnetic lenses before it strikes the specimen. The specimen is inserted in a ‘specimen stage’ which is located in the direction of impinging electrons. These beaming electrons after striking the specimen surface produce secondary electrons which are then collected by a ‘secondary electron detector’ to generate a variety of signals. These signals are processed and converted into a series of pixels which can be viewed on a cathode ray tube or monitor (Bozzola and Russell [25]). The oven dried peat soil samples used in this tests which were coated with gold before taking SEM images. The SEM test was conducted by using the instrument JEOL, Japan, with model no. JSM-6701F. The micrographs were taken at a magnification of 1000 for all three samples.

3.0 RESULTS AND DISCUSSION

3.1 Physical Properties

The results of different physical properties of the peat soil samples are presented in Table 2. From Table 2, it is found that the moisture content of the peat soil is very high, this may attributed to the fact that, peat soils have high fiber content which is able to absorbed water. Huat [3] stated that the natural water content of West Malaysian peat varies from 200 to 700% and East Malaysian peat varies from 200 to 2207%. Our value also falls within the ranges. From the laboratory test, it has been observed that the sample M_1 to M_5 falls in the category with degree of humification H_4 to H_6 (Hemic) and sample M_6 can be categorized as H_7 to H_{10} (Sarpic); according to the Von Post scale. If the percentage of organic content (OC) in soil is more than 75% then the soil can be categorised as peat soil as per ASTM D 2607 69 [26]. In this study sample M_4 and Sample M_6 contain less than 75% OC and can be categorised as highly organic soil. The remaining soil samples can be categorised as peat. The result shows that M_1 soil sample has higher fiber content (FC) than others soil samples and the sample M_6 has lowest fiber content (FC).

Den Haan [27] studied that, the specific gravity in organic or peat soils is affected by the organic constituents; e.g., cellulose and lignin which are having lower specific gravity, approximately 1.58 and 1.40, which causes the reduction in specific gravity of peat soils. Huat [3] also reported that for tropical peat soil, G_s ranges from 1.07 to 1.7. In the present study, specific gravity (G_s) for the peat soil samples tested also falls within the ranges except for sample M6. The Gs value for sample M6 is higher as compared to the other samples tested. This may be attributed to the fact that sample M_6 is highly decomposed and has lowest fiber content (FC).

The LL value is higher for M_1 sample because M_1 sample contains more fiber which results in high water absorption capacity compared to the other samples. It is also found that all samples collected from Matang are non-plastic. The result also shows that sample M_2 has lower pH value than other peat soil samples and sample M_6 has the highest value. As a result, M_2 sample is more acidic due to the higher organic content.

Table 2: Physical properties for different peat soil samples

Property	Sample					
	M_1	M_2	M_3	M_4	M_5	M_6
Natural moisture content, (%)	620.14	473.70	360.72	787.04	623.76	605.63
Degree of decomposition	H_3	H_5	H_6	H_4	H_4	H_7
Loss on Ignition, (N) (%)	85.67	79.70	67.88	83.08	81.59	44.74
Organic content, (H) (%)	85.10	78.88	66.60	82.40	80.85	42.53
Specific gravity, (Gs)	1.45	1.62	1.64	1.48	1.56	1.82
Fiber content (FC) (%)	65.00	63.45	61.40	64.25	63.55	31.98
Liquid Limit (LL) (%)	78.00	79.00	73.00	75.00	77.00	69.00
pH value	4.05	4.64	5.15	4.25	4.33	6.18

3.2 Engineering Properties

3.2.1 Standard Proctor Test

Standard Proctor test were carried out for peat soil samples and the results are presented in Figure 2 and Table 3. From Figure 2, it can be noticed that for the soil sample M_6 has MDD of 0.88 gm/cm³ and the value of OMC is 54.95%. It can also be observed that this soil sample has the maximum dry density and minimum moisture content as compared to the other samples tested in this study. This may be attributed to the fact that sample M_6 has lower fiber content (FC) and as a result, it has lower water absorption capacity compared to the remaining peat soil samples.

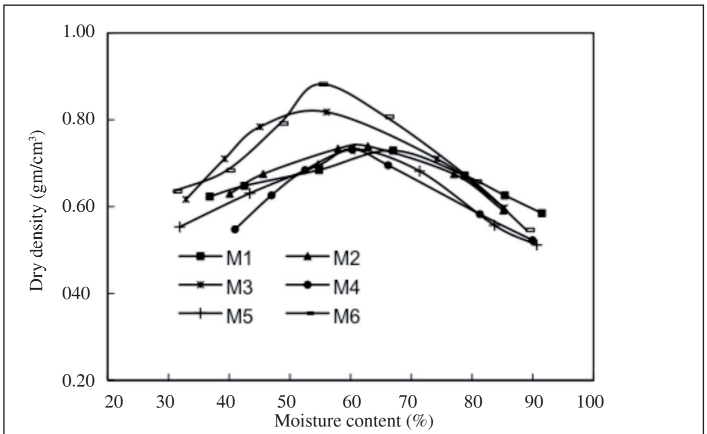

Figure 2: Standard Proctor test for different peat soil samples

The maximum dry density of the peat sample tested in this study varies from 0.72 to 0.88 gm/cm³. Our result falls within the range as reported by Huat [3]. The bulk densities of peat are in the range of 0.8 to 1.2 gm/cm³ whereas the dry densities are 0.1 to 1.4 gm/cm³.

3.2.2 Unconfined Compressive Strength Test

The UCS tests have been conducted for all soil samples compacted at its MDD and OMC of the soil and the results are presented in Table 3. In this study UCS value for original remoulded peat soil sample varies from 14.23 to 21.62 kPa. Behzad and Huat [28] also mentioned in their study that the UCS value for remoulded peat is 22 kPa.

It can be noticed that considerably higher compressive strength has been obtained from M_6 samples, it may be attributed to the fact that the sample M_6 has lower fiber content (FC) (i.e., 31.98%) which results lower water holding capacity and higher compressive strength. Also M_1 sample has lower UCS strength value it may be to the fact that, the M_1 sample has higher fiber content (FC) and organic content (OC).

Table 3: Geotechnical properties for different peat soil samples

Property	Sample					
	M_1	M_2	M_3	M_4	M_5	M_6
Optimum moisture content (OMC) (%)	65.36	62.84	56.10	60.25	60.64	54.95
Maximum dry density (MDD) gm/ cm^{-3}	0.72	0.74	0.83	0.73	0.73	0.88
Unconfined compressive strength (UCS) (kPa)	14.23	17.25	19.15	18.00	14.85	21.62

3.3 Scanning Electron Microscope (sem)

Scanning electron micrographs of peat soil samples M_1, M_3 and M_6 are shown in Figures 3, 4 and 5, respectively. Figure 3 shows that M_1 soils are composed of fibers, woody and porous in nature compared with M_3 and M_6 samples. Figure 4 shows that M_3 sample is more compact than M_1 sample. From Figure 5 (sample M_6), it can be observed that the particles are plate/sheet-like clay type structure. It may be attributed to the fact that, the more fibrous/organic content a soil is/has, the more porous space it has.

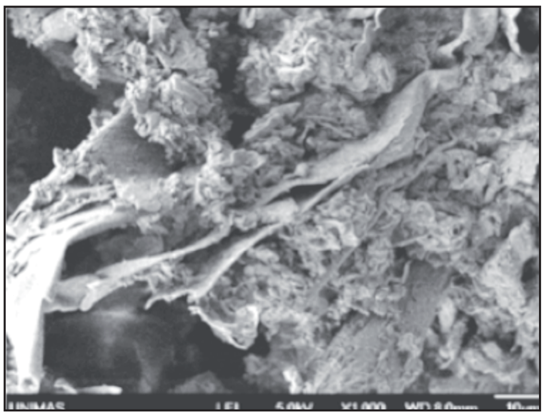

Figure 3: SEM micrograph of the peat soil sample M_1

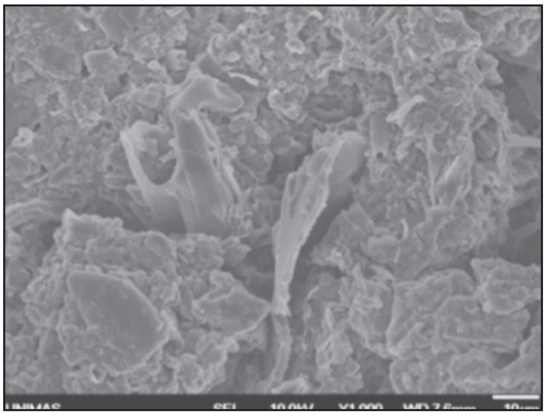

Figure 4: SEM micrograph of the peat soil sample M_3

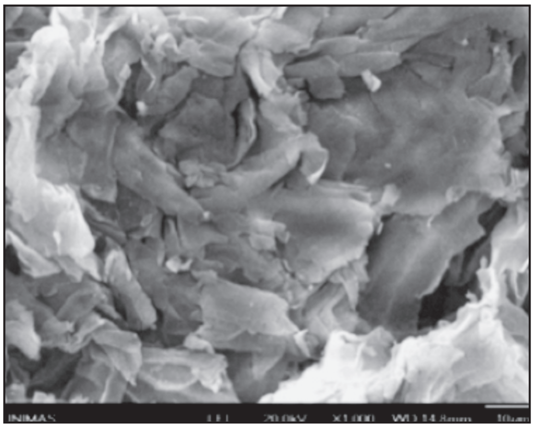

Figure 5: SEM micrograph of the peat soil sample M_6

4.0 CONCLUSIONS

The present paper investigates the physical, geotechnical and morphological properties of different types of peat soil samples from Matang, Sarawak, Malaysia. From the laboratory tests results, the following conclusions can be drawn:

i. The ranges of the natural moisture content, G_s, and pH for peat soil samples are between 360 to 787%, 1.45 to 1.82 and 4.05 to 6.18, respectively.
ii. The result shows that, FC, OC and *N* are within the ranges, 31 to 65%, 42 to 85% and 44 to 85%, respectively and according to the Von Post scale the sample M_1 to M_5 is Hemic and the sample M_6 is falls in the category of Sarpic.
iii. The standard Proctor test result shows that MDD and OMC ranges approximately between 0.72 to 0.88 gm/cm^{-3} and 55 to 65%, respectively.
iv. The result of UCS test shows that, the strength for different peat soil samples is between 14.23 to 21.62 kPa.
v. SEM result shows that the peat soil sample M_1 contains more fibers, woody and porous as compared with the samples M_3 and M_6. From sample M_6, it can be observed that the particles/fibers are so packed, plate or sheet-like and strongly bonded.

From the available data and to be established data bank on the region's peat soil compiled by the Construction on Soft Soil (CoSS) Group of UNIMAS, it is hope that the local geotechnical engineers can easily understand the behavior of physical and geotechnical properties as well as morphological characteristics of Sarawakian peat soils.

5.0 ACKNOWLEDGEMENTS

The author would like to acknowledge the MOSTI for financial support (Grant no. 03-01-09-SF0032). Also the authors would like to express deep gratitude for the technical supports offered by the Geotechnical laboratory staff and the Construction on Soft Soil Group members, Universiti Malaysia Sarawak, Malaysia. ■

REFERENCES

[1] A. A. Mutalib, J. S. Lim, M. H. Wong, and L. Koonvai, "Characterization, Distribution and Utilisation of Peat in Malaysia, Tropical Peat." Proceeding of the International symposium on Tropical Peatland, Kuching, Sarawak, Malaysia, pp. 7-16, 1991.

[2] H. S. Lee, "Utilisation and Conservation of Peatswamp Forests in Sarawak, Tropical Peat" Proceedings of the International symposium on Tropical Peatland, Kuching, Sarawak, Malaysia, pp. 286-292, 1991.

[3] B. B. K. Huat, "Organic and Peat Soils Engineering." University Putra Malaysia press. 1st Edition, pp. 5-11, 2004.

[4] E. K. Huttunen, and V. H. Kujala, "Assessment of the Quality of Stabilized Peat and Clay." Symposium Grouting and Deep Mixing, Balkema, pp. 607-612, 1996.

[5] D. T. Eriktius, E. C. Leong, and H. Rahardjo, "Shear Strength of Peaty Soil-Cement Mixes." Proceedings of the third International Conference on Soft Soil Engineering, Hong Kong, pp. 551-556, 2001.

[6] R. Andersson, S. E. Johansson, and K. G. Axelsson, "Stabilization of Organic Soils by Cement and Puzzolanic Reactions." A Feasibility Study within the Project Swedish deep stabilization, Report 3, 2002.

[7] S. Hebib, and R. E. Farrell, "Some Experiences on the Stabilization of Irish Peats." Can. Geotechnical Journal, Vol. 40, pp. 107-120, 2003.

[8] B. B. K. Huat, M. S. Shukri, and T. A. Mohamed, "Effect of Chemical Admixtures on the Engineering Properties of Tropical Peat Soils." American Journal of Applied Sciences, Vol. 2, No. 7, pp. 1113-1120, 2005.

[9] P. K. Kolay, and N.S.B. Romali, "Highly Organic Soil Stabilization by Different Types of Admixtures." 2nd International Conference on Problematic Soils, Sunway Resort Hotel, Petaling Jaya, Selangor, Malaysia, pp. 211-216, 2006.

[10] H. Roslan, and M. S. Shahidul, "A Model Study to Determine Engineering Properties of Peat Soil and Effect of Strength after Stabilization." European Journal of Scientific Research, Vol. 22, No, 2, pp. 205-215, 2008.

[11] D. Sadek, H. Roslan, and A. Abubakar, "Engineering Properties of Stabilised Tropical Peat Soils." EJGE paper 13, Bund. E, 2008.

[12] L. S. Wong, H. Roslan, and H. A. Faisal, "Engineering Behaviour of Stabilized Peat Soil." European Journal of Scientific Research, Vol. 21, No. 4, pp. 581-591, 2008.

[13] G. Rajasekaran, K. Kurali, and R. Srinivasaraghavan, "Effect on Chlorides and Sulphates on Lime Treated Marine Clays." Soils and Foundations, Vol. 37, No. 2, pp. 105-115, 1997.

[14] S. Nontananandh, and M. Kamon, "Hydration Mechanisms of Fly Ash Stabilized by Lime." Proc. of the 2nd International Conference on Environmental Geotechniques, Osaka, Japan, pp. 857-862, 1996.

[15] M. Kawamura, and S. Diamond, "Stabilisation of Clay Soils against Erosion Loss." Clay and Clay minerals, Vol. 23, pp. 443-451, 1975.

[16] M. Kamon, and S. Nontananandh, "Combining Industrial Wastes with Lime for Soil Stabilisation." Journal of Geotechnical Engineering, Vol. 117, No. 1, pp. 1-17, 1991.

[17] N.B. Hobbs, "Morphology and the Properties and Behaviour of Some British and Foreign Peats." Quarterly J. of Engineering Geology, Vol. 19, pp. 7-80, 1986.

[18] BS 1377, Part 1-4, "Soils for Civil Engineering Purposes." British Standards Institution. London. UK, 1990.

[19] ASTM D 2974, "Standard Test Method for Moisture, Ash, and Organic Matter of Peat and other Organic Soils." Book of ASTM Standards, ASTM, Philadelphia, USA, 2000.

[20] A.W. Skempton, and D. J. Petley, "Ignition Loss and Other Properties of Peats and Clays from Avonmouth, King's Lynn and Cranberry Moss." Geotechniques, Vol. 20, No. 4, pp. 343-356, 1970.

[21] T. B. Edil, "Recent Advancements in Geotechnical Characterization and Construction over Peat and Organic Soil." In Proceedings of 2nd International Conference on Advances in soft soil Engineering and Technology, Ed. Huat, et al., Putrajaya, Malaysia, pp. 3-35, 2003.

[22] L. Von Post, "Sveriges Geologiska Undersøknings torvinventering och nogra av dess hittils vunna resultat (SGU peat inventory and some preliminary results)." Svenska Mosskulturføreningens Tidsskrift, Jønkøping, Sweden Vol. 36, 1922.

[23] ASTM D1997-91, "Standard Test Method for Laboratory Determination of the Fiber Content of Peat Samples by Dry Mass." Annual Book of ASTM Standards, ASTM, Philadelphia, USA, 1996.

[24] ASTM D 2166, "Standard Test Method for Unconfined Compressive Strength of Cohesive Soil." Annual Book of ASTM Standards, ASTM, Philadelphia, USA, 2000.

[25] J. J. Bozzola, and L. D. Russell, "Electron microscopy: principles and techniques for biologists." Second edition, Jones and Bartlett Publishers, Sudbury, Massachusetts, 1999.

[26] ASTM D 2607-69. "Classification of Peats, Mosses, Humus, and Related Products." Annual Book of ASTM Standards, ASTM, Philadelphia, USA, 1990.

[27] E. J. Den Haan, "An Overview of the Mechanical Behaviour of Peat and Organic Soils and Some Appropriate Construction Techniques." In Proceedings on recent Advances in Soft Soil Engineering, Kuching Sarawak, pp. 17-45, 1997.

[28] K. Behzad, and B. K. Huat, "Improving Unconfined Compressive Strength of Peat with Cement, Polypropylene Fibers, and Air Curing Technique." Global Journal of Research in Engineering, Vol. 10, Issue 1, pp. 9-15, 2010.

PROFILES

MR. MD. AMINUR RAHMAN obtained his Bachelor Degree in Civil Engineering from Khulna University of Engineering and Technology, Bangladesh in 2006; Master Degree in Geotechnical Engineering from Universiti Malaysia Sarawak, Malaysia in 2010. Currently continues PhD study in Geotechnical Engineering at Swinburne University of Technology, Melbourne, Australia. His research interests are in ground improvement, characterisation of soft soil, solid waste and recycle materials in civil engineering application and finite element modeling in geotechnical engineering.

ENGR. DR SITI NOOR LINDA TAIB is a Senior Lecturer in the Department of Civil Engineering, Faculty of Engineering, Universiti Malaysia Sarawak, Malaysia. She is a graduate member of Board of Engineers, Malaysia and The Institution of Engineers, Malaysia. Her research works include slope stability analysis, soil nailing, development of image analysis in analysing soil movement and peat soil research. She is currently supervising several undergraduate and postgraduate research topics covering topics particularly on soft soil improvement.

DR PRABIR K. KOLAY is an Assistant Professor in Civil and Environmental Engineering Department at Southern Illinois University Carbondale, USA. He did his PhD in Geotechnical Engineering from IIT Bombay, India. His research interest is Geotechnical and Geo-environment Engineering and a member of IGS, TRB and IACMAG.

ASSOC. PROF. DR MOHAMMAD IBRAHIM SAFAWI is a Faculty member of the Engineering Faculty, Universiti Malaysia Sarawak in the Department of Civil Engineering specialises in the area of high performance concrete particularly lightweight foam and self-compacting concrete. His research interest is in the application of foam concrete in peat soils and design of peat soil replacement with another suitable material.

EN. AHMAD KAMAL ABD. AZIZ is currently a lecturer with Universiti Malaysia Sarawak under the Department of Civil Engineering and specialised in the area of Geotechnical Engineering especially in the area of finite element modeling. He graduated with BSc (Hons) from UiTM, Shah Alam and MSc in Science (Geotechnical Engineering) from Manchester University, UK.

A MULTILEVEL MULTIPLEXING TECHNIQUE FOR HIGH SPEED FIBER OPTIC COMMUNICATION SYSTEMS

(Date received:24.3.09/Date approved: 23.8.2011)

Amin Malekmohammadi[1] and Ahmad Fauzi Abas[2]
[1]*Department of Electrical and Electronic Engineering, Faculty of Engineering, The University of Nottingham, (Malaysia Campus), Jalan Broga, 43500 Semenyih, Selangor*
[2]*Department of Computer and Communication Systems Engineering, Universiti Putra Malaysia, 43400 Serdang, Selangor*
E-mail: [1]amin.maleknottingham.edu.my, [2]fauzi@eng.upm.edu.my

ABSTRACT

In order to explore the potential of optical multilevel signaling for high speed optical fiber networks, a novel multilevel multiplexing technique is demonstrated. Three users, each with data rates of 10 Gb/s were successfully multiplexed and transmitted over a single WDM channel, which can offer a possible transmission rate of 30 Gb/s per WDM channel. The performance of the proposed technique is examined, with comparison to 30 Gb/s Time Division Multiplexing (TDM). Based on the simulation results back-to-back receiver sensitivity of -29.2 dBm and -33.5 with OSNR of 22.5 dB and 18.3dB was achieved for the worst and best uses respectively, together with the chromatic dispersion tolerance ranging from 207 ps/nm to 276 ps/nm. A comparison with conventional TDM technique shows a clear advantage of the proposed technique.

Keywords: *Dispersion Tolerance, Multiploxing, Optical Communication*

1.0 INTRODUCTION

The advances in data communication and information technology allow tremendous amounts of data to be transferred through the networks. From one year to another, the required network capacity increases exponentially, which shows that Tb/s capacity is not far from reality.

Many kind of multiplexing such as Wavelength Division Multiplexing (WDM) technology, Time Division Multiplexing has recently shown their potential to support high bandwidth data transfer [1; 2; 3]. Time Division Multiplexing is a digital process that can be applied when the transmission capacity of a medium is larger than the transmitting and receiving devices data rate. In such case, multiple transmissions can occupy a single link by subdividing it into several slots.

Optical multilevel signaling is one of the candidates for these advanced signaling techniques used for future high speed long-distance optical networks [4]. It can reduce the optical signal bandwidth to pack more signal channels in a single optical fiber by WDM technique, and improve the signal transmission performance such as chromatic dispersion tolerance. For example, four-level phase modulation, namely, differential quadrature phase-shift keying (DQPSK) [5] was thoroughly studied to realise ultrahigh capacity WDM networks. Obviously, there are other methods employed to provide more transmission capacity such as quadrature signaling and spectrum coding [6] so that more than one channel can be transmitted in a single wavelength. However these methods are not economical and are difficult to realise.

The proposed technique which is called Absolute Polar Duty Cycle Division Multiplexing (AP-DCDM) is a new multiplexing technique which uses return to zero duty cycle and bipolar signaling. In this technique, subsequent users at the multiplexer input have opposite polarity, which results in a unique multilevel pattern at the output of the multiplexer. As a result of bipolar signaling, the increment of the multiplexed signal amplitude with reference to the number of user is reduced, therefore, improving the receiver sensitivity, which is the main limiting issue in multilevel signaling. In this paper, we demonstrate that AP-DCDM is able to support multi-users transmission per WDM channel at acceptable performance.

2.0 WORKING PRINCIPLE

AP-DCDM is a multiplexing technique that uses bipolar signal with different duty cycle to differentiate the channels or users. In this technique, each user transmits bit '0' with zero volts and for the case of bit one, the odd users transmit '$+A$' volts while the even users transmit '$-A$' volts. Based on the linear distribution of duty cycle, the i^{th} multiplexing user transmits bit 1 within T_i second, which is

$$T_i = i \times \left(\frac{T_s}{n+1} \right) \qquad (1)$$

Where T_s is the symbol duration and n is the number of users. Therefore, different users share the communication medium to transmit in the same time period and at the same carrier wavelength, but with different duty cycles. The unique duty cycle for each channel helps to regenerate data at the receiver. Figure 1 illustrates the signal multiplexing process for three users system. In Figure 1(a), 8 possible combinations of users' data are shown which is referred to as Case 1 to Case 8. Figures 1(b), (c) and (d) show the duty cycle distribution of the three user system, where 25%, 50% and 75% duty cycle are used to represent User1 (U25), User2 (U50) and User3 (U75) respectively. Noting that the second user has opposite polarity to the first user, and similarly, the third user has opposite polarity relative to the second user. Based on the 2^n possible bits combination in Figure 1(a), each of these combinations produces unique symbols with both positive and negative polarity [Figure 1(e)]. The process ends by taking the absolute value of the signal in Figure 1(e) to produce absolute polar DCDM signal. Figure 1(f) shows the absolute polar signal for the eight possible combinations of bits for three users. Having the knowledge about this uniqueness at the receiver side, the original data for each user can be recovered.

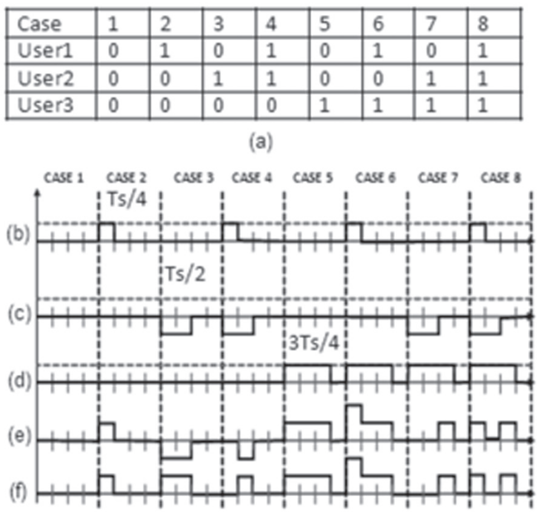

Case	1	2	3	4	5	6	7	8
User1	0	1	0	1	0	1	0	1
User2	0	0	1	1	0	0	1	1
User3	0	0	0	0	1	1	1	1

Figure 1: (a) eight possible combination of bits for three users, (b) U25 data stream, (c) U50 data stream, (d) U75 data stream, (e) bipolar multiplexed signal and (f) absolute polar multiplexed signal

3.0 SIMULATION SETUP

Figure 2 (a) shows the simulation setup. Three users each at 10 Gb/s with PRBS 2^{10}-1 are carved with three electrical RZ pulse carver at 25%, 50% and 75% duty cycle respectively. The voltages for all users at the multiplexer input are identical. All users' data are multiplexed via a power combiner (electrical adder) resulting in a bipolar signal. Subsequently, the absolute circuit is used to produce an absolute polar signal.

The signals are modulated onto a laser diode (LD) signal which operates at 1550 nm wavelength using a Mach-Zehnder Modulator (MZM). The eye diagram of the modulator output is shown in Figure 2(b). At the receiver side, the optical signal is detected by a photodiode and passed through a low-pass filter (LPF) and Clock-and-Data-Recovery (CDR) unit. The Gaussian low-pass filter is set at 0.75 of the null-to-null bandwidth, which is determined by the smallest duty cycle, to eliminating the photodiode noises.

In the CDR unit, the received signal is fed into the sampling circuit. The samples are taken at three sampling points of S_1, S_2 and S_3 at the first three slots in every symbol [Figure 2(b)]. Outputs of the sampling circuit are fed into the decision and regeneration unit. In this unit, the sampled values are compared against two threshold values, thr_1 and thr_2 [Figure 2(b)] and the decision is performed based on the operations shown in Tables I, II and III. These tables contain the regeneration rules that the data recovery unit uses to regenerate original data for each user, which are based on the multiplexed signals shown in Figure 1(f). For example, for U25, binary 0 is regenerated when sampling values at S_1 and S_2 are less than thr_1 (Table I rule 1) or values at S_1 is in between thr_1 and thr_2 while values in S_2 are greater than thr_1 (Table 1 rule 2). Binary 1 is regenerated when sampled amplitude at S_1 is in between thr_1 and thr_2, while amplitude at S_2 is less than thr1 (Table I rule 3) or values in S_1 is less than thr1 and values in S_2 are greater than thr_1 (Table 1 rule 4) or values in S_1 and S_2 are greater than thr_1 and thr_2 respectively (Table 1 rule 5).

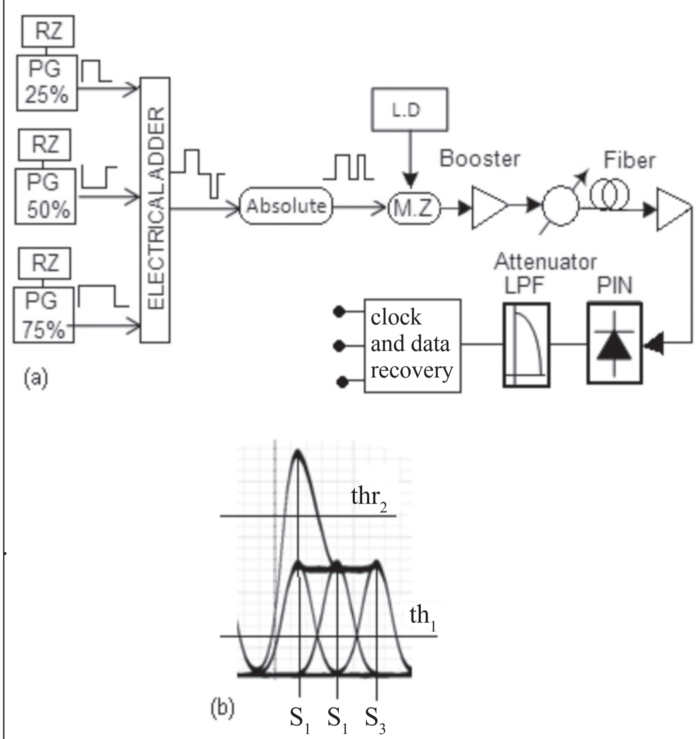

Figure 2: (a) AP-DCDM simulation setup for multiplexing three users, (b) Transmitted eye diagram including sampling points and threshold values

Table 1: Data recovery rules for U25

No	Rules	Case
1	if $(S_1 < thr_1)$ and $(S_2 < thr_1)$ then U25 = 0	Case: 1, 7
2	if $(thr_1 \leq S_1 < thr_2)$ and $(S_2 \geq thr_1)$ then U25 = 0	Case: 3, 5
3	if $(thr_1 \leq S_1 < thr_2)$ and $(S_2 < thr_1)$ then U25 = 1	Case: 2, 8
4	if $(S_1 < thr_1)$ and $(S_2 \geq thr_1)$ then U25 = 1	Case: 4
5	if $(S_1 \geq thr_2)$ and $(S_2 \geq thr_1)$ then U25 = 1	Case: 6

Table 2: Data recovery rules for U50

No	Rules	Case
1	if $(S_2 \geq thr_1)$ and $(S_3 < thr_1)$ then U50 = 1	Case: 3,4
2	if $(S_2 < thr_1)$ and $(S_3 \geq thr_1)$ then U50 = 1	Case: 7,8
3	if $(S_2 < thr_1)$ and $(S_3 < thr_1)$ then U50 = 0	Case: 1,2
4	if $(S_2 \geq thr_1)$ and $(S_3 \geq thr_1)$ then U50 = 0	Case: 5,6

Table 3: Data recovery rules for U75

No	Rules	Case
1	if $(S_3 < thr_1)$ then U75 = 0	Case: 1, 2, 3, 4
2	if $(S_3 \geq thr_1)$ then U75 = 1	Case: 5, 6, 7, 8

4.0 RESULTS AND DISCUSSION

Figure 3 shows the back-to-back pre-amplified receiver sensitivity for the three users, 30 Gb/s (3 x 10 Gb/s) AP-DCDM system. They are compared against conventional 30 Gb/s TDM. In AP-DCDM system, the three users show different performance. At bit-error-rate (BER) of 10^{-9}, U25 has the receiver sensitivity of around -29.2 dBm with OSNR of 22.5 dB, while U50 and U75 have the same receiver sensitivity of -33.5 dBm with OSNR of 18.3 dB. In comparison to 30 Gb/s TDM, our proposed system shows better sensitivity for U50 and U75, in the order of 1 dB.

Figure 4 shows the effect of chromatic dispersion to the performance of 30 Gb/s conventional TDM and 30 Gb/s TDM over AP-DCDM. Using AP-DCDM, all users show almost similar behavior of positive and negative chromatic dispersions. U25 and U50 have the same ability to tolerate chromatic dispersion of ±103.5 ps/nm while U75 has the dispersion tolerance of ±138 ps/nm at BER of 10-9. For the 30 Gb/s conventional TDM, dispersion tolerance is around ±86.5 ps/nm. This result shows that 30 Gb/s TDM over AP-DCDM is more robust to dispersion in comparison with 30 Gb/s conventional TDM. This is because of smaller spectral width of the former technique. The simulated time-averaged eye diagrams at various dispersions are shown in Figure 5.

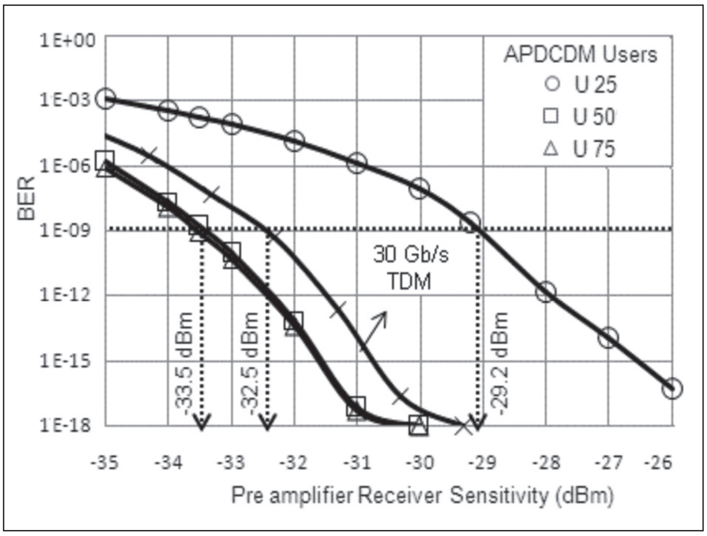

Figure 3: Pre-amplified receiver sensitivity for three channels 30 Gb/s TDM over AP-DCDM and 30 Gb/s conventional TDM

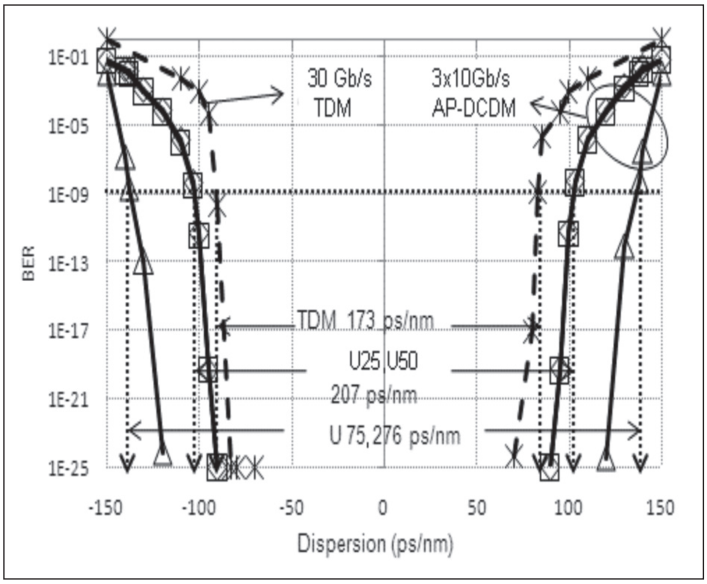

Figure 4: Chromatic dispersion tolerance comparison between AP-DCDM and TDM at the same transmission power

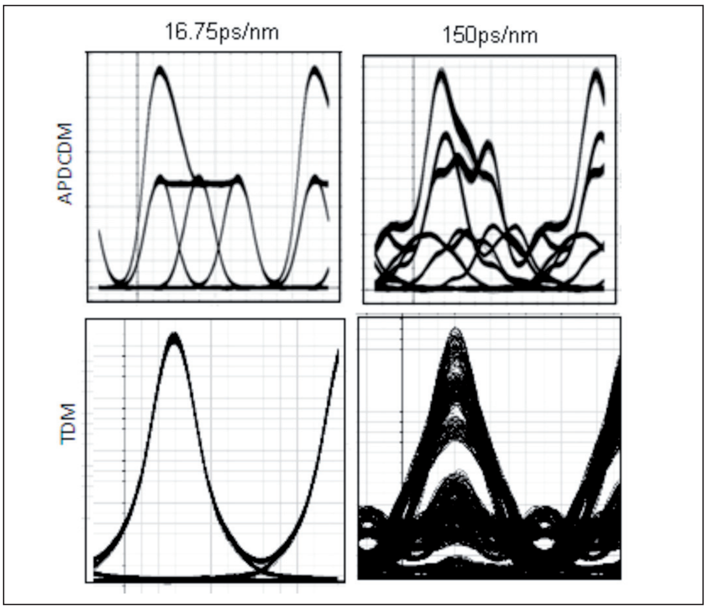

Figure 5: Eye diagrams for TDM over AP-DCDM and conventional TDM at different dispersions

5.0 CONCLUSIONS

The principle of the AP-DCDM technique and the proof of its viability are discussed. Using this electrical multiplexing or demultiplexing technique, more than two users can be carried over a WDM channel. Therefore, the capacity utilisation of the WDM channels can be increased tremendously at tolerable penalty. Performance of AP-DCDM was examined with back-to-back receiver sensitivity, OSNR and chromatic dispersion tolerance. AP-DCDM system shows better sensitivity for U50 and U75, in the order of 1 dB in comparison to conventional TDM at 30 Gb/s. For chromatic dispersion, AP-DCDM shows higher dispersion tolerance in comparison to conventional TDM at the same capacity. The results confirm the ability of AP-DCDM to become an alternative multiplexing technique in optical fiber communications. ■

REFERENCES

[1] T. H. Wood, G. C. Wilson, R. D. Feldman, and J. A. Stiles, "FiberVista: A Cost-Effective Fiber-to-the-Home (FTTH) System Providing Broad-Band Data Over Cable Modems Along with Analog and Digital Video", IEEE Photon. Technol. Lett., Vol.11, No.4 , Apr. 1999, pp. 475-477

[2] G. Charlet, E. Corbel, J. Lazaro, A. Klekamp, R. Dischler, P. Tran, W. Idler, H. Mardoyan, A. Konczykowska, F. Jorge, and S. Bigo, "WDM Transmission at 6 Tbit/s capacity over transatlantic distance, using 42.7Gb/s Differential Phase-Shift Keying without pulse carver", in Proc. OFC 2002, paper PDP36

[3] A. H. Gnauck, P. J. Winzer, S. Chandrasekhar, and C. Dorre, "Spectrally Efficient (0.8 b/s/Hz) 1-Tb/s (25 £ 42.7 Gb/s) RZ-DQPSK Transmission Over 28 100-km SSMF Spans With 7 Optical Add/Drops", in Proc. ECOC 2004, paper Th4.4.1

[4] N. Kikuchi, K. Sekine, and S. Sasaki, "Multilevel Signaling for High-speed Optical Transmission," presented at the 32nd European Conf. Optical Communication (ECOC), Cannes, France, Sep. 2006, Paper Tu3.2.1.

[5] R. A. Griffin, and A. and C. Carter, "Optical Differential Quadrature Phase-Shift Key (ODQPSK) for High Capacity Optical Transmission", in Proc. OFC 2002, paper WX6

[6] S.A.Aljunid, M.Ismail, A. R.Ramli, B.M.Ali, and M.K.Abdullah, "A New Family of Optical Code Sequences for Spectral-Amplitude-coding Optical CDMA Systems", IEEE Photonics Technology Letters, vol 16, issue 10, Oct. 2004, pp.2383-2385.

PROFILES

DR AMIN MALEKMOHAMMADI is a member of IEEE, IEEE-LEOS and Optical Society of America (OSA), received his PhD degree in Computer System Engineering (Optical Communications) at Universiti Putra Malaysia, 2009. Currently he is working at the Department of Electrical and Electronic Engineering, University of Nottingham as an assistant professor. He is also with the Georgia Green Institute for Electromagnetic Research, University of Nottingham, UK as an associate member. He has authored and co-authored 40 technical papers which include journals articles and conference proceedings. He has filed 3 patents for his inventions and scientific works.

IR. ASSOC. PROF. DR AHMAD FAUZI ABAS obtain his Doctor of Engineering (Dr-Ing.) from University of Paderborn, Germany in 2006. Since then, he joined the Department of Computer and Communication Systems Engineering, Faculty of Engineering, Universiti Putra Malaysia as a lecturer. Currently, he is an Associate Professor in the same department, where he leads the Photonic and Fiber Optics Systems Research Working Group. He has authored and co-authored around 100 technical papers, which include journal articles and conference proceeding. His research interest are in optical communications, devices and sensors.

STRENGTH AND DEFORMATION CHARACTERISTICS OF CEMENT TREATED SOFT BANGLADESH CLAYS

(Date received:5.4.2011/Date approved: 11.8.2011)

Md. Mokhlesur Rahman[1], Abu Taher Md. Zillur Rabbi[2] and Abu Siddique[3]
[1,2]*Department of Civil Engineering,*
Dhaka University of Engineering and Technology, Gazipur-1700, Bangladesh
[3]*Professor, Department of Civil Engineering,*
Bangladesh University of Engineering and Technology, Dhaka-1000, Bangladesh
E-mail: [1]mokhlesur_2005@yahoo.com, [2]sumonbitr@yahoo.com and *[3]abusid@ce.buet.ac.bd*

ABSTRACT

The strength and deformation characteristics of cement treated soft Bangladesh clays are evaluated through a series of experimental investigations. Based on the rate of strength development, the unconfined compressive strength and cement content relationship can be divided into 3 zones: Inactive Zone, Active Zone and Inert Zone. The stiffness of the cemented clay is a function of cement content and curing time, as the higher cement content and curing time results higher stiffness. The significant increase in apparent preconsolidation pressure and reduction in apparent compression index are observed from consolidation tests for cement treated clay. This implies that the treated clay undergoes structuration (formation of cementation bond) up to their apparent preconsolidation pressure and afterward the destructuration (breaking of cementation bond) takes place. Ductile behavior is associated with lower strength and higher failure strain (high unit deformation). On the contrary, higher strength and lower failure strain (low unit deformation) correspond to brittle behavior. Generally, higher cement content and curing time are the main parameters to cause the stabilised mass become brittle. Effective stress paths correspond to different category of states such as normally consolidated, lightly, moderately and heavily overconsolidated states depend on amount of cementation.

Keywords: *Cementation Bond, Deformation, Engineering Behavior, Fabric, High Water Content, Strength*

1.0 INTRODUCTION

Major geotechnical problems often arise for construction in Bangladesh involving soft clays containing high water content. Such soft clay formations are available in Bangladesh, especially when the in-situ water contents are high owing to its low shear strength and high compressibility [1]. There are three types of clay in Bangladesh on the basis of plasticity, namely high plastic (C1) clay, medium plastic (C2) clay and low plastic (C3) clay. Thus, suitable ground improvement techniques are needed for deep excavation projects in these soft clays to obtain strength stability and deformation control. Now a days, cement stabilisation is one of the commonly used methods of ground improvements. An increment in strength, reduction in compressibility (deformation) and improvement of swelling characteristics as well as reduction of creep properties of soil are the main aims of cement stabilisation method.

While the conventional cement stabilisation is mainly for surface treatment, the use of cement has recently been extended at greater depth in which cement column are being installed to act as a type of soil reinforcement [2 – 4]. These methods are termed as deep cement mixing and cement jet grouting which is currently being used in various countries to improve the strength and deformation properties of soft clay for most of the deep excavation projects. To improve the strength and deformation properties of cement treated soft clay soils, they are investigated in laboratories as model tests [5 – 9].

Normally, cement stabilisation work is carried out before the start of excavation. The improved soil layer functions as a strut acting below the excavation level, which helps in limiting the movement of soil mass. Hence, in this application, the strength and deformation characteristics of stabilised clay need to be model investigated in soil laboratory. Thus, the effects of cement inclusion on strength and deformation characteristics of soft Bangladesh clays are described in this paper, in order to have a better understanding on stress-strain, stiffness and compressibility characteristics of cement treated clays.

2.0 EXPERIMENTAL INVESTIGATION

2.1. Soil Sample

Clays were collected in various districts of Bangladesh such as C1 clay from Gazipur, C2 clay from Gopalgonj and C3 clay from Khulna. The soils were collected from depth of 2-3 m from existing ground level with disturbed and undisturbed state. Its physical and engineering properties are listed in Tables 1 and 2 respectively. ASTM Type I Portland cement was used as a binding material in this study. Samples were prepared from these clays and cement slurries.

Table 1: Characteristic values of the physical and index properties of the untreated base clays

Properties	Characteristics Values		
Type of Soil	C1 clay (LL > 50%)	C2 clay (LL = 35 to 50%)	C3 clay (LL < 35%)
Liquid Limit, LL, (%)	78	47	33
Plastic Limit, PL, (%)	31	25	20
Plasticity Index, PI, (%)	47	22	13
In-Situ Water Content, w_n (%)	70	62	53
Liquidity Index, LI	0.83	1.68	2.54
*Clay (%)	73	63	56
*Silt (%)	23	29	34
*Sand (%)	4	8	10
Bulk Unit Weight, γ_t (kN/m^3)	15.05	14.67	14.45
Dry Unit Weight, γ_d (kN/m^3)	8.85	9.05	9.44
Specific Gravity, G_s	2.680	2.673	2.668
Activity of clays, A_c	0.64	0.35	0.23
Degree of saturation, S_r (%)	89	84	78
Unified Soil Classification System	CH	CL	CL

Table 2: Characteristic values of the engineering properties of the untreated base clays

Properties	Characteristics Values		
Type of Soil	C1 clay	C2 clay	C3 clay
Unconfined Strength, q_u (kPa)	50	41	58.5
Strain at Ultimate Strength, ε_f (%)	3.67	3.65	4.00
Initial Void Ratio, e_o	1.81	1.96	2.10
Preconsolidation Pressure, p'_c (kPa)	70	65	61
Compression Index, C_c	0.737	0.781	0.863
Swell Index, C_s	0.124	0.127	0.131
Shear strength at po ' = 200 kPa, s_u (kPa)	98	92	89
Shear Strain at s_u, ε_u (%)	11	10.7	10.2

2.2. Methodology of Testing

The clay paste was passed through a 2-mm sieve for removal of shell pieces and other bigger size particles. The intentional increase in water content is to simulate the water content increase taking place in the wet method of dispensing cement admixture in deep mixing and the significant increase taking place in jet grouting. The clay with its water content corresponding to the above simulating conditions and the quantity of cement resulting in clay-water or cement ratio (*wc/c*) of 2, 2.5, 4, 7.5, 10, 15 and 30. They were thoroughly mixed so as to ensure uniform dispersion of the cementing agent although the clay-water mixture.

The clay-water content (w_i) that used in this study was 120%, 150%, 200% and 250%. The mixing time was arbitrarily fixed at 10 minute. Such a uniform paste was transferred to cylindrical split moulds of 50 mm diameter × 100 mm height and 75 mm diameter × 100 mm height with connecting 50 mm height top collars and bottom ended cap taking care to prevent any air entrapment. Cylindrical moulds of 50 mm diameter × 100 mm height were used to prepare specimens for unconfined compression tests and triaxial compression tests. On the other hand, cylindrical moulds of 75 mm diameter × 100 mm height were used to prepare specimens for consolidation tests.

After 24 hours the specimens were dismantled and they were wrapped with thick polythene bags and they were stored in a room of constant temperature and humidity until their respective curing time finished.

Unconfined compression (UC) tests were carried out after 1, 2, 4, 12, 24, 52 and 104 weeks of curing period. Consolidation and unconsolidated undrained (UU) triaxial compression tests were run on samples after 4 and 12 weeks of curing. The rate of vertical displacement applied in UC tests was 1 mm/min. The effective confining pressures, p_o' for UU test was 200 kPa. A back pressure of 100 kPa was maintained to ensure high levels of degree of saturation during the triaxial test.

2.3 Parameters

According to Miura *et al.*, and Horpibulsuk [5,6], the prime parameter governing the strength and deformation of cement treated clay has been proposed and which is designated as clay-water/cement ratio, *wc/c*. The clay water or cement ratio hypothesis was also introduced. It merits controlling the input of cement to attain the strength and deformation requirement with curing time and clay-water content.

The *wc/c* is defined as the ratio of initial water content of the clay (%) to the cement content (%). The cement content, *c* is the ratio of cement to clay by weight both reckoned in the dry state. To obtain the same value of *wc/c*, it is possible to vary the water content of the clay, or the amount of cement, or both as the case might be. In order to examine up to what extent the applicability of *wc/c* is varied; the water content of clay was varied over a wide range in this study.

3.0 RESULTS AND DISCUSSION

The test results of the strength and compressibility (deformation) characteristics of cement treated clays were discussed in the following sections:

3.1. Strength Characteristics

Unconfined compression tests were performed to determine the stress-strain and stiffness characteristics of cement treated clay. The experiments were conducted with cement content (c) varies from 4 to 60% and having curing periods of 1 to 104 weeks.

Table 3 shows the strength at 4 and 12 weeks with 120%, 150%, 200% and 250% mixing water and 7.5, 10 and 15 clay-water or cement ratios for C1, C2 and C3 clays. Test results show that the increases of cement content and curing time result in significant improvement of unconfined compressive strength as well as stiffness of the treated clay. Figure 1 illustrates the effect of cement content on unconfined compressive strength of treated C1, C2 and C3 clays with different clay-water/cement ratios and at different curing periods. It is found that for 1 weeks strength, the effect of initial water content seems to be significant at all ranges of cement content. However, for 4 weeks strength, the effect of initial water content of all clay-slurry is insignificant if the cement content is less than 30%. In case of cement content more than 30%, samples of C1 and C3 clays give the higher strength as compared to that of samples C2 clay with initial water content of 120%. For clay with high initial water content, the development of lower strength could be due to the lesser cement particles per unit volume of the treated mixture.

Table 3: Unconfined compressive strength q_u in kPa for cement treated clays

Clay-water content *wc* (%)	wc/c Ratio	Cement content *c* (%)	C1 Clay		C2 Clay		C3 Clay	
			Curing Time		Curing Time		Curing Time	
			4 w	12 w	4 w	12 w	4 w	12 w
120	7.5	16	399	533	291	405	339	438
	10	12	251	335	179	267	213	284
	15	8	149	226	106	172	126	180
150	7.5	20	383	528	277	395	318	429
	10	15	241	338	175	260	200	266
	15	10	143	217	124	169	138	185
200	7.5	26.67	381	520	272	390	314	421
	10	20	238	330	170	249	195	257
	15	13.33	134	207	95	155	112	165
250	7.5	33.33	379	511	268	401	311	409
	10	25	235	321	172	258	189	265
	15	16.67	124	187	88	160	108	166

Another possible reason of low strength development is due to the increase of average distance between the reacting clays and cement particles. The efficiency of the diffusion of calcium ion concentration also reduces with the increase in initial water content of the clay-slurry. The conclusion has been supported by the investigation of Chew *et al.* [8] for cement treated Singapore marine clay.

The above results also suggest that the difference between the 1 to 104 weeks strength is significant, except when cement content is less than 4%. As the formation of cementation bonds due to the hydration and cementation reaction increases with the increase in curing time, the rate of development of strength also increases.

Figure 1 also reveals that a larger rate of increase of unconfined compressive strength is noted with cement content in the range of 4 to 40%; while a smaller incremental rate of strength is observed for cement content more than 40%. This is observed for curing periods of 4 to 104 weeks however, the incremental rate of UC strength was found uniform in the case of 1 and 2 weeks samples. This is probably because of the cementation becomes mature after 4 weeks curing periods. Based on this observation, the unconfined compressive strength and cement content relationship can be divided into 3 zones; Inactive Zone, active Zone and Inert Zone.

The cement content up to 4% shows only very marginal improvement of unconfined compressive strength and is termed as inactive zone. This implies that a certain percentage of cement (more than 4%) is required to complete the hydration reaction between cement and clay particles. The end result of complete cementation is to increase the shear strength. The cement content between 4 to 40% is termed as active zone, as it shows significant improvement of strength with cement content. At this zone, the rate of hydration reaction is very high and thus the bridging (cementation) effect is very efficient.

Hence, the increased amount of cementation reaction products CSH (calcium silicate hydrate) and CASH (calcium aluminum silicate hydrate) caused a sharp increase in shear strength. Beyond the cement content of 40%, the rate of increase of strength reduces and seems to be asymptotic. Such region is referred here as inert zone. This is because of the completion of cementation reaction (pozzolanic reaction) due to the exhaustion of cement. It is also possible that the reactions are going on but the calcium ion solutes diffuse very slowly within the treated clay matrix such that no further improvement of strength is observed. Similar results of clay-cement matrix were observed by Kamaluddin [10] and Chew *et al.* [8].

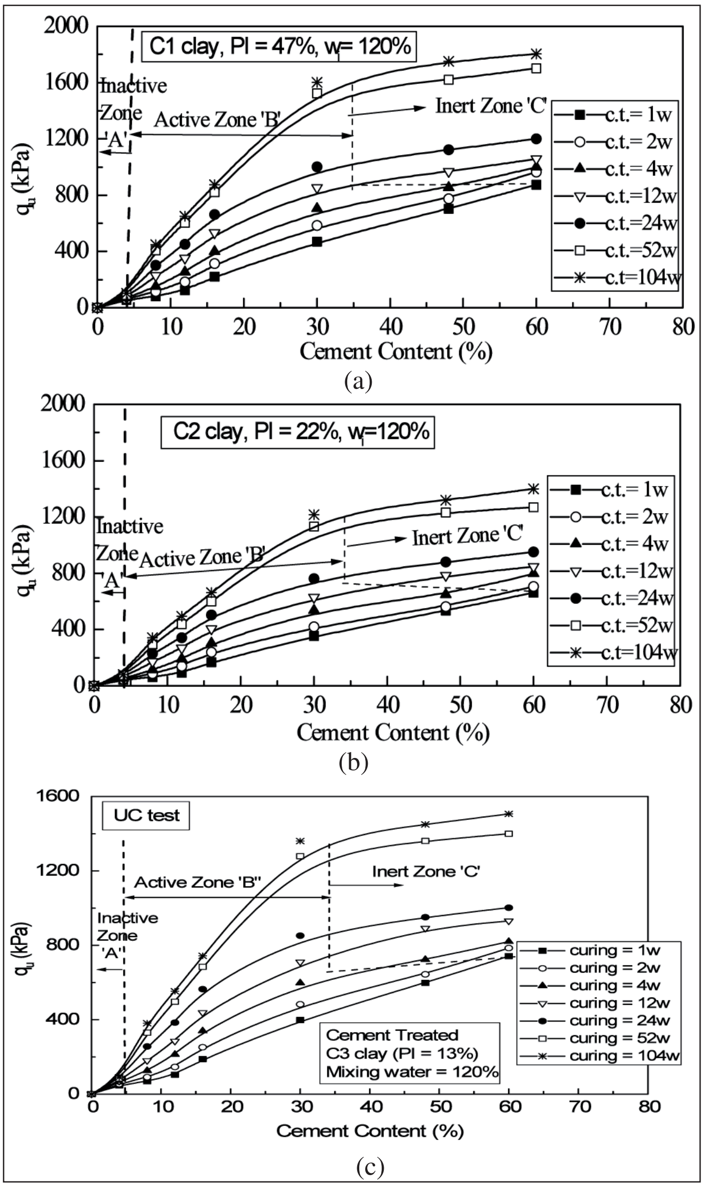

Figure 1: Unconfined compressive strength and cement content relationship at different curing periods (w_i = 120%) for (a) C1 clay, (b) C2 clay and (c) C3 clay

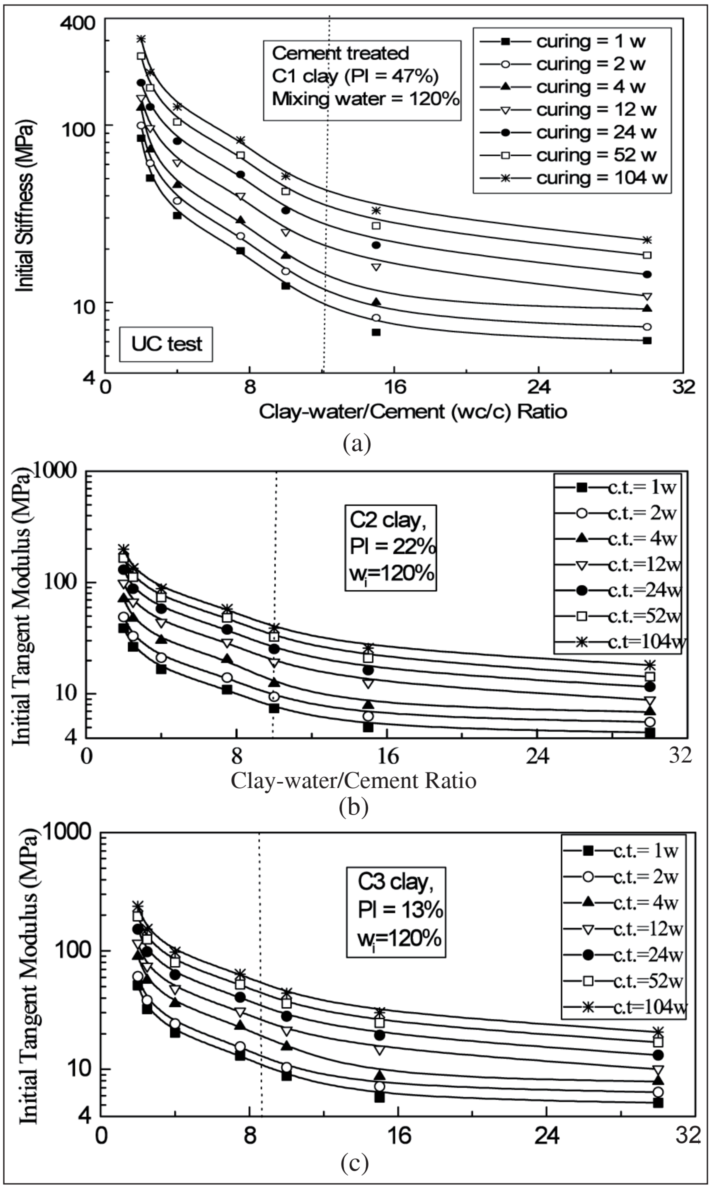

Figure 2: Relationship between initial tangent modulus and clay-water or cement ratio (w_i = 120%) for (a) C1 clay, (b) C2 clay and (c) C3 clay

3.2 Stiffness Characteristics

The stress-strain behavior of unconfined compression test for soils is generally non-linear. For this, initial stiffness or initial tangent modulus is defined as the slope of tangent at initial starting of non-linear stress-strain curve and simply abbreviated as E_i. The stiffness was found to be a function of clay-water or cement ratio, *wc/c* and curing time. Generally, higher *wc/c* ratio (i.e., lower cement content) and lower curing time correspond to the smaller values of the stiffness. Figure 2 show the relationship between initial tangent modulus and clay-water/cement ratio of treated samples of C1, C2 and C3 clays at mixing water content 120% used for clay slurries. A sharp increase of the modulus E_i can be noticed up to a *wc/c* ratio of 12, 10 and 9 for C1, C2 and C3 clays respectively and thereafter slow development occurs. The linear variations are attained at about *wc/c* 15 for all clays and high plastic clay undergoes high stiffness.

3.3 Compressibility (Deformation) Characteristics

Consolidation tests were carried out to explain the deformation characteristics of cement treated clay. Figures 3(a), (b) and (c) shows the $e\text{-}log\sigma_v'$ curve for the treated C1, C2 and C3 clays respectively. All three figures contain a $e\text{-}log\sigma_v'$ curve of corresponding remoulded specimen.The figures show that treated clay curves cross the untreated reconstituted clay curve before its preconsolidation pressure (σ_p') / yield stress (σ_y') and then it is displaced from the untreated reconstituted clay curve (dotted line) with increasing values of effective vertical pressure, indicating instinct characteristics of lower compressibility (deformation) of the treated mass. Beyond the σ'_p value, obviously, higher compressibility (deformation) can be noticed and at higher pressure levels, the treated clay curve tends to proceed parallel to the lower part of the untreated clay curve.

The compressibility of the untreated reconstituted sample is much steeper than those exhibited by the treated clays. The compression index (C_c) and swell index (C_s) are the slope of the ($e\text{-}log\sigma'_v$) plot at post yield stress during loading and unloading conditions respectively. The yield stress is obtained as the point of intersection of two straight lines extended from the linear portions on either end of the compression curve plotted as e against $log\sigma'_v$ [6].

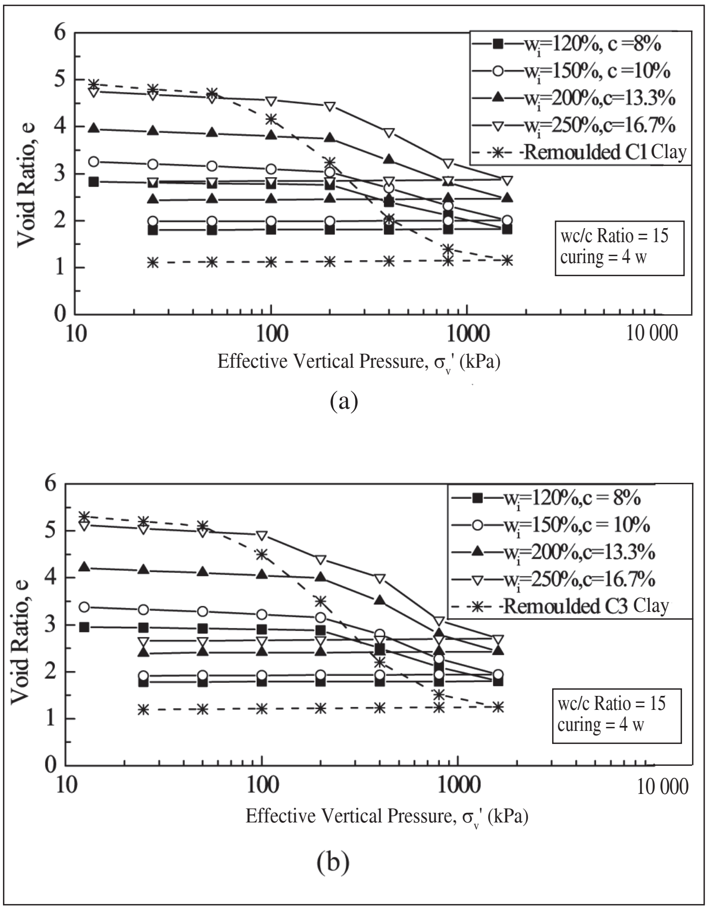

Figure 3: Void ratio-vertical stress relationship of treated and untreated clays at loading and unloading conditions for (a) C1 clay and (b) C3 clay

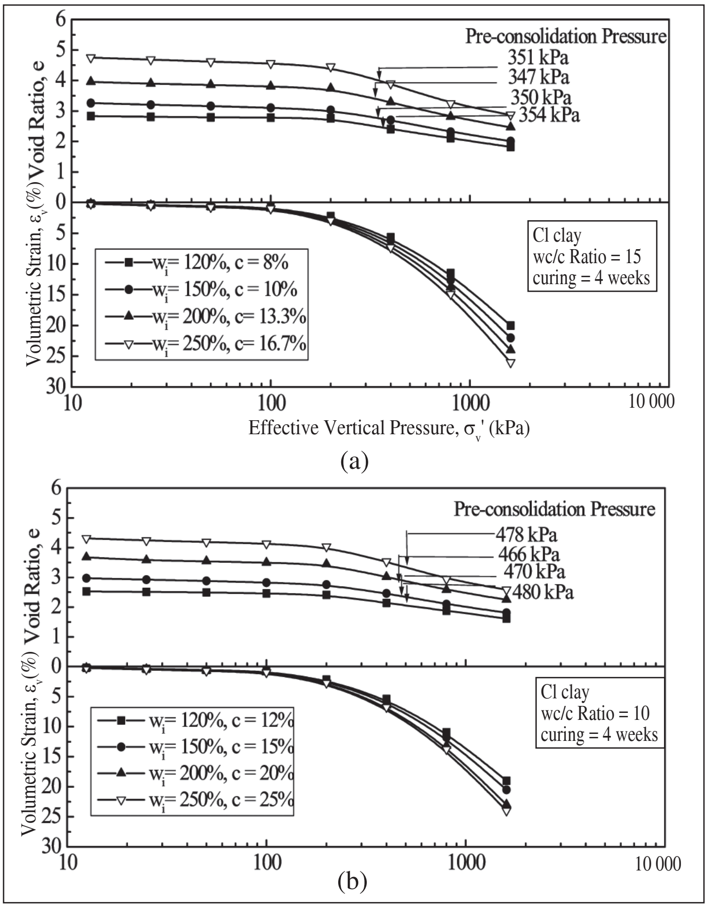

Figure 4: Compressibility of cement-stabilised clays for C1 clay and curing, 4 weeks at wc/c ratio (a) 15 and (b) 10

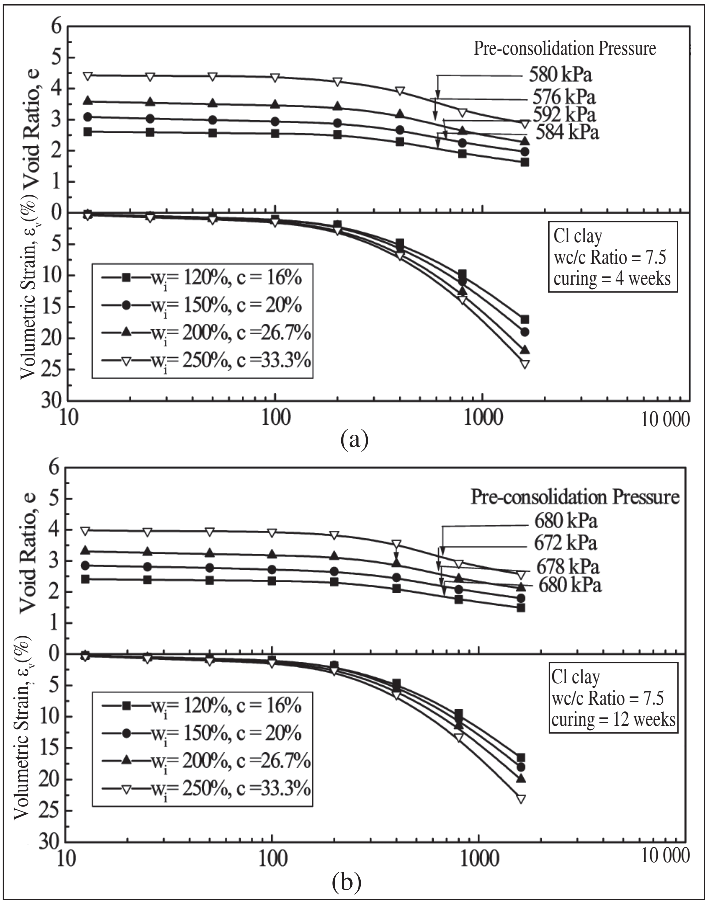

Figure 5: Compressibility of cement-stabilised C1 clays and wc/c ratio, 7.5 at curing (a) 4 weeks and (b) 12 weeks

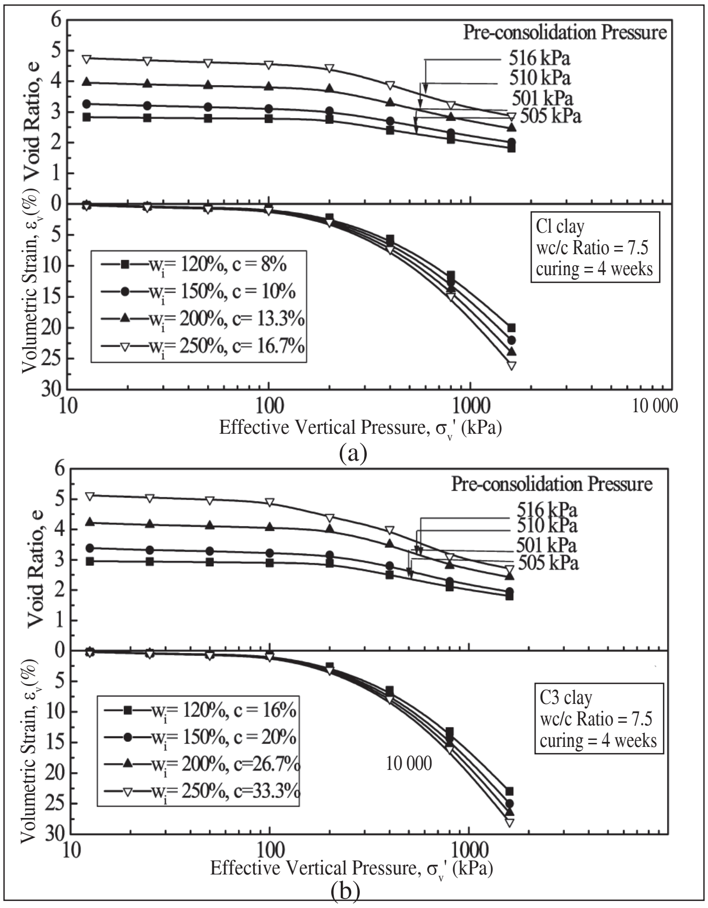

Figure 6: Compressibility of cement-stabilised clays at wc/c ratio, 7.5 and curing, 4 weeks for (a) C2 clay and (b) C3 clay

Figures 4 to 6 shows the *e-logσ'*$_v$ and ε_v*-logσ'*$_v$ relationships of different treated clay samples with *wc/c* ratio 7.5, 10 and 15 and mixing clay-water content (w_i), 120%, 150%, 200% and 250%. Table 4 shows the result of σ_y', C_c and C_s for C1, C2 and C3 clays at a curing period of 4 and 12 weeks. It is found that consolidation properties improved greatly by increasing the cement content and curing time. The addition of cement content increases the yield stress from about 61 to 70 kPa for the untreated clays and 350 to 680 kPa for the treated clays. The void ratio for C1 clay is lower than that of C3 clay but the void ratio for C3 clay is higher than that of C2 clay while the yield stress for C1 clay is higher than that of C3 clay however, the yield stress for C3 clay is higher than that of C2 clay. The increase of apparent yield stress is due to the effect of structuration (existing of cementation bond) of treated clay particles. Test results reveal that the void ratio of the treated samples practically changes very small amount until reach the apparent yield stress. This implies that due to the effect of structuration, the volumetric compressibility of the treated samples is very small and the stiffness is very high as long as it is within its yield stress range. The *e-logσ'v* relationship graph also shows that beyond the apparent yield stress, the behavior of treated samples is almost parallel to the untreated clays. This could be due to the destructuration (breaking of cementation bond) of the cementation effect of the treated clay matrix when it is stressed beyond the yield stress. The conclusion is also similar to that observed by Miura et al. [5].

3.4 Compression Index (C_c) and Swell Index (C_s)

The deformation (compressibility and swelling) characteristics of treated clays are found to be quite different from the untreated ones. Test results show that the compression index and swell index reduce significantly due to the effect of cement inclusion in soft clay. This observation implies that the treated clay sample is consistent with the heavily over-consolidated soil behavior. The deformation characteristics of different treated clays in terms of C_c and C_s are calculated for different clay-water or cement content as shown in Figures 7 and 8 for 4 and 12 weeks curing time respectively. It is found that C_c value decreases significantly with the increase in cement content (decrease for *wc/c* ratio). For the specimens with *wc/c* ratio 10 or less, the reduction of C_c and C_s values are very marginal, more pronounced and approaching to zero. However, at *wc/c* ratio 10 or more, almost smaller change of C_c and C_s are noticed. It is also noted that the compression index (C_c) of untreated clay is much smaller than that of the treated clay samples, while swell index (C_s) of untreated clay is higher than that of treated clay samples. This observation has been consistent with the findings of Chew et al. [7] which showed that during virgin yielding, the structured soil is less compressible than the reconstituted soil. This suggests that at higher stresses (beyond the apparent yield stress), the treated samples exhibit normally consolidated behavior with larger C_c. The effect of curing time on compression indices is rather significant.

Table 4: Compressibility parameters for cement stabilised clays

Curing (weeks)	w_i (%)	*wc/c* Ratio	C1 clay (PI = 47%)			C2 clay (PI = 22%)			C3 clay (PI = 13%)		
			σ_y' (kPa)	C_c	C_s	σ_y' (kPa)	C_c	C_s	σ_y' (kPa)	C_c	C_s
4	120	7.5	584	0.822	0.004	505	0.855	0.007	525	0.882	0.009
		10	480	0.856	0.005	417	0.886	0.008	457	0.916	0.010
		15	354	0.933	0.006	305	0.963	0.009	338	0.982	0.012
	150	7.5	592	0.893	0.008	501	0.912	0.009	527	0.991	0.011
		10	470	0.906	0.009	426	0.943	0.011	450	1.082	0.013
		15	350	0.968	0.011	308	0.995	0.013	340	1.115	0.015
	200	7.5	576	0.992	0.010	510	1.065	0.014	522	1.154	0.016
		10	466	1.111	0.012	411	1.121	0.016	455	1.203	0.019
		15	347	1.126	0.014	311	1.148	0.018	336	1.228	0.021
	250	7.5	580	1.155	0.014	516	1.88	0.018	527	1.213	0.021
		10	478	1.188	0.015	414	1.201	0.020	447	1.261	0.024
		15	351	1.194	0.017	306	1.213	0.022	338	1.311	0.026
12	120	7.5	680	0.806	0.003	634	0.832	0.005	650	0.849	0.007
		10	538	0.823	0.004	501	0.866	0.006	521	0.877	0.008
		15	460	0.848	0.005	422	0.943	0.008	436	0.961	0.010
	150	7.5	678	0.857	0.007	629	0.903	0.008	644	0.945	0.009
		10	534	0.875	0.008	506	0.916	0.009	526	0.966	0.011
		15	454	0.946	0.009	418	0.978	0.011	441	1.003	0.013
	200	7.5	672	0.915	0.009	631	0.102	0.012	652	1.142	0.014
		10	541	0.928	0.011	502	1.113	0.014	529	1.182	0.016
		15	450	0.998	0.013	420	1.128	0.016	445	1.204	0.019
	250	7.5	680	1.101	0.012	638	1.157	0.016	657	1.181	0.019
		10	531	1.131	0.013	509	1.189	0.018	536	1.225	0.021
		15	443	1.154	0.015	416	1.196	0.019	438	1.287	0.024

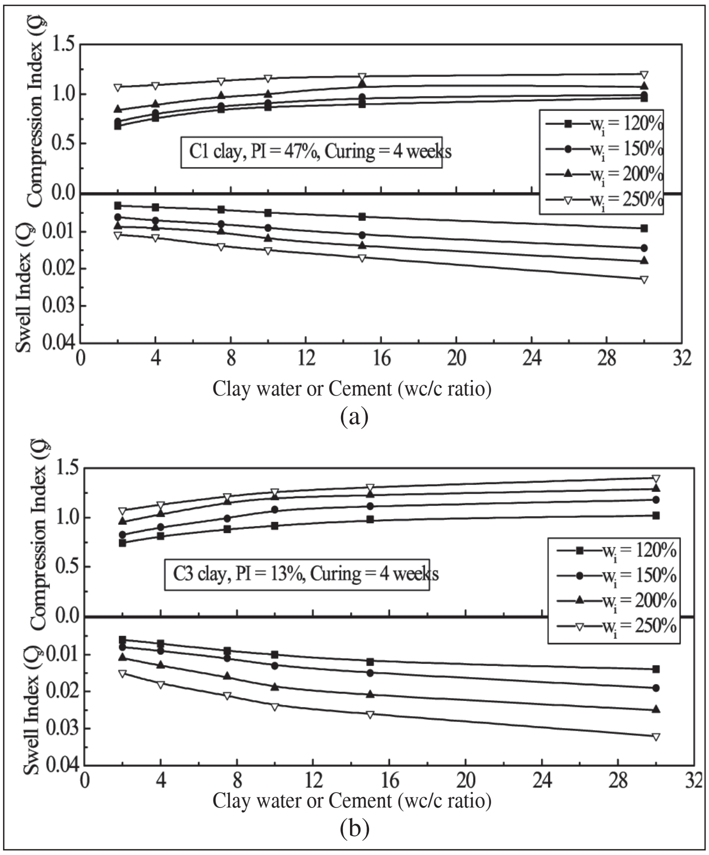

Figure 7: Effect of clay-water or cement ratio on compression and swell indices of treated clays for (a) C1 clay and (b) C3 clay (curing = 4 w)

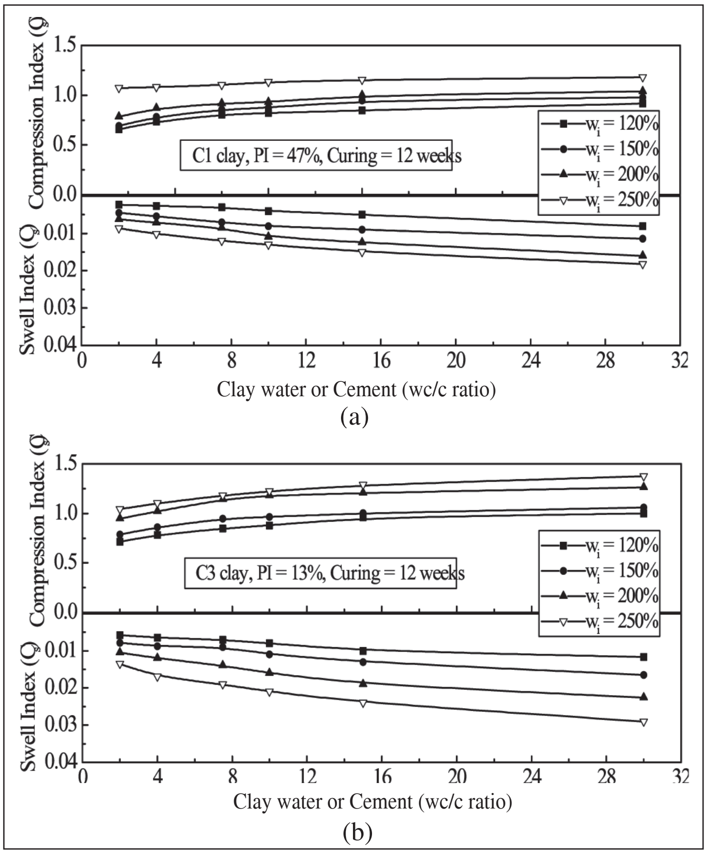

Figure 8: Effect of clay-water or cement ratio on compression and swell indices of treated clays for (a) C1 clay and (b) C3 clay (curing = 12 w)

The compression index and swell index decreases with increasing curing time. For treated clays, the apparent compression index increases with the increase in vertical stresses up to their apparent yield stress, and thereafter decreases. This implies that the treated clay undergoes structuration (formation of cementation bond) up to their apparent yield stress and afterward the destructuration (breaking of cementation bond) takes place. This result is also agrees with the results from the investigations of Chew *et al.* [8] for cement treated Singapore marine clay.

3.5 Stress-strain Characteristics

The stress-strain behavior of cement treated clay samples with curing time 4 and 12 weeks obtained from unconsolidated undrained (UU) triaxial compression tests are shown in Figures 9(a) and 9(b) respectively while Figures 10(a) and 10(b) show the stress-strain behavior from unconfined compression (UC) tests. The test results are described with comparing stabilisation effect for clay-water or cement (*wc/c*) ratio and curing time on strength (maximum stress at which sample failed) and strain (i.e., deformation per unit length).

Table 5 shows a comparison for strength and failure strain (failure unit deformation) from UC and UU tests of C1, C2 and C3 clays. The UU triaxial compression test results are compared with unconfined compression test results, it is found that strengths for UU triaxial compression test are increased to about 1.2 times than that of unconfined compression test but strains (unit deformation) for UU triaxial compression test are increased to about 2 times than that of unconfined compression test. The results for UU triaxial compression test are increased because the specimens are tested in a confined pressure state.

From Table 5, it is observed that C1 clay gained more strength than that of C3 clay, on the other hand, C3 clay gained more strength than that of C2 clay. In general, the stress-strain curves of the treated samples were found to increase abruptly up to the peak deviator strengths then suddenly decreased to low residual values upon further straining. The overall behavior of the treated samples can be categorised into brittle, quasi-brittle and ductile types. Brittle and quasi-brittle characteristics were observed for higher cement content such as wc/c ratio 7.5 and 10, rendering a comparatively lower value of strain at maximum strength (qmax) whereas ductile characteristics were observed for lower cement content such as wc/c ratio 15 and 30. Ductile samples were observed to be associated with a mild peak whereas brittle samples were observed to be associated with a sharp peak. The samples with higher cement content and curing time were observed to possess brittle behavior accompanied with low values of strains at qmax. The brittle samples always exhibited sharp peaks associated with abrupt falling characteristics. The residual strain of the brittle sample is much lower than that of the ductile sample.

It reveals that the lower the wc/c ratio, the greater the enhancement of the cementation bond strength inducing higher strength. The test results also show that the engineering behavior of cement-stabilised clay is dependent upon the clay-water or cement ratio (wc/c) and fabric (type of clay). For the improvement of soft Bangladesh clay at high water content by cement admixture form UC and UU tests, it is concluded that high plastic clay undergoes better improvement than low plastic clay but low plastic clay undergoes better improvement than medium plastic clay.

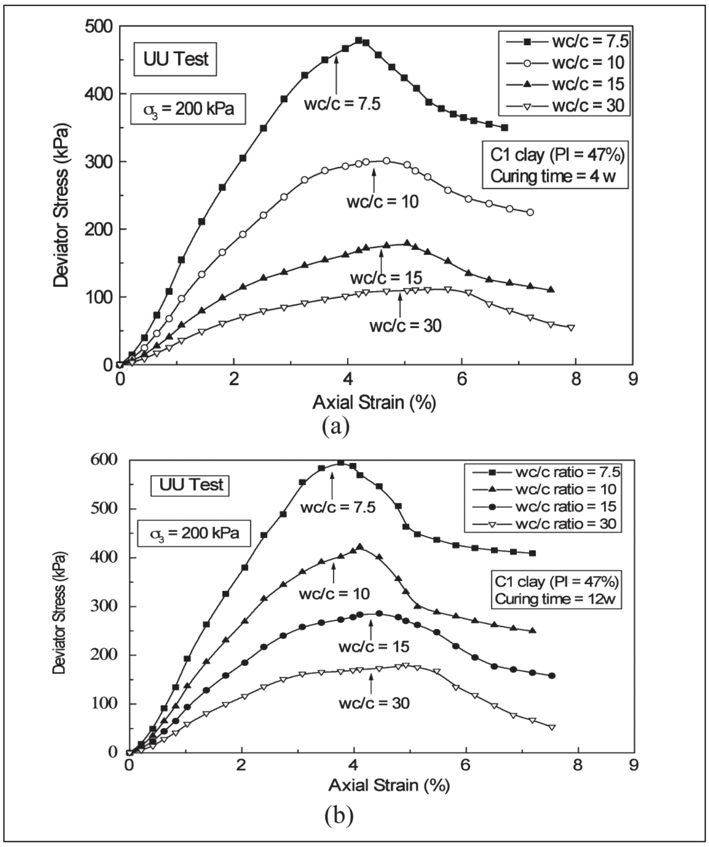

Figure 9: Stress-strain typical relationships of cement-stabilised C1 clays from UU test at different wc/c ratio for curing (a) 4 weeks and (b) 12 weeks

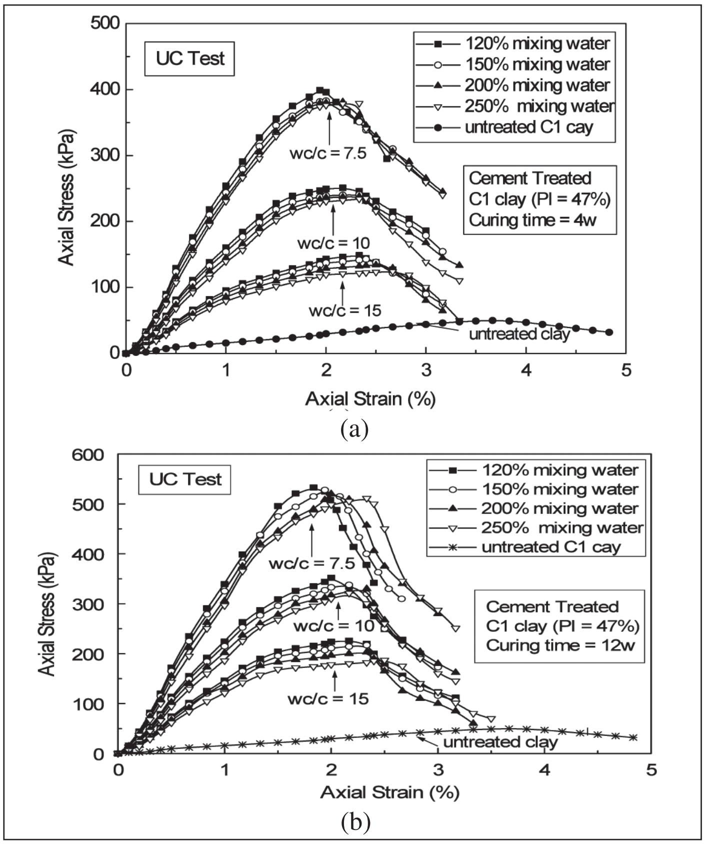

Figure 10: Stress-strain typical relationships of cement-stabilised C1 clays from UC test at different wc/c ratio for curing (a) 4 weeks and (b) 12 weeks

Table 5: Comparison of undrained shear strength and axial strain at failure of cement treated clays (w_i = 120%) from UC and UU tests (σ3 = 200 kPa)

Curing Time (week)	Clay Type	wc/c Ratio	Undrained Shear Strength (kPa)		Axial Strain at Failure (%)	
			UC test	UU test	UC test	UU test
4 w	C1	7.5	200	240	1.94	1.83
		10	126	151	2.16	2.00
		15	75	93	2.33	2.17
		30	34	56	2.69	2.46
	C2	7.5	146	174	2.67	2.50
		10	92	108	2.85	2.67
		15	53	64	3.00	2.83
		30	27	45	3.23	3.01
	C3	7.5	170	219	2.40	2.33
		10	107	142	2.50	2.50
		15	63	91	2.83	2.67
		30	32	48	3.15	2.93
12 w	C1	7.5	267	299	4.19	3.76
		10	168	211	4.68	4.11
		15	113	143	5.04	4.45
		30	38	89	5.76	4.92
	C2	7.5	203	237	5.26	5.00
		10	134	160	5.64	5.14
		15	86	103	6.02	5.36
		30	30	69	5.64	6.43
	C3	7.5	219	254	5.54	4.67
		10	142	194	5.61	5.10
		15	90	129	5.94	5.41
		30	35	82	6.7	6.02

3.6 Undrained Stress Path Characteristics

The effective stress paths are defined the path of straight lines or curve lines by plotting the deviator stress versus mean effective stress. Figures 11(a) and 11(b) illustrate the undrained effective stress paths for cement treated C1 and C3 clays respectively. Overall view of the figures seems to indicate that originated from the same untreated samples possessing normally consolidated state. Figure 11 consists of stress paths of treated clays for $p_o' = 200$ kPa.

The stress paths evidently, belong to different category ranging from a low OCR (over-consolidation ratio) value to a high OCR value. These stress paths, corresponds to different category of states such as normally consolidated, lightly, moderately and heavily over-consolidated state; though all of the samples have a cement content value. The clay-water or cement ratios are used 7.5, 10, 15 and 30 with mixing water content 120% for each clay.

Effective stress paths for treated clays are similar to that of normally consolidated state for high wc/c ratio up to 30 (i.e, low cement content up to 4%), lightly over-consolidated state for wc/c ratio up to 15 (i.e, cement content up to 8%), moderately over-consolidated state for *wc/c* ratio up to 10 (i.e, cement content up to 12%) and heavily over-consolidated state for wc/c ratio up to 7.5 (i.e, high cement content up to 16%). Very small pore pressures are developed and the stress paths propagate approximately at constant-*po'*, i.e., sub-parallel to *q*-axis. Such a behavior is generally found from natural over-consolidated clays and this type of aspect strongly supports the elastic wall concept of the Cambridge stress-strain theories; the specimens remaining on elastic wall exhibits constant plastic volumetric strain [6].

4.0 STRENGTH AND DEFORMATION RELATIONSHIP

Figure 12 illustrates the relation between *εf* (failure strain i.e., failure unit deformation) and *qu* (unconfined compressive strength) in an arithmetic plot in terms of *wc/c* ratio of cement stabilised samples for C2 clay while Figure 13 illustrates the relation between *εf* and *qu* in terms of curing time of cement stabilised samples for C3 clay. Such figures are meaningful to delineate the ductile and brittle behavior of the samples. The relationship has produced a definite trend of reduction of failure strain (unit deformation) with incremental values of cement content and curing time. At higher values of *wc/c* ratio such as 30 (i.e., lowest cement content such as 4%), significant large failure strains whereas samples with low strength produce higher values of *εf* with constraint in a narrow band. These samples exhibit ductile behavior during shearing.

Ductile behavior is associated with low strength and higher failure strain (unit deformation). On the contrary, higher strength and low failure strain (unit deformation) correspond to brittle behavior. Generally, higher cement content and curing time are the main parameters to cause the stabilised mass brittle. In Figures 12 and 13, the brittle characteristics can be seen at relatively higher values of *qu*, where samples cluster along the best fit line.

On the other hand, ductile behavior can be observed at the region of relatively lower values of *qu* where samples show comparatively less wide scatter. The best fit line shows the required expressions with coefficients of correlation greater than 0.90.

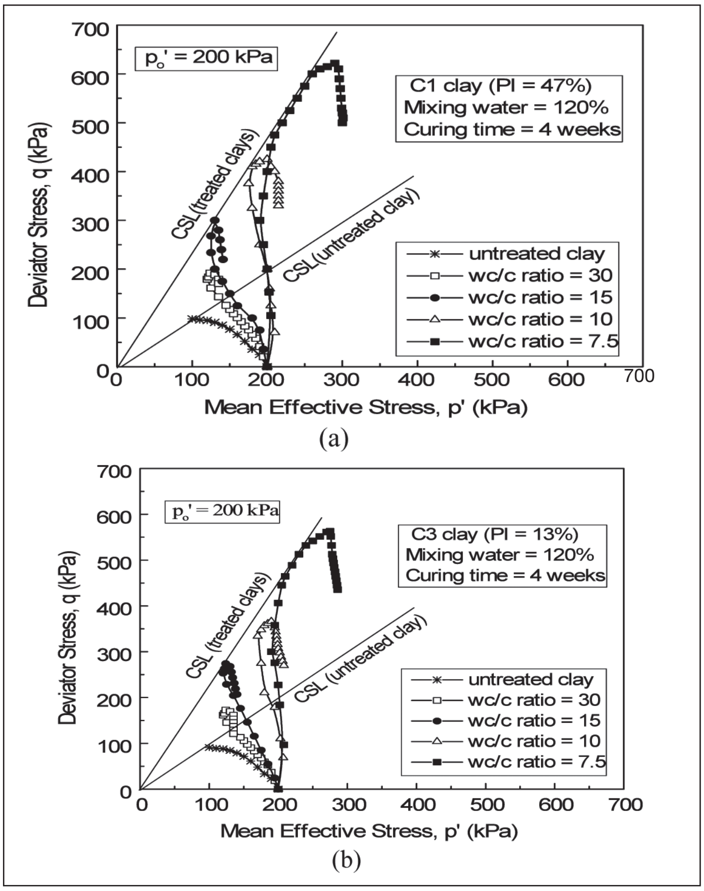

Figure 11: Undrained stress paths of cement treated clays (a) C1 clay and (b) C3 clay

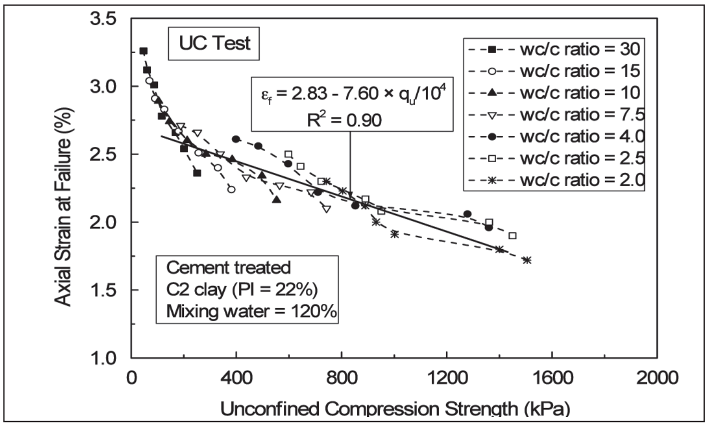

Figure 12: Relationship between qu and axial strain at failure shown in terms of wc/c ratio for cement treated C2 clay

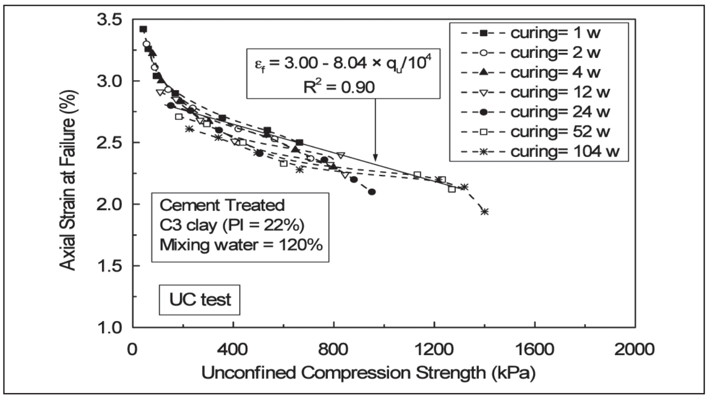

Figure 13: Relationship between qu and axial strain at failure shown in terms of curing time of cement treated C3 clay

The expressions for relation of εf (in %) and qu (in kPa) plot in terms of *wc/c* ratio for cement stabilised Bangladesh clays are linear equations as follow:

$\varepsilon_f = 2.34 - 7.01 \times q_u/10^4$ for high plastic (C1) clay

$\varepsilon_f = 3.00 - 8.04 \times q_u/10^4$ for medium plastic (C2) clay and

$\varepsilon_f = 2.83 - 7.60 \times q_u/10^4$ for low plastic (C3) clay

The mathematical expressions show that C1 clay has achieved lower failure strain than that of C2 clay and C3 clay. While, Kamaluddin [10] reported that the relationship (ε_f, q_u) for cement stabilised Bangkok clay at low mixing water content, such as $\varepsilon_f = 3.3 - 19 \times q_u/10^4$.

5.0 CONCLUSIONS

Strength and deformations characteristics of cement treated soft Bangladesh clays are studied through a series of unconfined compression, consolidation and unconsolidated undrained triaxial compression tests. From the test results, the following conclusions can be drawn:

i) The unconfined compressive strength and stiffness of cement treated Bangladesh clay increases with the increase of cement content and curing time. The resulting effect of improvement of strength leads to the formation of more structured for cemented clay.

ii) Cement content of less than 4% does not show any effective improvement of strength and deformation properties of soft Bangladesh clays however, beyond 4% and up to 40% cement content can be envisaged as Active Zone. Beyond 40% cement content is defined as Inert Zone. These zonal demarcations are observed only for 4 weeks curing periods. However, further investigation needs to be conducted to verify the extended range of Inert Zone by adding higher cement content and at longer curing periods.

iii) The significant increase in apparent pre-consolidation pressure (pc')/yield stress ($\sigma y'$) and reduction in volumetric strain are observed from consolidation tests of cemented clay samples at in-situ stress range. This is due to the structuration (existing of bond strength) of clay particles due to the inclusion of cement. The consolidation behavior of cemented clay seems to be consistent with that of the over-consolidated clays. This implies that the cemented clay undergoes structuration up to their yield stress and then the progressive destructuration (breaking of bond strength) takes place.

iv) The higher the value of cement content (lower *wc/c* ratio), the greater is the enhancement of the yield stress and decrease of compression index and swell index accompanied with gradual reduction of compressibility. The (εv, $\log\sigma' v$) relationships show that the higher the cement content and curing time, the lower the volumetric strain incurred by the cemented sample.

v) The reduction in compression index (C_c) and swell index (C_s) are observed from consolidation tests of cemented clay samples at in-situ stress range. This is due to the structuration of clay particles due to the inclusion of cement. The swelling behavior of cemented clays seems to be consistent with that of the overconsolidated clays.

vi) The characteristic shape of (q-εs) curve also suggests that the deviator stress increases to a peak value and then strain softens to a lower residual value. The stress paths evidently explain the strength and deformation behavior of clays that belong to different category ranging from a low OCR (over-consolidation ratio) value to a high OCR value. These stress paths, correspond to different category of states such as normally consolidated, lightly, moderately and heavily over-consolidated state depend on amount of cementation.

vii) For the improvement of soft Bangladesh clay at high water content by cement admixture in shallow and deep foundations, in which the water content of the clay varies from 120% to 250%, the *wc/c* value is the prime parameter governing the engineering behavior of cement stabilised clays both in considered strength and deformation behavior, whereas the effect of fabric can be negligible.

viii) Ductile behavior is associated with low strength and higher failure strain (unit deformation) while, higher strength and low failure strain (unit deformation) correspond to brittle behavior.

ix) The relations between unit deformation i.e., strain, εf (in %) and strength, qu (in kPa) plot in terms of *wc/c* ratio can be expressed as:

$\varepsilon_f = 2.34 - 7.01 \times q_u/10^4$,
$\varepsilon_f = 3.00 - 8.04 \times q_u/10^4$ and
$\varepsilon_f = 2.83 - 7.60 \times q_u/10^4$

for stabilised high, medium and low plastic clays respectively.

x) For the improvement of soft Bangladesh clay at high water content by cement admixture, it is concluded that high plastic clay undergoes better improvement than low plastic clay. However, low plastic clay undergoes better improvement than medium plastic clay. ■

REFERENCES

[1] A. Siddique, A. M. M. Safiullah, and M. A. Ansary, (2002). “Characteristic features of soft ground engineering in Bangladesh”, Proceedings of Int. Symposium, Japan, Vol. 2, pp. 231-248.

[2] F. Tatsuoka, Y. Fohata, K. Uchida, and K. Imai (1996). “Deformation and strength characteristics of cement treated soils in Trans-Tokyo Bay Highway Project”, Grouting and Deep Mixing, Proc. of the IS-Tokyo 96, 2nd Int. Conf. on Ground Improvement Geosystems, Tokyo, pp. 453-459.

[3] H. Hashizume, Y. Okochi, J. Dong, N. Horii, Y. Toyosawa, and S. Tamate (1998). “Study on the behavior of soft ground improved using DMM.” Proc: Int. Conf. on centrifuge 98, IS-Tokyo 98, pp. 851-856.

[4] A. Probaha, S. Shibuya, and T. Kishida (2000). “State of the art in deep mixing technology, Part III: geomaterial characterization”, Ground Improvement, Thomas Telford Ltd., Japan: Vol. 3, pp. 91-110.

[5] N. Miura, S. Horpibulsuk, and T. S. Nagaraj (2001). “Engineering behavior of cement stabilized clay at high water content”, Soils and Foundation, Japanese Geotechnical Society, Japan. 41 (5): 33-45.

[6] S. Horpibulsuk (2001). “Analysis and assessment of engineering behavior of cement stabilized clays”, Ph.D. Dissertation, Saga University, Saga, Japan.

[7] S. H. Chew, A. H. M. Kamruzzaman, and F. H. Lee (2001). “Strength and deformation characteristics of cement treated marine clay”, Proceedings of the 14th SE Asian G. Conf., Hong Kong, 285-290.

[8] S. H. Chew, A. H. M. Kamruzzaman, and F. H. Lee (2004). “Physicochemical and engineering behavior of cement treated clays”, Journal of G. and Geo-Env. Engineering, ASCE, 130(7), 696-706.

[9] M. R. Mokhlesur, (2008). "Investigation of strength and deformation characteristics of cement and lime treated soft clays", Ph. D. Thesis, BUET, Dhaka, Bangladesh.

[10] M. Kamaluddin (1995). “Strength and deformation behavior of cement-treated Bangkok clay.” Ph. D. Thesis, AIT, Bangkok, Thailand.

PROFILES

PROF. MD. MOKHLESUR RAHMAN is currently a professor in the Department of Civil Engineering in Dhaka University of Engineering and Technology (DUET), Bangladesh. He received B. Sc. Eng. (Civil) and M. Sc. Eng. (Geotechnical) and Ph. D. (Geotechnical) from BUET. His research interests include soil investigation, soil sampling and strength-deformation characteristics of chemically modified cement and lime stabilised clays.

MR. ABU TAHER MD. ZILLUR RABBI is an Assistant Professor in the Department of Civil Engineering in Dhaka University of Engineering and Technology (DUET), Bangladesh. He received B. Sc. Eng. (Civil) from RUET, Rajshahi, Bangladesh and M. Sc. Eng. (Civil and Geotechnical) from Saitama University, Japan. His research interest includes soil improvement, laboratory based element and model tests of soil, small strain stiffness properties, dynamic properties of soil, geotechnical earthquake engineering.

PROF. ABU SIDDIQUE is a Professor, the Department of Civil Engineering and Controller of Examination, Bangladesh University of Engineering and Technology (BUET). He holds B. Sc. Eng. (Civil), BUET; M. Sc. Eng. (Geotechnical), BUET; Ph.D. (Geotechnical), University of Surrey, U.K. His research interests include stress-deformation and stiffness characteristics of clays, geotechnical behavior of stabilised and expansive soils.

A METALLURGICAL STUDY OF SPOT WELD GROWTH ON MILD STEEL WITH 1MM AND 2MM THICKNESSES

(Date received:24.3.2011/Date approved:19.9.2011)

Aravinthan Arumugam[1] and Nachimani Charde[2]
[1,2]Department of Mechanical, Material and Manufacturing Engineering,
The University of Nottingham (Malaysia Campus), Jalan Broga,
43500 Semenyih, Selangor
E-mail: [1]nachi.charde@nottingham.edu.my

ABSTRACT

Resistance Spot Welding (RSW) is an important welding technology for joining two or more metals in various manufacturing industries. For instance, to date a car may contain an average of 3000-4000 spot weld joints and the nuggets' joints are very important between metal sheets to ensure the aging factor of mechanical assemblies. As such the growths of spot welds create significance and it is determined by its' main controlling parameters such as: current, weld time and force. However factors such as electrode deformation, dissimilar materials, materials with different thicknesses and corrosions are also affect weld growth. This study was conducted to look into the effects of different thickness (1 mm and 2 mm) on weld nugget growth of mild steel. The tensile test and hardness test have been carried out to characterise the formation of weld nugget growth for different weld schedules. The results of the experiments showed that the growth of spot weld nuggets was affected by different thicknesses. The microstructures of weld nuggets have also shown distinguishable differences in weld growth for the both 1 mm and 2 mm thicknesses. The results have shown difference in yield strength as well, for the same welding schedules. This was happened due to the difference of resistive path of two thicknesses.

Keywords: *Mild Steel Weld Nuggets, Mild Steel Different Thicknesses*

1.0 INTRODUCTION

Spot welding process is a joining process that joins two or more metal sheets together through fusion at a certain point [1]. It is a simple process that uses two copper electrodes to press the work sheets or base metals together and forces a high current to pass through it. The growth of weld nugget is then determined by its controlling parameters i.e., the current, force and weld time [2]. The other factors that influence the weld growth are electrode deformation, material properties, corrosion, gaps between work sheets and what not [3].

Automotive industry is one of the main industries that have been using spot welding mechanism to join its metal structures for long time. To date, a car's body may contain an average of 3000 to 4000 spot weld joints which do not alter the weight of materials very much as compared to traditional arc welding. The other industries such as marine, bridge and road, high rise buildings and aircraft engineering are also primarily anticipating the spot welding process for its small scale metal assemblies. So far the researchers have done many researches on spot welding for various materials such as low carbon steel, nickel, aluminum, titanium, copper alloy, stainless steel, austenitic stainless steel, galvanised low carbon steel, zinc coated steel, magnesium alloy and high-strength low alloy steel [1-6].

This research was focused on the spot weld growth of the low carbon mild steel and investigates the ability of producing sound welds as the metal seemed to be very common and cheap as compared to others. The welded specimens were later tested using tensile-shear [3-4] test and hardness test [5-6] to characterise the formation of weld nuggets of low carbon mild steel.

2.0 EXPERIMENT

The formation of weld is mainly influenced by controlling-parameters of spot welding process, as stated before. In this experiment, the force is kept constant at 3 kN (2 Bar) and the other two important parameters (current and weld time) were varied for two different thicknesses to study the growth of weld nuggets. The test was conducted for two thicknesses (1 mm and 2 mm) of mild steel. Table 1 shows the chemical composition properties of materials and Table 2 shows the weld schedules that were used for this test.

Table 1: Chemical properties of mild steel

Element	Maximum wt %
C	0.23
Mn	0.90
P	0.04
S	0.05

Table 2: Weld schedule

Samples Number	Thicknesses (mm)	Force (kN)	Current (kA)	Weld time (Cycle)
1-5	1 and 2	3	8	8
6-10	1 and 2	3	10	8
11-15	1 and 2	3	12	8
16-20	1 and 2	3	8	10
21-25	1 and 2	3	10	10
26-30	1 and 2	3	12	10
31-35	1 and 2	3	8	12
36-40	1 and 2	3	10	12
41-45	1 and 2	3	12	12

We have varied the parameters from lower range of weld schedules (force = 3 kN; current = 8 kA; time = 8 cycles) to higher range of weld schedules (force = 3 kN; current = 12 kA; time = 12 cycles) to analyse the nugget growth as well as the weld strength. It yields three by three matrixes with constant force. The sample size was maintained at the same size (25 mm x 200 mm) except thicknesses (Figure 1). The tensile-shear (Figure 2) test was carried out to determine the yield strength of spot welded samples and also analyse the strength of weld nuggets. The Ultimate Tensile Strength (UTS) was taken into consideration after which the breaking of weld occurred (Figure 2).

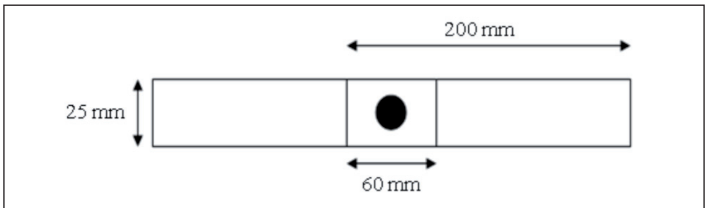

Figure 1: Test sample

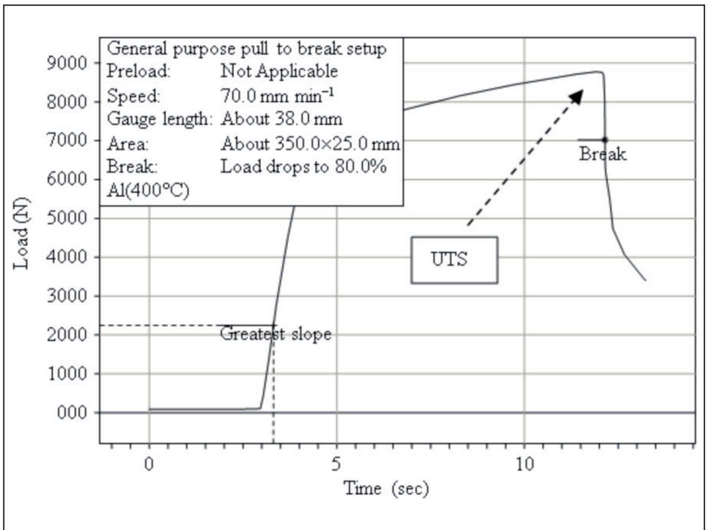

Figure 2: Tensile shear curve

The specimens are all welded using 50 KVA spot welding machine with an electrode tips of 5 mm (round) in diameter. The weld schedule was specifically increased by two parameters that of, firstly the current (8, 10 and 12 kA); secondly the time cycle (8, 10 and 12 cycles) while a constant force was maintained during the welding process takes place. As such a combination of 45 samples was developed with 5 samples in each weld schedule (Table 2). An average tensile strength value of the 5 samples was taken into account. Moreover the welded nuggets have also been analyzed for hardness distribution along the welded zone (heat affected zone, fusion zone) and also for the hardness of un-welded areas. The hardness was measured for 5 repetitions along the diameter of nuggets using Rockwell Hardness Tester using HRB scale. All the forty five samples were picked to undergo hardness test. The results are graphically shown in Figure 5.

3.0 RESULTS AND DISCUSSION

3.1 Tensile Shear Test

The entire weld schedule is divided into 3 groups; as, group 1, 2 and 3 to show the weld time increment (8, 10 and 12 cycle). Each group shows the weld current increments from 8 to 10 and 10-12 kA. Each testing uses 5 samples to obtain an average of tensile strength and hardness. As for the 1 mm-mild steel and referring to weld schedule 1 (Figure 3), the tensile strength increases from the 1st weld schedule to the 2nd weld schedule (4452kN to 5962kN) and then drops at the 3rd weld schedule (5962kN to 5678kN). This is because from the 1st weld schedule to the 2nd weld schedule, weld current increases from 8-10 kA. Therefore more heat is supplied at the weld zone which produces a stronger weld. However further increase in current (12 kA) causes expulsion which reduces the weld strength [1]. For the same 1 mm mild steel, comparing weld schedule 1, 4 and 7 where the welding current is maintained at 8 kA but the weld time increased from 8 cycles to 12 cycles, the weld strength initially shows an increase (4452kN to 6302kN) due to sufficient time given for the weld to develop.

However, at longer weld time (12 cycles), overheating causes the molten metal to expel from the weld zone therefore causing a reduction in weld strength (6302kN to 6127kN). The similar pattern was also found for the other set of welding schedules; i.e., 2, 5 and 8 (5962kN to 6903kN and to 6703kN) and also 3, 6 and 9 (5678kN to 6760kN and to 6200kN) [2].

Furthermore, to 1 mm specimens; the 2 mm mild steel and referring to weld schedule 1, the tensile strength increases from weld schedule 1 till weld schedule 3 (1663kN to 9600kN to11355kN). This is because of the increase in weld current from 8-12 kA which causes an increase in heat that is supplied to the weld zone. Comparing the weld pattern for 1 mm thickness and 2 mm thickness (Group 1 or 8 cycles weld time), weld schedule 3 shows a reduction in strength for 1 mm thickness due to expulsion. However with 2 mm thickness, expulsion was avoided because of the thickness (high resistance) of the mild steel path which was unable to cause overheating at the weld zone [1]. This is how the 1 and 2 mm mild steel showed difference in strength.

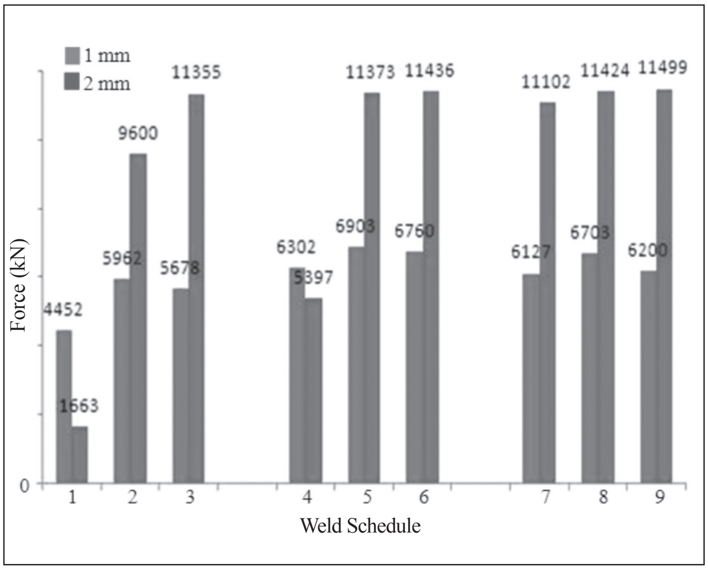

Figure 3: Tensile test result (1 and 2 mm)

In general an increase in weld strength was noticed for the 2 mm thickness compared to the 1 mm thickness except for welding schedule 1 and 4. These welding schedules were done with the lowest weld current (8 kA) and probably the current was not sufficient to create melting at the given welding time due to thickness. However at high current and weld time, the amount of heat supplied was sufficient to produce a sound weld. This is because the increase of thickness of welded sheets. Mathematically the heat generated by electrode is given by:

$$E = I^2_{ms} \cdot R \cdot T_s = I^2_{ms} \cdot \frac{\rho\ell}{A} \cdot T_s \qquad (1)$$

Where: I^2_{rms} = The true rms welding current; R = The sheet resistance; ρ = The sheet electrical resistivity; ℓ = The total sheet thickness; A = The spot area; T_s = The total welding cycle.

Since total sheet thickness is proportional to heat generation, strength achieved in 2 mm thickness sheets was higher than 1 mm thickness sheets mathematically. Similar observation was also discussed by Oikawa *et al.* (2007). By physical observation of the tensile-tested samples, three different weld failures were noticed. Firstly interfacial fracture (a), Secondly tear from edge of one side of metal sheet (b) and thirdly tear from both side of metal sheet (c). It was seen that the interfacial fracture occurred because of the insufficient supply of weld time and current, here. The tear from edge of one side of metal sheet occurred because of the gradual thermal distribution along the Heat Affected Zone (HAZ) and therefore the HAZ produces lower strength than the welded area. That's why the break occurred at the HAZ rather than the center of welded area. Lastly, tear from both side of metal sheet occurred because of the over-thermal gradient at the heat affected zone on which the tear off easily happens when pull out force is applied [8-10]. Figure 4 shows the different weld failures of test samples.

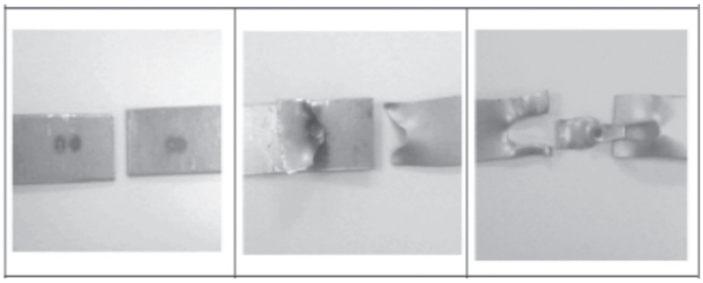

(1 mm Samples)

(a) (b) (c)

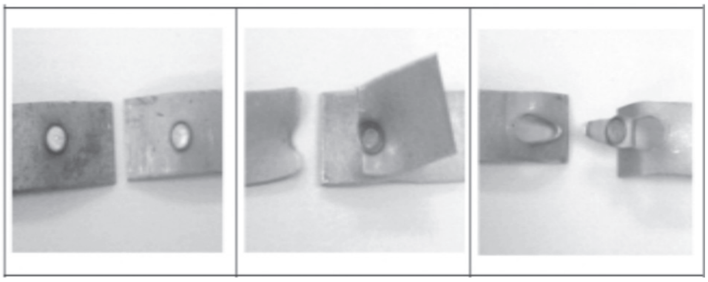

(2 mm Samples)

(a) (b) (c)

Figure 4: Tensile tested samples.
(a) Interfacial fracture (I = 8 kA; T = 8 cycle);
(b) tear from edge of one side of metal sheet (I = 10 kA; T = 10 cycle);
(c) tear from edge both side of metal sheet (I = 12 kA; T = 12 cycle)

3.2 Hardness Test

Hardness test was done using the Brinell-Rockwell Tester to study the hardness of weld obtained for both 1 mm and 2 mm mild steel. Hardness of welded area versus un-welded area yields a distinguishable difference on hardness values. The welded area has higher hardness compared to the un-welded. This is because of the heat treatment characteristics of mild steel. The hardness of mild steel can be increased by heat treatment. As such the welded areas are giving higher hardness values as compared to unwelded areas. However the increment of weld schedules with respect to hardness distribution along the welded areas, seemed not proportional. It fluctuated along the areas of weldment (Figure 5). This observation seemed true for both 1 and 2 mm thickness sheets.

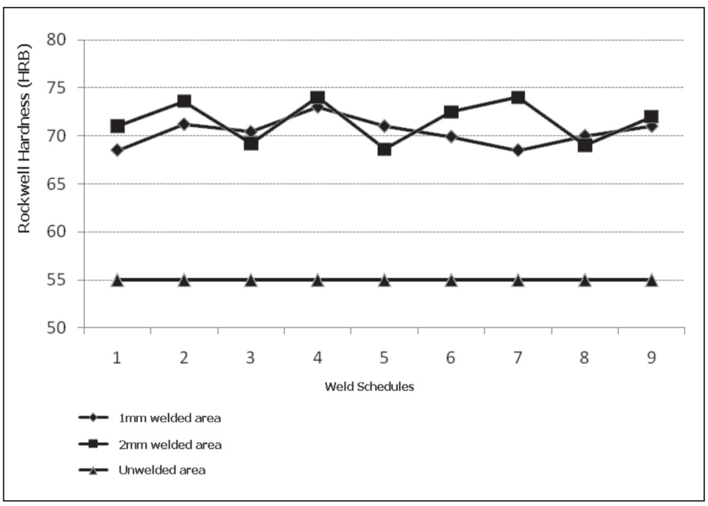

Figure 5: Rockwell hardness results (HRB values Vs group samples)

3.3 Micro Structures

The metallurgical studies have shown thorough details about the nugget formations and expansions. Macro structures of nuggets were observed by varying current and force but only some (current based) of it included here for simplicity. Finally it supports the tensile and hardness test results by showing increment in diameters (Table 3).

Table 3: Micro structures of weld nuggets

Base Metal (1 mm)	**Base Metal (2 mm)**
MS-1 mm (**8** kA, 10 cycles, 3 bars)	MS-2 mm (**8** kA, 10 cycles, 3 bars)
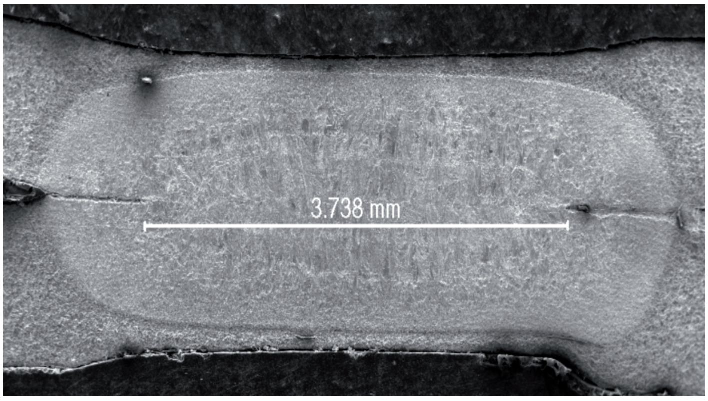	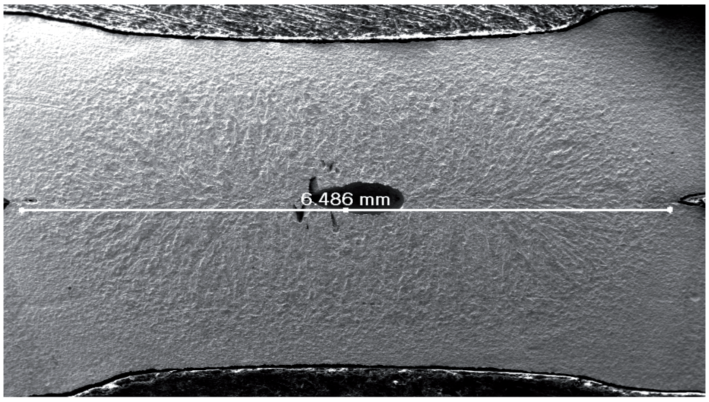
MS-1 mm (**10** kA, 10 cycles, 3 bars)	MS-2 mm (**10** kA, 10 cycles, 3 bars)
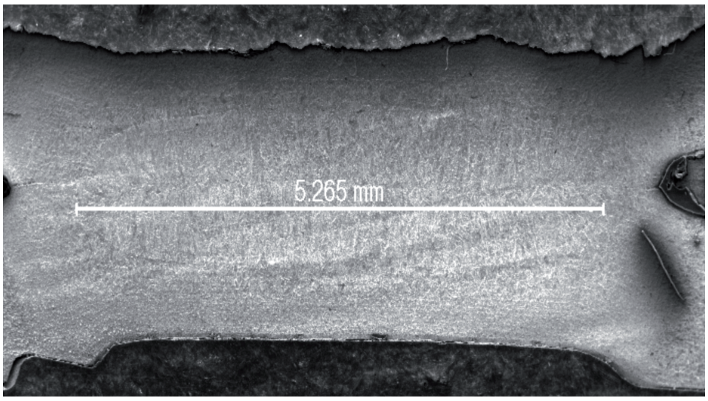	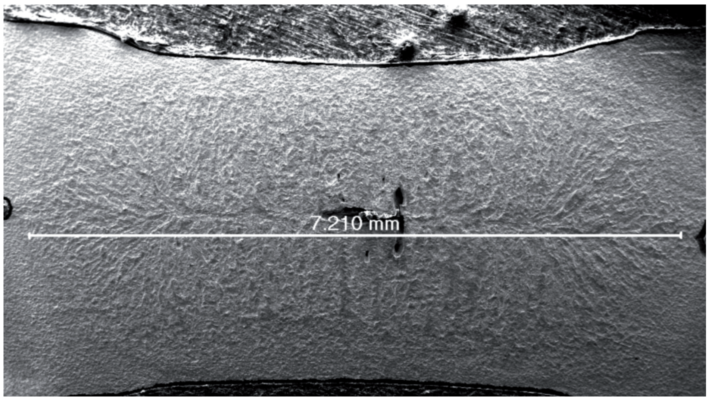
MS-1 mm (**12** kA, 10 cycles, 3 bars)	MS-2 mm (**12** kA, 10 cycles, 3 bars)
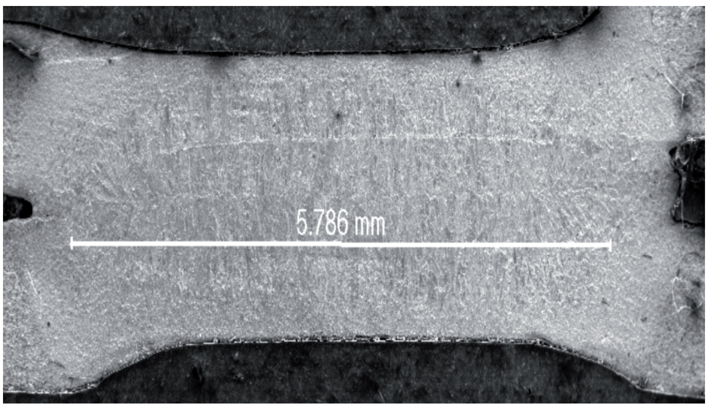	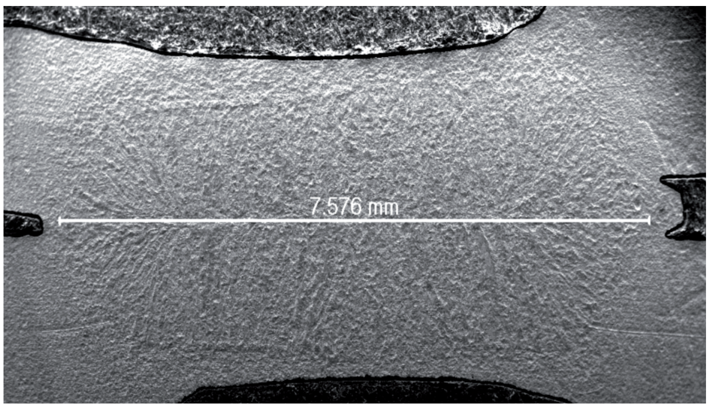

4.0 CONCLUSIONS

This experiment looks into the RSW characteristic of low carbon mild steel of 1 and 2 mm of thickness. It concludes that:

1. Increase in current and time resulted increment in tensile strength until expulsion limit occurred.

2. Increasing the thickness of base metal caused strong bounding between base metals and consequently increased tensile force is required to break the nuggets.

3. The diameter of nuggets was increased with increase in current and time which supports the tensile strength increment on tensile tests.

4. The hardness values of welded area were increased (from 55 to 72 HRB in average) due to the electrical and thermal conductivity of mild steel.

5. When the thickness of nuggets was reduced due to expulsion it also resulted in reduced tensile strength.

6. Macro structure of nuggets exhibits the coarser area (fusion zone), fine area (heat affected zone) and base metal clearly.

5.0 ACKNOWLEDGEMENTS

We would like to thank Ministry of Science, Technology and Innovation of Malaysia (MOSTI) for its financial support throughout the experimentations. ■

REFERENCES

[1] J.B. Shamsul and M.M. Hisyam, 2007, Study of Spot Welding of Austenitic Stainless Steel Type 304, Journal of Applied Sciences Research, Vol 3(11); 1494-1499.

[2] Dursun O¨ zyu¨rek , 2008 , An effect of weld current and weld atmosphere on the resistance spot weld ability of 304L austenitic stainless steel, Materials and Design 29 (2008) 597-603.

[3] Ranfeng Qiu, Shinobu Satonaka and Chihiro Iwamoto, 2009, Effect of interfacial reaction layer continuity on the tensile strength of spot welded joints between aluminum alloy and steels, Materials and Design 30 (2009) 3686-3689.

[4] D.Q. Sun, B. Lang, D.X. Sun and J.B. Li, 2007, Microstructures and mechanical properties of resistance spot welded magnesium alloy joints, Materials Science and Engineering A 460-461 (2007) 494-498.

[5] Kent P. von Maubeuge*, Henning Ehrenberg Naue,2000, Comparison of peel bond and shear tensile test methods for needlepunched geosynthetic clay liners, Geotextiles and Geomembranes 18 (2000) 203-214.

[6] E. Bayraktar , J. Moiron and D. Kaplan, 2006, Effect of welding conditions on the formability characteristics of thin sheet steels: Mechanical and metallurgical effects, Journal of Materials Processing Technology 175 (2006) 20-26.

[7] X. Kong, Q. Yang, B. Li, G. Rothwell, R. English a and X.J. Ren a, 2008, Numerical study of strengths of spot-welded joints of steel, Materials and Design 29 (2008) 1554-1561.

[8] P. Marashi , M. Pouranvari , S. Amirabdollahian, A. Abedi and M. Goodarzi, 2008, Microstructure and failure behavior of dissimilar resistance spot welds between low carbon galvanized and austenitic stainless steels, Materials Science and Engineering A 480 (2008) 175-180.

[9] C. Maa, D.L. Chena, S.D. Bhole, G. Boudreau, A. Lee and E. Biro, 2008, Microstructure and fracture characteristics of spot-welded DP600 steel, Materials Science and Engineering A 485 (2008) 334-346.

[10] Hatsuhiko Oikawa, Gen Murayama, Tatsuya Sakiyama, Yasuo Takahashi and Tadashi Ishikawa, 2007, Resistance Spot Weldability of High Strength Steel (HSS) Sheets for Automobiles. Nippon Steel Technical Report No. 95.

PROFILES

DR ARAVINTHAN ARUMUGAM is currently working as Assistant Professor at Nottingham University Malaysia Campus in Department of Mechanical, Materials and Manufacturing Engineering. He has obtained his PhD and BEng(Hons) in Mechanical Engineering from Nottingham Trent University UK. His research areas are mainly in the manufacturing processes and industrial automation. He holds a research grant from MOSTI from which this paper was produced. Dr. Aravinthan is also a Chartered Engineer with the Institution of Mechanical Engineers and a Graduate Engineer with the Board of Engineers Malaysia (BEM).

MR. NACHIMANI CHARDE SINGGARAN is currently pursuing a full time PhD under Dr Aravinthan Arumugam at Nottingham University Malaysia Campus. He was graduated with Bachelor of Engineering in Electronics System Design Engineering from Northumbria University UK and Master of Science in Electrical and Electronics Engineering from Southern Pacific University USA. He is a Member of IEEE and IEM Student Member (44779). Besides he has about 5 years teaching experience at Private Higher Educational Institutions in Malaysia.

NUMERICAL AND EXPERIMENTAL STUDY OF SHOCK/TURBULENT FLOW INTERACTION – A CODE VALIDATION TEST

(Date received:9.1.2011/Date approved: 19.8.2011)

Mohammad Ali Jinnah[1] and Kazuyoshi Takayama[2]
[1]*MCE Department, Islamic University of Technology, Board Bazar, Gazipur-1704*
[2]*Multidisciplinary Shock Wave Research Center, Tohoku University,*
2-1-1 katahira, Aoba-ku, Sendai 980-8577, Japan
E-mail: [1]jinnah@iut-dhaka.edu

ABSTRACT

A numerical code has been developed to solve the shock/turbulence interaction using grid adaptation technique. For the code validation test, shock wave propagations through nozzle are studied experimentally and numerically for the incident shock Mach number 1.60. The experimental photographs, taken by double exposure holographic interferometry, are used for the code validation test and a comparison is conducted between the experimental photographs and the numerical images. The shock wave propagation through a nozzle of small throat area is selected where laminar flow structures, transition phenomena, flow separation line as well asviscous boundary layer separation, wave propagation through the throat of the nozzle and shock wave reflection from converging area of the nozzle are observed numerically. The numerical results agree well with the experiment results. The numerical code is used to solve the two-dimensional Navier-Stokes equations with k-ε turbulence model for the solution of the shock wave propagation through the nozzle and this code later has been extended to develop a three-dimensional code. The three-dimensional code is used to solve the shock or turbulence interaction for a compressible fluid. A grid convergence study has been performed to validate the interaction results. The Navier-Stokes Simulation (NS) results for the shock wave interaction with turbulence are compared with the Navier-Stokes Simulation (NS) results with k-ε turbulence model and the comparison results are good enough to validate the present simulation works.

Keywords: *Navier-Stokes Equations, Shock or turbulence Interaction, Shock Wave, Turbulent Flow, Turbulence Model*

1.0 INTRODUCTION

The investigation on shock or turbulence interaction is an important feature due to its complexity to determine the characteristics of the turbulence by experimentally and numerically. Experimental realization of a homogeneous and isotropic turbulent flow interacting with a normal shock wave in the laboratory is a difficult task due to generation of compressible and isotropic turbulent flow and the generation of a normal shock wave interacting with flow. Experimentally and numerically many researchers got many results on shock or turbulence interaction. The outcomes of the interactions of shock wave with homogeneous and isotropic turbulence are the amplification of longitudinal velocity fluctuation, the amplification of turbulent kinetic energy level and substantial changes in length scales. The selection of homogeneous and isotropic turbulent field interactions is the easier phenomena than the other types of turbulent field like turbulent boundary layer interactions, turbulent wake-shock interaction. Turbulence amplification through shock wave interactions is a direct effect of the Rankine-Hugoniot relations. The study of the interaction of turbulence with a shock wave is of fundamental importance in engineering applications. For designing aero-mechanism system such as transport aircraft of supersonic and hypersonic speed, the shock wave and turbulence interaction effects are the important phenomena. The shock or turbulence interaction effects are generally seen in aero-mechanism system and in combustion process as well as high-speed rotor flows.

The study of the interaction of turbulence with a shock wave began in the early 1950s with the development of linear theories. Ribner [1-3] investigated how a shock wave is perturbed by an impinging single shear wave. The theory, later on called Ribner's theory, is, in fact, mostly based on the mode theory developed by Kovasznay [4] and extended to the shock problem by focusing mainly on the acoustic field generated by the interaction with the shock wave. Using his general theory of aerodynamic sound generation, Lighthill [5] estimated the acoustic energy scattered from the interaction of turbulence with a shock wave. Analytical studies of shock-turbulence interaction (Ribner [1]; Moore [6]; Kerrebrock [7]) were developed using a linearised description of the interaction of plane disturbances interacting with a shock wave.

These disturbances were represented as waves of vorticity, entropy, or sound (Kovasznay [4]) and these disturbances interacting with the shock wave generates the fluctuations downstream of the shock wave. Ribner [1] investigated the passage of a single vorticity wave through a plane shock and its modification, with simultaneous generation of a sound wave in a reference frame fixed on the shock wave.

This analysis was later extended to study turbulence amplification due to a shock wave (Ribner [2]), the flux of acoustic energy emanating from the downstream side of the shock (Ribner [3]), and the one-dimensional power spectra of various fluctuations downstream of the shock (Ribner [8]). Moore [6] analysed the flow field produced by oblique impingement of weak plane disturbances on a normal shock wave in a reference frame fixed on the mean upstream flow. Anyiwo *et al* [9] revisited the linear analysis to identify primary mechanisms of turbulence enhancement – amplification of the vorticity mode, generation of acoustic and entropy modes from the interaction, and turbulence 'pumping' by shock oscillations.

The shock or turbulence interaction considerably modifies the fluid field by vorticity and entropy production and transport. Experimental evidence from shock wave/boundary layer interaction indicates amplification in Reynolds stresses and turbulence intensities across the shock wave. The physics, however, of the phenomena associated with this amplification is not well understood. The first attempt to predict such turbulence amplification across the shock is attributed to Ribner [1]. His predictions were verified by experiments conducted by Sekundov [10] and Donsanjh *et al* [11]. Several analytical and numerical studies of this phenomenon show very similar turbulence enhancement.

Chu *et al* [12] indicated that there are three fluctuating modes, which are coupled and are responsible for the turbulence amplification. Acoustic (fluctuating pressure and irrotational velocity mode), turbulence (fluctuating vorticity mode) and entropy (fluctuating temperature mode) are the three fluctuating modes which are nonlinearly coupled and the Rankine-Hugoniot jump conditions across the shock indicate that when any one of the three fluctuation modes is transferred across a shock wave, it not only generates the other two fluctuation modes, but it may itself also be considerably amplified.

Many researcher conducted experiments on the interaction of turbulent boundary layers with an oblique shock wave. A general finding from the experiments is that Reynolds shear stress and turbulence intensities are amplified across the shock wave. The interaction of an oblique shock wave with a turbulent boundary layer involves several complex phenomena like, unsteady flow separation in the interaction region, oscillation of the shock wave in the longitudinal direction, streamline curvature, and inhomogeneity effects due to walls. Due to above complications, it has been difficult to determine through these experiments the effect of shock wave on turbulence.

Experiments on the interaction between the shock wave and grid-generated turbulence, were conducted by Debreve *et al* [13] and they measured velocity and temperature spectra upstream and downstream of the shock wave and concluded that turbulent fluctuations are amplified and Taylor micro scales increase during the interaction. Jacquin *et al* [14] investigated the interactions of a normal shock wave with grid-generated turbulence and a turbulent jet and they observed that turbulence amplification was not significant for the grid-generated turbulence and that the decay of turbulent kinetic energy was accelerated downstream of the shock wave.

Their experiments treated the interaction of a shock with quasi-incompressible turbulence where fluctuations in pressure and density are not significant. They have observed that the data obtained from grid-generated turbulence are not sufficient to characterise the turbulence properly. They have analysed the flow by means of laser Doppler velocimetry. The obtained supersonic flow is shocked by means of a second throat creating a pure normal shock wave or free turbulence interaction. On other hand, Debreve *et al* [13] obtain a quasihomogeneous turbulence by generating perturbations in the settling chamber of a supersonic wind tunnel at Mach 2.3.

They show that, after the expansion in the nozzle, the turbulent field becomes strongly non-isotropic and that the turbulence level is drastically decreased leading to experimental difficulties. Debieve *et al* [15] analysed the evolution of turbulence through a shock, and separated the effects of the specific turbulent sources from the effects of the mean motion-convection and production. Their prediction of the longitudinal velocity fluctuation was in good agreement with the experimental results. An experimental work was performed on the interaction of weak shocks (M_s = 1.007, 1.03 and 1.1) with a random medium of density in homogeneity by Hesselink *et al* [16].

They observed that the pressure histories of the distorted shock waves were both peaked and rounded and explained these features in terms of the focusing or defocusing of the shock front due to in homogeneity of the medium. The Richtmyer- Meshkov instability (Richtmyer [17] and Meshkov [18]) provides an important example of the interaction of a shock wave and a material interface. This instability is observed when a shock wave passes normally through a perturbed interface between two fluids of different densities. Experiments of such an instability show that a single shock wave will cause the perturbation's amplitude to grow linearly with time.

However, interaction of the perturbation with a second shock stimulates the growth of the mixing zone between the gases. One interpretation of the experiments is that mixing is enhanced, that is the mixing zone between the two fluids grows, by the interaction of the shock wave with the turbulent or random flow field left behind the first shock wave.

In the present validation test of 2D code for the solution of Navier-Stokes equations, shock wave propagations through nozzle are studied experimentally and numerically. The shock wave propagation through a nozzle of small throat area is selected where laminar flow structures, transition phenomena, flow separation line as well as viscous boundary layer separation, wave propagation through the throat of the nozzle and shock wave reflection from converging area of the nozzle are observed numerically.

A good numerical simulation for nozzle flow depends on the throat area and the converging or diverging angle of the nozzle and the strength of the shock wave propagate through the throat of the nozzle. After the validation test of the 2D code, the extended code for the solution of three-dimensional Navier-Stokes equations with *k-ε* turbulence model is developed to solve almost all types of shock or turbulence interaction problems. For the better solution of the flow field, the improved three-dimensional grid adaptation technique is applied in these computations.

2.0 NUMERICAL METHOD

The three-dimensional unsteady, compressible, Reynolds-averaged Navier-stokes equations with *k-ε* turbulence model are solved by shock capturing method. Without external forces and heat sources, the conservative form of non-dimensionalised governing equation in three-dimensional Cartesian coordinate system is:

$$\frac{(\partial Q)}{\partial t} + \frac{\partial (F - Fv)}{\partial x} + \frac{\partial (G - Gv)}{\partial y} + \frac{\partial (H - Hv)}{\partial z} = S(Q) \quad (1)$$

where, $Q = [\rho, \rho u, \rho v, \rho w, e, \rho k, \rho\varepsilon]$,

$F = [\rho u, \rho u^2, \rho uv, \rho uw, u\,(e + p), \rho uk, \rho u\varepsilon]$,

$$G = [\rho v, \rho uv, \rho v^2, \rho vw, v\,(e + p), \rho vk, \rho v\varepsilon],$$
$$H = [\rho w, \rho uw, \rho vw, \rho w^2, w(e + p), \rho wk, \rho w\varepsilon]$$

and,
$$Fv = [0, \tau_{xx}, \tau_{xy}, \tau_{xz}, u\tau_{xx} + v\tau_{xy} + w\tau_{xz} - q_x, k_x, \varepsilon_x],$$
$$Gv = [0, \tau_{xy}, \tau_{yy}, \tau_{yz}, u\tau_{xy} + v\tau_{yy} + w\tau_{yz} - q_y, k_y, \varepsilon_y],$$
$$Hv = [0, \tau_{xz}, \tau_{yz}, \tau_{zz}, u\tau_{xz} + v\tau_{yz} + w\tau_{zz} - q_z, k_z, \varepsilon_z]$$

Here Q is the vector of conservative variables which contains mass, momentum and energy. All variables are calculated in per unit volume. ρ is taken as the mass per unit volume. Three momentum terms in three-dimensional Cartesian coordinates system are ρu, ρv and ρw per unit volume. Total energy, e, turbulent kinetic energy, ρk and turbulent dissipative energy, $\rho\varepsilon$ are the energy terms per unit volume in these computations. F, G and H are the three inviscid flux vectors in X-, Y-, and Z-axis respectively. Similarly Fv, Gv and Hv are the three viscous flux vectors in X-, Y-, and Z-axis respectively. Each flux vectors contain mass flux, momentum flux and energy flux. ρu is the mass flux and ρu^2, ρuv, ρuw are the momentum flux and $u\,(e + p)$, ρuk, $\rho u\varepsilon$ are the energy flux in the X-axis. Similarly ρv is the mass flux and ρuv, ρv^2, ρvw are the momentum flux and $v(e + p)$, ρvk, $\rho v\varepsilon$ are the energy flux in the Y-axis and ρw is the mass flux and ρwu, ρvw, ρw^2 are the momentum flux and $w\,(e + p)$, ρwk, $\rho w\varepsilon$ are the energy flux in the Z-axis. Also ρ is the fluid density and u, v and w are velocity components in each direction of Cartesian coordinates. While e is the total energy per unit volume, pressure p can be expressed by the following state equation for ideal gas

$$p = (\gamma - 1)[e - \frac{1}{2}\rho(u^2 + v^2 + w^2)] \tag{2}$$

where γ is the ratio of specific heats. From the relationship between stress and strain and assumption of stokes, non-dimensional stress components are as follows:

$$\tau_{xx} = \frac{\mu}{\mathrm{Re}}\frac{2}{3}\left(2.\frac{\partial u}{\partial x} - \frac{\partial v}{\partial y} - \frac{\partial w}{\partial z}\right), \tau_{yy} = \frac{\mu}{\mathrm{Re}}\frac{2}{3}\left(2.\frac{\partial v}{\partial y} - \frac{\partial w}{\partial z} - \frac{\partial u}{\partial x}\right), \tau_{zz} = \frac{\mu}{\mathrm{Re}}\frac{2}{3}\left(2.\frac{\partial w}{\partial z} - \frac{\partial u}{\partial x} - \frac{\partial y}{\partial y}\right).$$

$$\tau_{xx} = \frac{\mu}{\mathrm{Re}}\left(\frac{\partial v}{\partial x} - \frac{\partial u}{\partial y}\right), \tau_{yz} = \frac{\mu}{\mathrm{Re}}\left(\frac{\partial w}{\partial y} - \frac{\partial v}{\partial z}\right), \tau_{xz} = \frac{\mu}{\mathrm{Re}}\left(\frac{\partial u}{\partial z} + \frac{\partial w}{\partial x}\right).$$

$$k_x = \frac{1}{\mathrm{Re}}\left(\mu_1 + \frac{\mu_t}{\sigma_k}\right)\frac{\partial k}{\partial x}, \quad \varepsilon_x = \frac{1}{\mathrm{Re}}\left(\mu_1 + \frac{\mu_t}{\sigma_k}\right)\frac{\partial \varepsilon}{\partial x}$$

$$k_y = \frac{1}{\mathrm{Re}}\left(\mu_1 + \frac{\mu_t}{\sigma_k}\right)\frac{\partial k}{\partial y}, \quad \varepsilon_y = \frac{1}{\mathrm{Re}}\left(\mu_1 + \frac{\mu_t}{\sigma_k}\right)\frac{\partial \varepsilon}{\partial y}$$

$$k_z = \frac{1}{\mathrm{Re}}\left(\mu_1 + \frac{\mu_t}{\sigma_k}\right)\frac{\partial k}{\partial z}, \quad \varepsilon_z = \frac{1}{\mathrm{Re}}\left(\mu_1 + \frac{\mu_t}{\sigma_k}\right)\frac{\partial \varepsilon}{\partial z}$$

The expression of laminar viscosity is $\mu_l/\mu_o = c_v\,(T/T_o)$ 1.5 where μ_o, is the laminar viscosity at the ambient temperature (T_o) and the coefficient, c_v depends on the temperature and the ambient gas. The total viscosity $\mu = \mu_l + \mu_t$ where μ_t is the turbulent eddy viscosity and the expression of turbulent eddy viscosity,

$$\mu_t = c_\mu\,\rho\,\frac{k^2}{\varepsilon} \tag{3}$$

The element of heat flux vectors are expressed by Fourier law of heat conduction as

$$q_x = \frac{\mathrm{kc}}{\mathrm{Re}}\frac{\partial T}{cx}, \quad q_y = \frac{\mathrm{kc}}{\mathrm{Re}}\frac{\partial \mathrm{T}}{cy}, \quad q_z = \frac{\mathrm{kc}}{\mathrm{Re}}\frac{\partial T}{cz}$$

where T, is the temperature, k_c is the thermal conductivity and it expresses by $k_c = k_l + k_t$. The expression of the thermal conductivity of the laminar part is $k_l/k_o = ck\,(T/T_o)$ 1.5 where k_o is the thermal conductivity at the ambient temperature and the value of the coefficient, c_k depends on the temperature and the ambient gas. The expression of the thermal conductivity of the turbulent part is $k_t = c_{tk}\,\frac{\mu_t}{\mathrm{Pr}}$, where the value of the coefficient, c_{tk} depends on the temperature and the ambient gas and Pr is the Prandtl number based on characteristic values. The Reynolds number of the flow is defined by Re = $(\rho_c u_c l_c/\mu_o)$ where ρ_c, u_c, l_c and μ_o are respectively a characteristic density, a characteristic velocity, a characteristic length and the viscosity of the fluid.

The source term $S\,(Q)$ of the k-ε turbulence model is written by

$$S(Q) = [0, 0, 0, 0, P_k - \rho\varepsilon - D_k, (c_{\varepsilon 1}.P_k - c_{\varepsilon 2}\,.\,\rho\varepsilon)\,\frac{\varepsilon}{k}] \tag{4}$$

where the production term P_k, which is the three-dimensional formulation, developed from the two-dimensional formulation of Kunz et al. (1992), is given in Cartesian coordinates as

$$P_k = \{2\,\mu_t\frac{\partial u}{\partial x} - \frac{2}{3}[\rho k + \mu_t\left(\frac{\partial u}{\partial x} + \frac{\partial v}{\partial y} + \frac{\partial w}{\partial z}\right)]\}\frac{\partial u}{\partial x} + \{2\,\mu_t\frac{\partial v}{\partial y} - \frac{2}{3}[\rho k + \mu_t(\frac{\partial u}{\partial x} + \frac{\partial v}{\partial y} + \frac{\partial w}{\partial z})]\}$$
$$\frac{\partial v}{\partial y} + \{2\,\mu_t\frac{\partial w}{\partial z} - \frac{2}{3}[\rho k + \mu_t\left(\frac{\partial u}{\partial x} + \frac{\partial v}{\partial y} + \frac{\partial w}{\partial z}\right)]\} + \mu_t\left(\frac{\partial u}{\partial y} + \frac{\partial v}{\partial x}\right)^2 + \mu_t\left(\frac{\partial w}{\partial y} + \frac{\partial y}{\partial z}\right)^2 \tag{5}$$

and the destruction term D_k is given as $D_k = \frac{2\rho}{\gamma T}\,\mathrm{k}\varepsilon$

The mass average turbulent kinetic energy and homogeneous component of turbulent kinetic energy dissipation rate are defined by as $k = \frac{1}{2}c_t^2\,(u^2 + v^2 + w^2)$ and $\varepsilon\;c_m\,k^2\,\frac{\mathrm{Re}}{100}$ (6)

The various constants in the k-ε turbulence model are listed as follows:

$$c_\mu = 0.09, c_t = 0.03, c_m = 0.09, c_{\varepsilon 1} = 1.45, c_{\varepsilon 2} = 1.92, \sigma_k = 1.00, \sigma_\varepsilon = 1.30 \tag{7}$$

3.0 NUMERICAL DISCRETISATION AND GRID ADAPTATION

The governing equations described above for compressible viscous flow are discretised by the finite volume method. A second order, upwind Godunov scheme of Flux vector splitting method is used to discretise the inviscid flux terms and MUSCL-Hancock scheme is used for interpolation of variables. Central differencing scheme is used in discretising the viscous flux terms. HLL Reimann solver is used for shock capturing in the flow. Two equations for k-ε turbulence model are used to determine the dissipation of turbulent kinetic energy and ε the rate of dissipation. The k and ε equations, each contains nonlinear production and destruction source terms, which can be very large near the solid boundaries. According to linear stability theory, such terms can also severely reduce convergence rates if a purely explicit scheme is used to discretise the equations. The above numerical discretisation and grid adaptation technique has been used by T. Kuribayashi *et al* [19] for numerical simulation of their experimental works.

Three dimensional hexahedral cells with adaptive grids are used for these computations. In this mesh, the cell-edge data structures are arranged in such a way that each cell contains six faces which are sequence in one to six and each face indicates two neighboring cells that are left cell and right cell providing all faces of a cell are arranged in a particular way by positions and coordinates in the mesh. The sequential six faces in Figure 1(i) are *abod, adhe, abfe, efgh, bogf, dogh*.

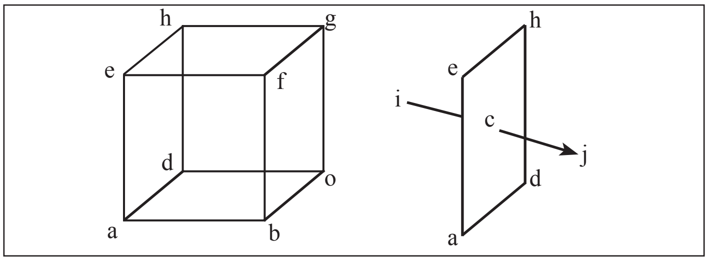

(i) (ii)

Figure 1: (i) Three-dimensional cell with six faces; (ii) Each face addresses the center of two neighboring cells, i and j

The grid adaptation is one of the improved and computational time saving techniques, which is used in these computations. The grid adaptation is performed by two procedures, one is refinement procedure and another is coarsening procedure. The refinement and coarsening operations are handled separately in computation. The criterion used for grid adaptation is based on the truncation error (ЄT) of the Taylor series expansion of density. The truncation error indicator ЄT is defined for every face of a cell and given by the ratio of the second-order derivative term to the first order one of the Taylor series of density so that

$$\epsilon_T = \max\left[\frac{|(\nabla\rho)_{lc} - (\nabla\rho)_i|}{(a_f\rho_c)/dl + |\nabla\rho|_i}, \frac{|(\nabla\rho)_{lc} - (\nabla\rho)_j|}{(a_f\rho_c)/dl + |\nabla\rho|_j}\right] \qquad (8)$$

where *c* represent in Figure 1 (ii) the location of any face of a cell and *i* and *j* represent left cell and right cell of that face, *dl* is the center distance between cell *i* and *j*, $(\nabla\rho)_i$ and $(\nabla\rho)_j$ are the density gradient for cell *i* and *j*, $(\nabla\rho)lc = (\rho i - \rho j)/dl$, ρ_c is the density at the interface of right cell and left cell and α_f is the constant which is initially designed to prevent a zero denominator. In these computations, the value of αf is used 0.02 and it is problem-independent parameter. The refinement and coarsening operation for any cell depends on ϵ_T value and this ϵ_T value is determined for each face of a cell. The criterion for adaptation for any cell is

Refinement = maximum ϵ_T of six faces of a cell > ε_r

Coarsening = maximum ϵ_T of six faces of a cell < ε_c

where ε_r and ε_c are the threshold values for refinement and coarsening. In these computations, the values of ε_r are used 0.16~0.48 and the values of ε_c are used 0.12~0.44 and the higher values are used for higher shock Mach number. The level of refinement, used in all types of computation, is 2 or 3, depending on the number of cell per unit volume. The original 5 x 5 x 5 (mm) cell size will be 1.25 x 1.25 x 1.25 (mm) if refinement level is 2 and 0.625 x 0.625 x 0.625 (mm) if refinement level is 3.

In refinement procedure, the cells are selected for refinement in which every cell is divided into eight new sub cells and these new sub cells are arranged in a particular sequence so that these sub cells are used suitably in the data-structure. In threedimensional adaptation, the volume of new sub cells is 1/8 of primary cell where in two dimensional, this fraction is 1/4. To avoid unlimited cells refinement around shock waves, either the maximum level of refinement or the minimum cell volume or both are prescribed. When either the level or the volume of cell reaches the given limit, further refinement is prohibited. In the refinement procedure, it is required that no two neighboring cells differ by more than one refinement level. This one level-difference rule has accepted by many authors because it simplifies adaptation procedure and prevents pathologically large volume ratios under certain circumstances. However, in unsteady calculations, the rule may be mismatch moving refined regions, say shock wave regions. To overcome this problem, pre-refinement is introduced. Once a cell cannot be refined due to the level difference between itself and one or a few neighboring cells, the neighboring cells are refined no matter what values of their refinement and coarsening are. In the coarsening procedure, the eight sub cells, which are generated from the primary cell, are restored into primary cell. The cell adaptive techniques are shown in Figures 2 (i) and (ii). The above three-dimensional adaptation strategy is based on an in-house 2-D solution adaptive code developed by Sun and Takayama [20].

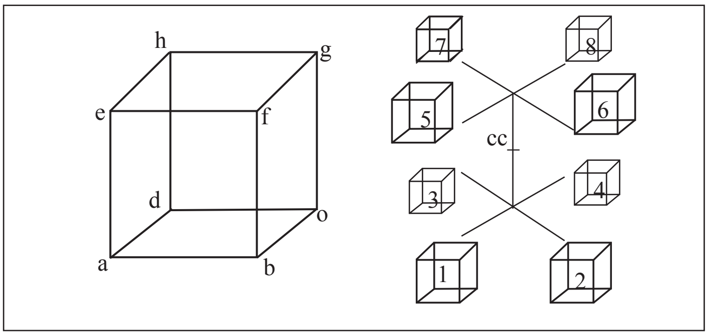

(i) (ii)

Figure 2: (i) Primary cell before adaptation where the center of the cell, cc is shown; (ii) Sequence of the eight cells after refinement of the primary cell as shown in Figure 2 (i)

4.0 TWO-DIMENSIONAL NUMERICAL VALIDATIONS

The experimental photographs, taken by double exposure holographic interferometry, are used for the code validation test and a comparison is conducted between experimental photographs and numerical images. The optical setup, present in the ISWRC laboratory, was used for the photographs and similar optical setup was also used by Sasoh *et. al.* [21] and other researchers in this laboratory. Many researchers conducted their code validation works on Navier-Stokes equations by using the flow over a flat plate. Some researchers used high-speed fluid flow around a cubic body to determine the velocity at different points on the axis of the cubic body and they attempted to simulate the viscous effect after determining the velocity along the axis numerically and experimentally.

In the present validation works, a visualisation technique is applied for the visualisation of the nozzle flow. For the purpose of code validation test, the shock wave propagation through a nozzle of small throat area is selected where laminar flow structures, transition phenomena, flow separation line as well as viscous boundary layer separation, wave propagation through the throat of the nozzle and shock wave reflection from converging area of the nozzle are observed numerically. The numerical code is used to solve the two-dimensional Navier-Stokes equations for the solution of the shock wave propagation through the nozzle and this code later has been extended to develop a three-dimensional code. The diameter of the throat of the nozzle is 2 mm and the details of the dimensions of the nozzle are shown in Figure 3 (i). The initial total number of cell is 10240 and the level of refinement is 3. All solid walls of the nozzle are taken as viscous solid wall boundary.

The upstream of incident shock wave is set as an inflow boundary condition, the properties and velocities of which are calculated from Rankine-Hugoniot conditions with incident shock Mach number. Shock wave propagations through nozzle are studied experimentally and numerically for the incident shock Mach number 1.60. The numerical results, shown in Figures 3 and 7 are compared with the experimental results, shown in Figures 4, 6 and 8. Discussions on agreement/disagreement between experimental and numerical results are described below:

(a) An agreement is observed in the laminar part of this flow field, which is shown in Figures 3 to 8.

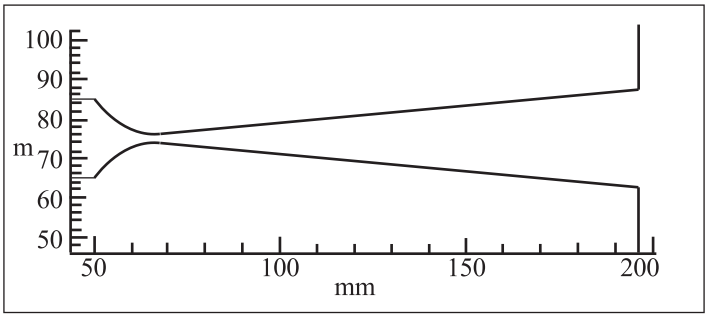

(i)

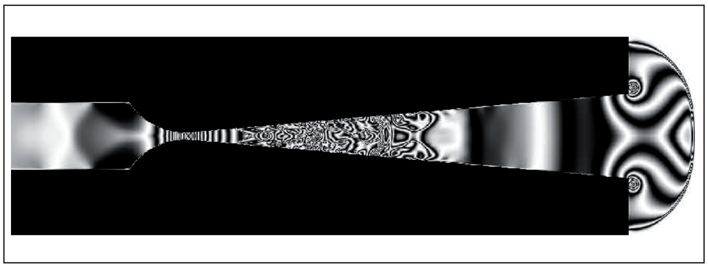

(ii)

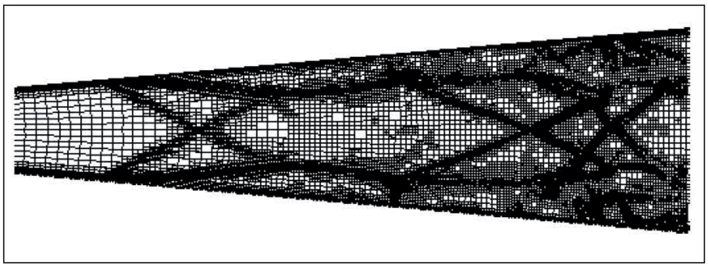

(iii)

Figure 3: (i) Physical dimensions of the nozzle used in both experimental works; Numerical results (ii) Numerical density fringes at the time instant 28 millisecond; (iii) Corresponding adaptive grids in which point of separation, slipstream and boundary layer separation line are visible clearly

(b) At the moment of flow separation, the point of separation and the separation line, shown in the numerical results in Figures 3, 5 and 7, have some agreements with the experimental results in Figures 4, 6 and 8. It is observed that the flow separation is clearly appeared in Figure 3 (iii) and Figure 5 (ii) where high-level refinement is observed along the separation line.

(c) Wave propagation through the throat of the nozzle, shown in experimental results, has the good agreement with numerical results.

(d) Boundary layer in different location of the flow field appears both in the experimental and numerical results and a good agreement is observed in both results. In gird adaptation, it is observed that the boundary layer separation line is clearly appeared in Figure 3 (iii) and Figure 5 (ii) where high-level refinement is observed along the boundary layer separation line.

(e) After the flow separation, an unsteady flow field appears and the flow transition period begins. In the transition period, some disagreement is observed between experimental results and numerical results. It may happen due to flow separation.

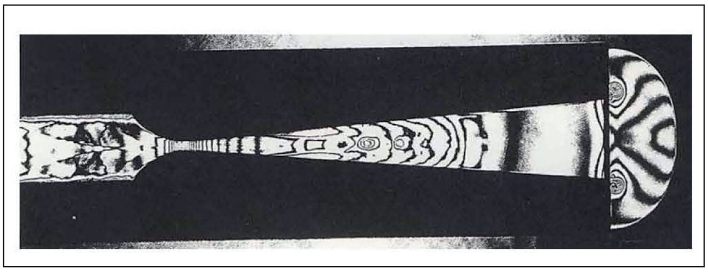

Figure 4: Experimental photo, taken by double exposure holographic interferometry; a shock wave propagating through nozzle at the same time instant 28 millisecond for viscous flow where the model of the nozzle is as Figure 3

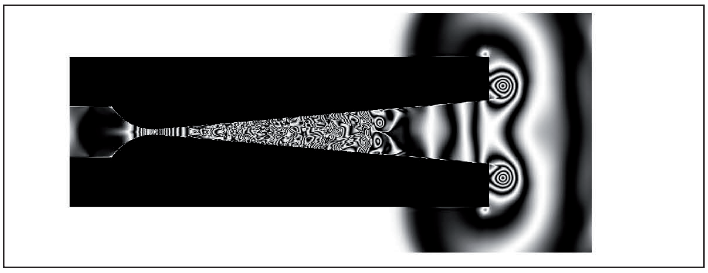

(i)

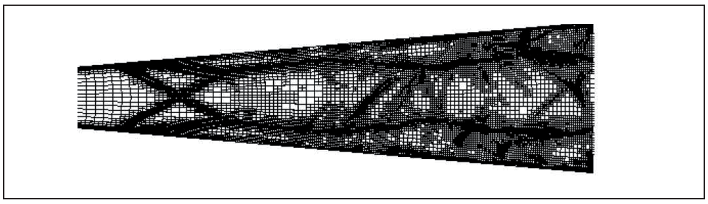

(ii)

Figure 5: Numerical results (i) Numerical density fringes at the time instant 51 millisecond; (ii) Corresponding adaptive grids in which point of separation, slipstream and boundary layer separation line are visible clearly

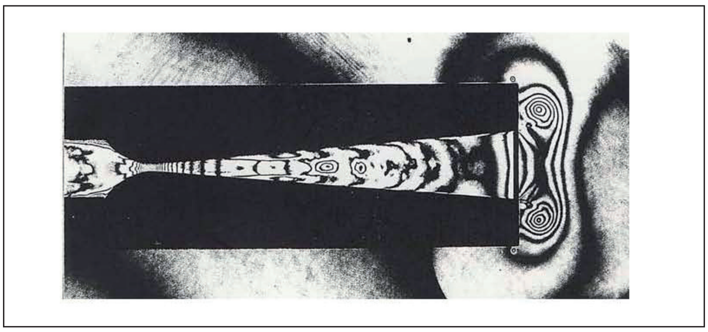

Figure 6: Experimental photo, taken by double exposure holographic interferometry; a shock wave propagating through nozzle at the same time instant 51 millisecond for viscous flow where the model of the nozzle is as Figure 3

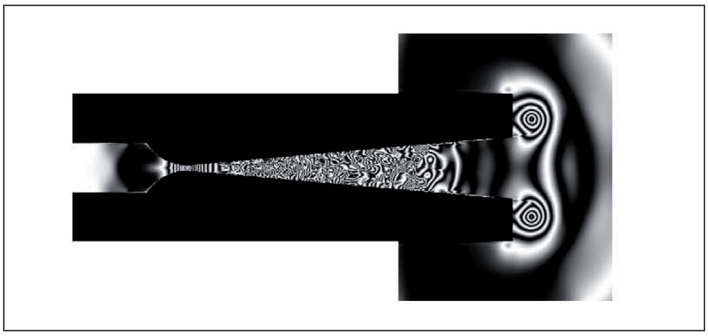

Figure 7: Numerical result: Numerical density fringes at the time instant 72 millisecond

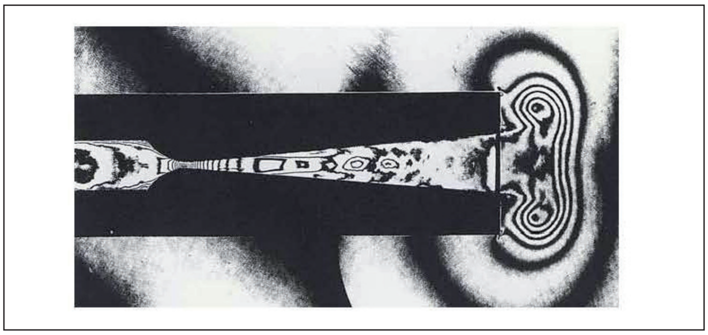

Figure 8: Experimental photo, taken by double exposure holographic interferometry; a shock wave propagating through nozzle at the same time instant 72 millisecond for viscous flow where the model of the nozzle is as Figure 3

5.0 THREE-DIMENSIONAL NUMERICAL VALIDATIONS

5.1 Problem specifications

For the purpose of three-dimensional numerical code validations, the three-dimensional mesh with turbulence-generating grids is used, which is shown in Figures 9 (i), (ii). The physical size of each cell before adaptation is 5 x 5 x 5 (mm) and the initial number of cell is 1985. The adaptive grids and the selected turbulent region are shown in Figure 10, which are the two-dimensional sectional view of ZX-plane. The distance between the turbulence-generating grid and the end wall is 65 mm and in this distance, a turbulent region is selected so that there have no boundary effects in the turbulent region. The longitudinal distances (*X/m*) of any point on the centerline of the turbulent region are determined from turbulence-generating gird where m is the maximum dimensional length of a grid in the grid system. The distance, X = 0.0 mm at the position of turbulencegenerating grids. The value *X/m* = 3.776 is the starting point of the centerline of turbulent region and the value *X/m* = 11.376 is the ending point of the centerline of turbulent region. All turbulence parameters are measured before and after the shock or turbulence interaction in the selected turbulent region. In these computations, the threshold values for refinement are used 0.16~0.20 and the threshold values for coarsening are used 0.12~0.16 and the level of refinement is 2. Based on characteristic values, Reynolds number is 21546 and Prandtl number is 0.722.

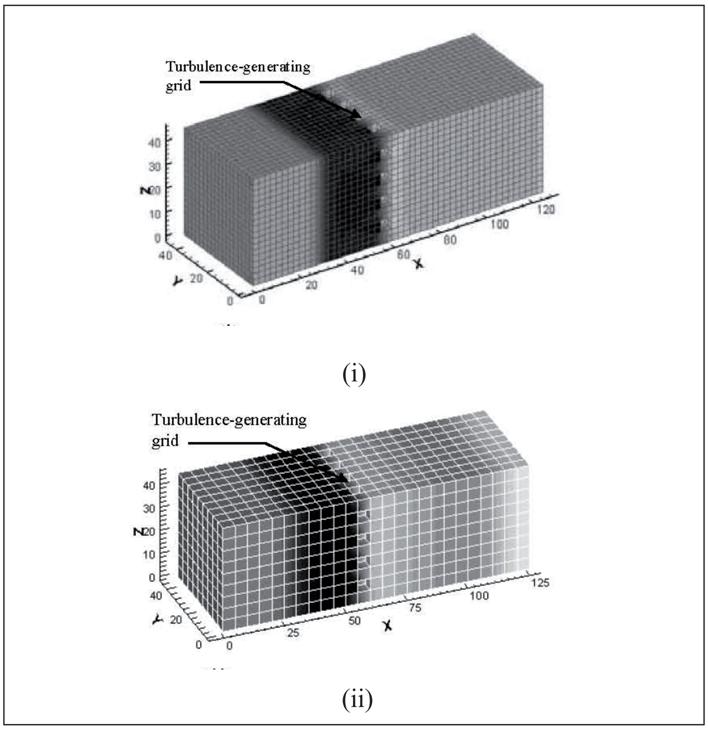

***Figure 9:** Three dimensional mesh and the position of the turbulence-generating grid plate are shown where different grid sizes are (i) $2 \times 2 \times 2$ grids/cm^3; (ii) $4 \times 4 \times 4$ grids/cm^3*

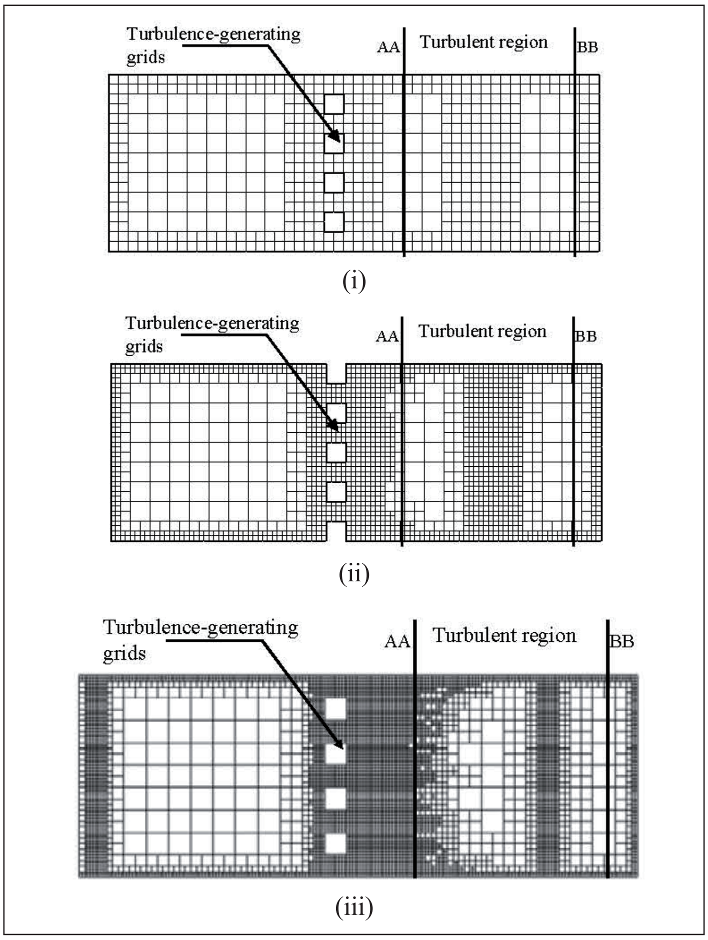

Figure 10: Two-dimensional cuts of the three-dimensional adaptive grids: (i) Level one; (ii) Level two; (iii) Level three

5.2 Grid convergence study

5.2.1 Using different level of refined grids

The study of the grid convergence on the present computational results has been carried out for different levels of grid refinement and for different grid sizes. The results, obtained for incident shock Mach number 1.50 are used for the study of the grid convergence. The refinement level one is used to solve the flow field with coarse grid and the refinement level three is used to solve the flow field with very refined grid. The results, obtained for level one, level two and level three refined grids, are compared with each other to observe the accuracy level of the computational results and such comparisons are used to determine the convergence behavior of the present simulation results. The two-dimensional sectional views of adaptive grids of level one, level two and level three refinements are shown in Figures10 (i), (ii) and (iii).

The grid size for refinement level one is 2.5 x 2.5 x 2.5 (mm), the grid size for refinement level two is 1.25 x 1.25 x 1.25 (mm) and the grid size for refinement level three is 0.625 x 0.625 x 0.625 (mm). The RMS (Root Mean Square) value of longitudinal velocity fluctuations or the longitudinal turbulence intensity, <u>/U are determined along the centerline of the turbulent region for the different levels of refined grids which is shown in Figure 11.

It is observed that the longitudinal turbulence intensity profile, obtained from the refinement level one, has some deviations with the profiles for higher refinement level and the longitudinal turbulence intensity profile for the refinement level two has the good agreement with the longitudinal turbulence intensity profile for the refinement level three and some disagreements are observed at the position near the turbulence grids. Similarly the lateral velocity fluctuations, v′/U and w′/U are determined along the centerline of the turbulent region for the different levels of refined grids and it is observed that there have the good agreements between the lateral velocity fluctuations profiles, obtained for higher level of refined grids. Figure 12 shows the average pressure variations across the reflected shock wave for the different levels of refined grids. It is observed that there have the good agreements between the average pressure profiles across the shock wave, obtained for higher level of refined grids.

5.2.2 Using different grid sizes

The utilities of the grid refinement in grid convergence study are sometimes difficult if there have the more deviations between the results obtained by two successive levels of the grid refinement. In that case different sizes of the grid are suitable to use for grid convergence study. Different grid sizes are 2 x 2 x 2 grid and 4 x 4 x 4 grid per cubic centimeter. For the size of 2 x 2 x 2 grid, the initial number of grid in the computational domain is 1985 and the computational domain is shown in Figure 9 (i). Similarly for the size of 4 x 4 x 4 grid, the initial number of grid in the computational domain is 15880 and the computational domain is shown in Figure 9 (ii). So, it is observed that different turbulent parameters in the turbulent region are determined for different number and size of the grids contain in the turbulent region.

The lateral planes intersect the centerline of the turbulent region, are used to determine different turbulent parameters. Each lateral plane contains several grids and the number of grid depends on the number of grid per unit volume in the turbulent region. For 4 x 4 x 4 grid, the number of grid in the lateral plane is approximately four times more than for 2 x 2 x 2 grid.

The computational results for different grid sizes are compared and performed the independence test of grid size in the present simulation results. All the results, obtained before and after the shock/turbulence interaction, are used to determine the independence test of grid size. The longitudinal turbulence intensity, *<u>/U* are determined along the centerline of the turbulent region for different grid sizes of 2 x 2 x 2 grid and 4 x 4 x 4 grid and the comparison between the characteristic profiles of the longitudinal turbulence intensity for different grid sizes are shown in Figure 13. It is observed in Figure 13 that the characteristic profiles for different grid sizes are simulated each other and the result indicates the independency on grid size in the present computations. Similarly the lateral velocity fluctuations, *v′/U* and *w′/U* are determined along the centerline of the turbulent region for different grid sizes of 2 x 2 x 2 grid and 4 x 4 x 4 grid and it is observed that the characteristic profiles of lateral velocity fluctuations for different grid sizes are simulated each other and the simulation results are independent on the grid size.

The normalised average pressure variations are determined across the reflected shock wave for different grid sizes of 2 x 2 x 2 grid and 4 x 4 x 4 grid and the comparison between the average pressure profiles for different grid sizes are shown in Figure 14. It is observed in Figure 14 that the average pressure profiles across the shock wave for different grid sizes are simulated each other and this result also indicates the independency on grid size in the present computations.

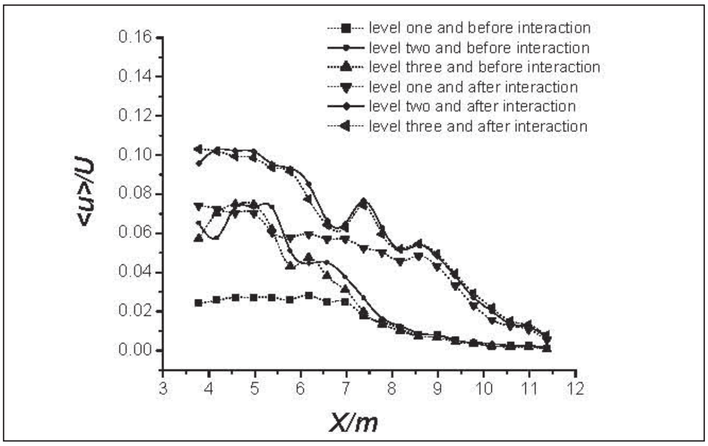

Figure 11: Longitudinal turbulence intensity (<u>/U) before and after the shock/turbulence interaction along the centerline of the turbulent region for different grid refinement levels

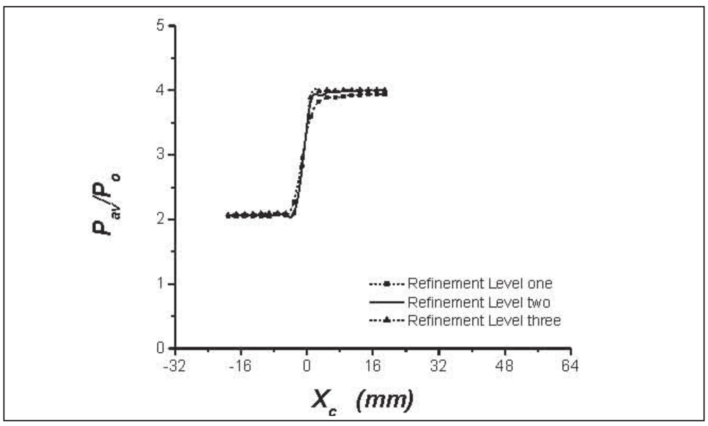

Figure 12: Average pressure (Pav/Po) variations across the reflected shock wave for different grid refinement levels, where the origin, Xc=0.0 corresponds to the shock location and X/m =7.6

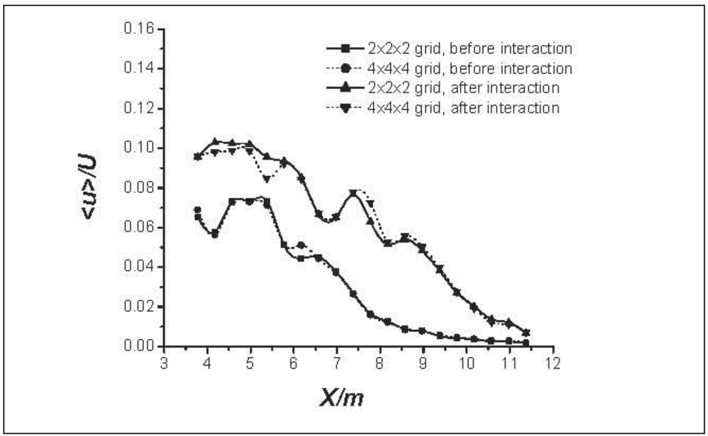

Figure 13: Longitudinal turbulence intensity (<u>/U) before and after the shock/turbulence interaction along the centerline of the turbulent region for different grid sizes

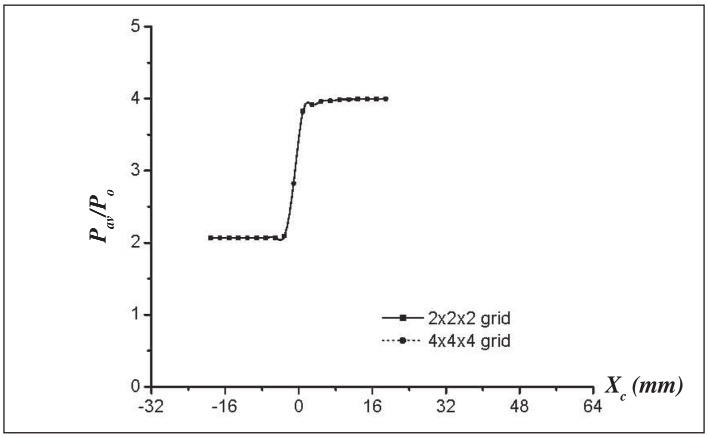

Figure 14: Average pressure (P_{av}/P_o) variations across the reflected shock wave for different grid sizes, where the origin, $X_c = 0.0$ corresponds to the shock location and X/m = 7.6

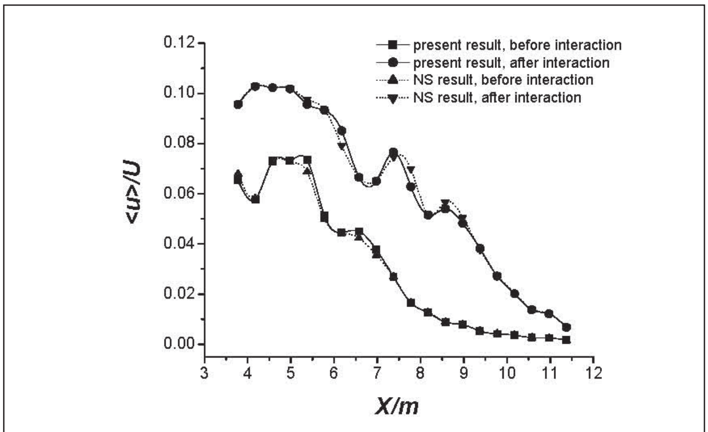

Figure 15: Comparison between the present simulation results and the NS results for the longitudinal turbulence intensity (<u>/U) along the centerline of the turbulent region before and after the shock/turbulence interaction

5.3 Comparison with the Navier-Stokes simulation (NS) results

For the purpose of the numerical code validation test, the present simulation results are compared with the Navier-Stokes simulation (NS) results and the results, obtained for shock Mach number 1.50, are used for this comparison. The comparison results indicate that the present threedimensional code with turbulence model is working very well for the present flow conditions. The turbulence model is used to solve some turbulence parameters directly and these turbulence parameters are used to determine the interaction effects properly. Navier-Stokes simulation (NS) is also performed for the shock or turbulence interaction with $M_s = 1.50$ where shock wave is captured. The solution of the Navier-Stokes equations is used to compare with the present simulation results and the present simulation results have the good agreements with the NS results.

The longitudinal turbulence intensity, $<u>/U$ before interaction and after interaction are characterised along the centerline of the turbulent region which is shown in Figure 15. The characteristic behaviors of the RMS value of longitudinal velocity fluctuations along the centerline of the turbulent region have the good agreements with the NS results and these agreements validate the present simulation results. The amplification of turbulent intensity and the amplification of turbulent kinetic energy level are determined for the shock wave interaction with turbulent field and these results are compared with the NS results, which are shown in Table 1.

Table-1: Comparison between the present simulation results and the NS results

Amplifications of	Incident shock Mach number	(Present simulation results)	(NS results)
Turbulent intensity	1.50	1.98~2.12	2.02~2.16
TKE level	1.50	3.08~3.41	3.20~3.55

Similarly the lateral velocity fluctuations, v'/U and w'/U are characterised along the centerline of the turbulent region and it is observed that the present computational results for the lateral velocity fluctuations, v'/U and w'/U have the good agreements with the NS results. The normalised pressure fluctuations characteristic curves before interaction and after interaction along the centerline of the turbulent region and it are shown that no substantial amplification of the pressure fluctuations occurs after interaction and it has good agreement with the NS results. The normalised average pressure, P_{av}/P_o variations are characterized across the reflected shock wave when the position of the reflected shock wave is in the turbulent region, which is shown in Figure 16 and the pressure profile obeys the shock reflection theory and also has the good agreement with the NS results. Even though all pressure values are not suitable for code validation but these are carrying good information about the characteristics of the selected turbulent region in the wake of the turbulence grid.

The solution of Navier-Stokes equations provides the information of turbulent kinetic energy (TKE) level in the flow field where the TKE is computed from the equation, 1/2 $(u'^2 + v'^2 + w'^2)$ and in this case, the values of TKE are directly related to the velocity fluctuations of the fluid particles. On the other hand, the TKE is obtained from the solution of two equations of k-ε turbulence model and the accuracy of the TKE value depends on the modeling equations. The values of TKE obtained from the velocity fluctuations of the fluid particles in the flow field are necessary to compare with the values of TKE obtained from the solution of two equations of k-ε turbulence model because all turbulence modeling equations are not ideal and it must have some deviations between these results. The comparisons between the TKE values obtained from the solution of Navier-Stokes equations and the solution of turbulence model are determined along the centerline of the turbulent region for M_s = 1.50 and the comparisons are shown in Figure 17. Using the equation, 1/2 $(u'^2 + v'^2 + w'^2)$, Rotman (1991) computed the TKE level in the flow field and it was observed that the maximum amplification factor of TKE level was 2.00 in the two dimensional computational results inside the Mach number range 1.01-1.50. The amplification of TKE level obtained from the velocity fluctuations is compared with the amplification obtained from the solution of turbulence model, which is shown in Figure 18, and it is observed in Figure 18 that the deviations between these results are 10 to 20 %.

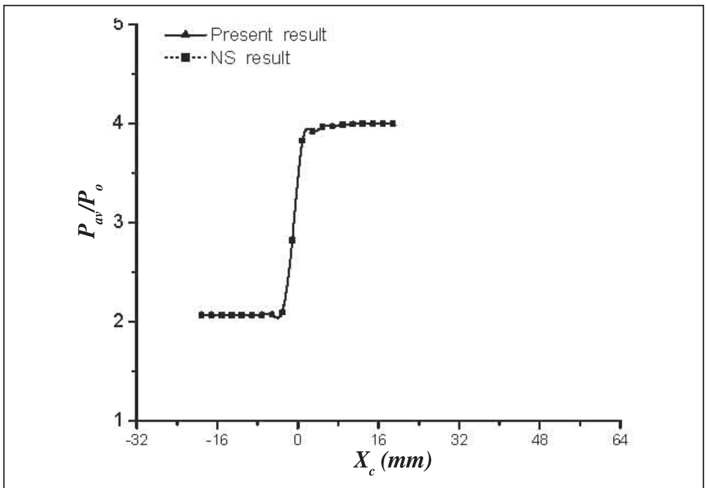

Figure 16: Comparison between the present simulation results and the NS results for the normalised average pressure (P_{av}/P_o) variation across the shock wave when the position of the shock wave is in the turbulent region and where the origin, X_c = 0.0 corresponds to the shock location and X/m = 7.6

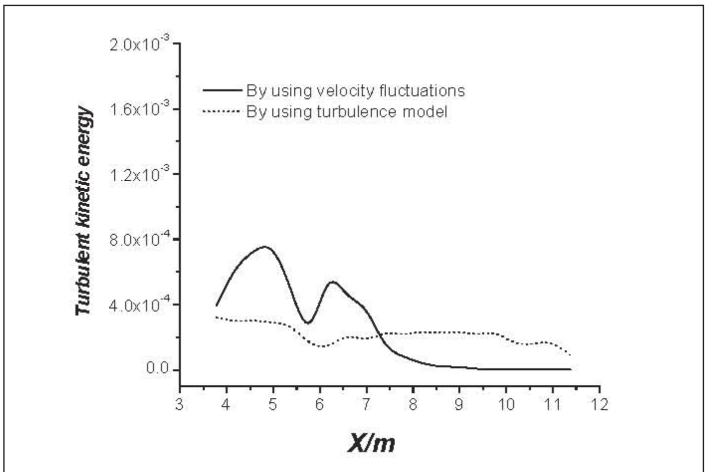

Figure 17: Comparison between the values of turbulent kinetic energy along the centerline of the turbulent region obtained from the velocity fluctuations and the turbulence model

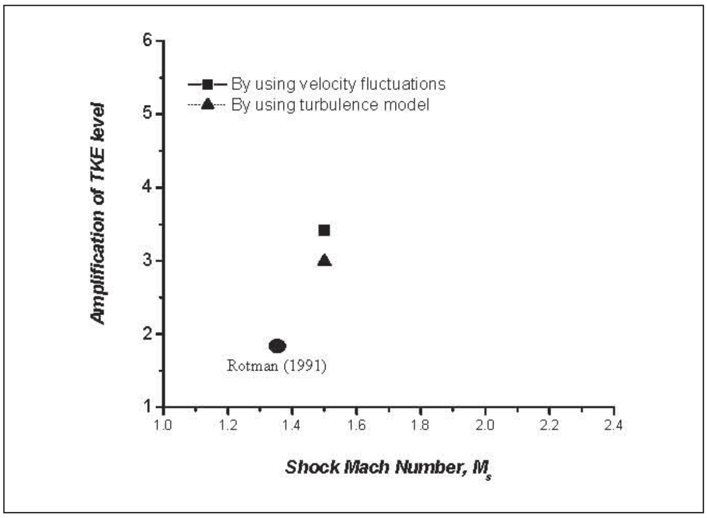

Figure 18: Comparison between the amplification of turbulent kinetic energy level obtained from the velocity fluctuations and the turbulence model

6.0 CONCLUSIONS

A good numerical simulation for nozzle flow depends on the throat area and the converging or diverging angle of the nozzle and the strength of the shock wave propagate through the throat of the nozzle. For small throat area of the nozzle, the flow separation will be high and blockage ratio will be low. In that case, it is necessary to select the shock wave strength comparatively high for good numerical simulations. So it is found that numerical results for higher shock Mach number have the good agreement with experimental results. Other flow parameters like fluid viscosity, Reynolds number also effect on the simulation results.

After the validation test of the Navier-Stokes equations, the extended three-dimensional Navier-Stokes equations with k-ε turbulence model are developed to solve almost all types of shock or turbulence interaction problems. Even though such type of computations is complex to get proper solution, but maximum simulated data agrees with the experimental results, performed by other researchers. In these computations, three-dimensional adaptive grids are used to get more accurate solution. Due to grid adaptation, the number of new cell, generated after refining operation, is twice the number of new cell, generated in two-dimensional adaptation and also adaptation is happened in the direction of the three Cartesian Coordinates. So the total number of cell difference between two subsequent refinement levels increases sharply, as a result, increases the computational time. The advantage of three-dimensional code is to solve all the turbulent parameters in the three-dimensional space system because the shock or turbulence interaction effect is one of the three-dimensional problems. The study of the grid convergence test has been performed successfully with different levels of grid refinement and also with different sizes of the grid. It is observed that all the simulation results are completely independent of the present grid system. The comparisons between the present simulation results and the NS results have been conducted successfully and it is observed that there have the good agreements between the present simulation results and the NS results. ■

REFERENCES

[1] Ribner HS. (1953) Convection of a pattern of vorticity through a shock wave, NACA TN-2864.

[2] Ribner HS. (1954) Shock-turbulence interaction and the generation of noise, NACA TN-3255.

[3] Ribner HS. (1969) Acoustic energy flux from shock-turbulence interaction, Journal of Fluid Mechanics 35: pp. 299-310.

[4] Kovasznay LSG. (1953) Turbulence in supersonic flow, Journal of the Aeronautical Science 20: pp. 657-682.

[5] Lighthill MJ. (1953) On the energy scattered from the interaction of turbulence with sound or shock waves. Proc. Camb. Phil. Soc, 49: pp. 531-551.

[6] Moore FK. (1953) Unsteady oblique interaction of a shock wave with a plane disturbances, NACA TN-2879.

[7] Kerrebrock JL. (1956) The interaction of flow discontinuities with small disturbances in a compressible fluid. Ph.D. thesis, California Institute of Technology.

[8] Ribner HS. (1987) Spectra of noise and amplified turbulence emanating from shock-turbulence interaction. AIAA J. 25: pp. 436-442.

[9] Anyiwo JC and Bushnell DM. (1982) Turbulence amplification in shock-wave boundary-layer interaction, AIAA J. 20: pp. 893-899.

[10] Sekundov AN. Supersonic flow turbulence and interaction with a shock wave, Izv. Akad. Nauk SSR Mekh. Zhidk. Gaza, March-April 1974.

[11] Donsanjh DS, (1964) Weeks TM. Interaction of a starting vortex as well as Karman vortex streets with traveling shock wave, AIAA paper No. 64-425.

[12] Chu BT and Kovasznay LSG. (1957) Non-linear interactions in a viscous heat- conducting compressible flow, Journal of Fluid Mechanics 3: p. 494.

[13] Devieve JF and Lacharme JP. (1986) A shock wave/ free turbulence interaction. Turbulent shear layer/shock wave interaction, edited by J. Delery, Springer-Verlag, Berlin.

[14] Jacquin L, Blin E and Geffroy P. (1991) Experiments of free turbulence/shock wave interaction, Proc. Turbulent shear flows, 8, tech Univ, Munich, Ger. p. 1-2-1-1-2-6.

[15] Debieve FR, Gouin H and Gaviglio J. (1982) Momentum and temperature fluxes in a shock wave-turbulence interaction. In Structure of Turbulence in heat and mass Transfer (ed. Z. P.Zaric). Hamisphere.

[16] Hesselink L and Sturtevant B. (1988) Propagation of weak shocks through a random medium, J. Fluid Mechanics 196: pp. 513-553.

[17] Richtmyer RD, (1960) Taylor instability in a shock acceleration of compressible fluids, Communications on Pure and Applied Mathematics 13: pp. 297-319.

[18] Meshkov EE. Izv. Akad. (1969) Instability of the interface of two gases accelerated by ashock wave, Nauk SSSR Mekh. Zhidk. Gaza 4: 151.

[19] Kuribayashi T.,Ohtani K., Takayama K., Menezes V., Sun M. and Saito T. (2007) Heat flux measurement over a cone in a shock tube flow, Shock Waves 16: pp. 275-285.

[20] Sun M and Takayama K (1999) Conservative smoothing on an adaptive quadrilateral grid, Journal of Computational Physics 150: pp. 143-18.

[21] Sasoh A., Matsuoka K., Nakashio K., Timofeev E., Takayama K., Voinovich P., Saito T., Hirano S., Ono S. and Makino Y. (1998) Attenuation of weak shock waves along pseudoperforated walls, Shock Waves 8: pp. 149-159.

PROFILES

ASSOC. PROF. DR MOHAMMAD ALI JINNAH is an Associate Professor in Department of Mechanical and Chemical Engineering, Islamic University of Technology (IUT) (An Organ of the OIC), Bangladesh. He obtained his Ph.D. from Tohuku University, Sendai, Japan in 2005 spesialising in Shock Wave interaction with turbulent flow. Het got his B. Sc Engineering (Mechanical) in 1993 and M.Sc. Engineering (Mechanical) in 18998 from BUET, Dhaka. He joined as an Assistant Engineer in Titas Gas T&D Company and served up to 2001. After getting his Ph.D, he joined as an Assistant Professor in IUT and is working stilll now.

EMERITUS PROF. KAZUYOSHI TAKAYAMA obtained his doctoral degree from Tohoku University in 1970 and was then appointed lecturer at the Institute of High Speed Mechanics, Tohoku University, promoted to Associate Professor in 1975 and to professor in 1986. He was appointed Director of the Shock Wave Research Center at the Institute of High Speed Mechanics in 1988. The Institute of High Speed Mechanics was restructured as the Institute of Fluid Science in 1989. He retired in 2004 and became Emeritus Professor of Tohoku University. In 1990 he launched Shock Waves, an international journal, taking on the role of managing editor and in 2002 became editor-in-chief. He was elected president of the Japan Society for Aeronautical and Space Sciences for one year in 2000 and was chairman of the Japanese Society of Shock Wave Research in 2000. He was appointed president of the International Shock Wave Institute in 2005. His research interests range from fundamental shock wave studies to the interdisciplinary application of shock wave research.

POSTURE, MUSCLE ACTIVITY AND OXYGEN CONSUMPTION EVALUATIONS AMONG METAL STAMPING OPERATORS: A PILOT STUDY IN MALAYSIAN SMALL AND MEDIUM INDUSTRIES

(Date received:25.5.2009/Date approved:10.8.2011)

Isa Halim[1], Abdul Rahman Omar[2] and Ahmad Rasdan Ismail.[3]
[1]*Faculty of Manufacturing Engineering, Universiti Teknikal Malaysia Melaka, Hang Tuah Jaya, 76100 Durian Tunggal, Melaka*
[2]*Faculty of Mechanical Engineering, Universiti Teknologi MARA, 40450 Shah Alam, Selangor*
[3]*Faculty of Mechanical Engineering, Universiti Malaysia Pahang, 22600 Pekan, Pahang*
E-mail: [1]isahalim@gmail.com

ABSTRACT

In the new era of world industrialization, ergonomics plays an important role to improve occupational health and productivity in most industries including small and medium industries (SMIs). However, SMIs in Malaysia do not put any priority on ergonomics awareness, for an example, by not designing the workstation ergonomically. As a consequence, operators are exposed to various ergonomic risk factors and prone to have ergonomic injuries. The objectives of this study are to evaluate working posture, muscle activity, and oxygen consumption while operators perform metal stamping process in a workstation, before and after the workstation is modified. The Rapid Entire Body Assessment (REBA), surface electromyography (SEMG), and oxygen analyser are used to evaluate working posture, muscle activity, and oxygen consumption respectively. Results of evaluations found that the modified workstation has reduced the physiological stress such as extreme posture, work/loading in the muscles as well as energy expenditure. The study concluded that an ergonomic workstation design can contribute significantly to improve physiological performance of the operators.

Keywords: *Metal Stamping Process, Muscle Activity, Oxygen Consumption, Workstation Design, Working Posture*

1.0 INTRODUCTION

In Malaysia, Small and Medium Industries (SMIs) has been recognised as one of the contributors to the growth of the nation's economy. Although the growth of Malaysian SMIs is rapid and their expansion is fast, they still face challenges that can affect their competitiveness. The companies under Malaysian SMIs have limitation in terms of ergonomics awareness, for examples, lack of materials handling equipment and improper workstation design. In addition, the efforts to enhance ergonomics awareness in Malaysian SMIs have several constrains in terms of manpower and availability of the service of ergonomits [1]. As a consequence of this, workplace conditions in the SMIs received very minimum intervention in ergonomics services. For example, the workstations for operators to perform the jobs are not designed ergonomically, thus exposing them to various difficulties such as extreme working posture, muscle fatigue, and the extra effort required to get the job done.

In industrial workplaces, designing a workstation is really important because it can contribute to feasible occupational health, job satisfaction, and work efficiency. Physiological factors such as posture, muscle activity and oxygen consumption should be critically studied when designing a workstation. Working posture can be defined as the orientation of body parts in space and in relation to each other while an operator performs a task [2].

Working posture is determined by the anthropometry of the operator, design of the workstation and the way the job is carried out. Dimensions, spatial position, orientation and design of workstation must be suited to the physical condition of the operator so that the operator can perform the task comfortably and safely in the workstation. The criteria for an ergonomic workstation design include locating materials and tools at appropriate height, thus making it easy to be reached by the operators. A proper workstation design will enable operators to practice safe working postures; otherwise it may contribute to awkward working postures [2].

In the design of a workstation, working height is very important. The height of the working surface should vary based on the operator's elbow height, and the type of work. A previous study pointed out working height, in general, should be set at 5 cm below the elbow level [3]. However, the working height can vary several centimeters, up or down, without any significant effect on performance [4]. A proper working height will allow a comfortable working posture. In contrast, inadequate posture from an improperly designed workstation can cause ergonomic injuries such as muscle strain, low back pain, and consequently decreased performance and productivity [5].

Popular methods to identify ergonomic risk factors in the workplace include observational method and direct technical measurement method. Usually, observational method is applied to obtain psychophysical feedbacks from respondents (operators) through personal interviews and questionnaire surveys.

Other tools include Rapid Upper Limbs Assessment (RULA) [6] and Rapid Entire Body Assessment (REBA) [7]. REBA is an ergonomic assessment tool that is specifically designed to assess working postures and movements corresponding to the tasks and workstations. It was developed on the basis of Rapid Upper Limbs Assessment (RULA) analysis, but it is also appropriate for evaluating tasks where the working postures are dynamic, static or where there are gross changes in posture [7]. Similar to RULA, this survey tool is useful when investigating postural stress during performance of tasks.

On the other hand, direct technical measurement method is applied to acquire information on physiological and biomechanical responses of subjects (operators). Normally, direct technical measurement method uses scientific tools which can measure specific parameters such as frequency, and voltage during the evaluations. The surface electromyography (SEMG) is one of the scientific instruments that has been applied to quantify muscle fatigue among operators while they are performing jobs [8-11].

The SEMG measures and records electromyography signals associated with the contraction of the muscles. It has been used in ergonomics for evaluation of operator performance associated with workstation design, for example, in the analysis of working posture for sedentary task [12], sewing operation [2] and manual materials handling [13].

Other equipment categorised under the direct technical measurement method is oxygen analyser. It is used to measure oxygen consumption of workers. The measurement of oxygen consumption is aimed to quantify the energy demands posed by the workstation design and task. Oxygen consumption can be defined as the volume of oxygen that is consumed by the worker during performing the task. This volume is expressed as a rate, either liter per minute (l/min) or milliliter per kilogram per minute (ml/kg/min). From the measurement of oxygen consumption, the energy expenditure of worker also can be obtained. A previous study quantified that 1 liter of oxygen consumed by the worker while performing task is equal to 21.2 kJ of energy needed by the worker [14]. Table 1 presents the amount of energy expenditure with respect to workload category.

Table 1: Classification of energy expenditure while performing task [14]

Workload Category	*Energy Expenditure*
Light task	Up to 10 kJ/min
Medium task	About 20 kJ/min
Heavy task	About 30 kJ/min

Realising the needs of ergonomic workstation design, this study was conducted to evaluate working posture, muscle activity, and oxygen consumption while operators perform metal stamping process at their workstation (existing design), and later at the modified workstation.

2.0 RESEARCH METHODS

Three metal stamping operators have participated as subjects in the study. The profile of the subjects:

- Age: mean = 20 years, SD = 2.0 years
- Gender: male
- Work experience: mean = 1 year, SD = 1.5 year
- Body mass: mean = 55.9 kg, SD = 3.3 kg
- Body height: mean = 1.7 m, SD = 0.07 m

The study was divided into two stages. During the first stage of the study, the evaluation was performed at the existing workstation (before the workstation design is modified). The second stage evaluation was carried out after the workstation was modified. Both stages analysed the same operators carrying out similar tasks. Before conducting the study, the researchers have obtained research approval regarding the methods and procedures from the Research Ethics Committee of Universiti Teknologi MARA.

2.1 Working Posture Evaluation

REBA [7] was used to analyse the working posture. The analysis can be done either using REBA Worksheet [7] or using computer programming to generate the results. Analysis using manual method (worksheet) may be time consuming and may lead to errors especially when large volumes of data have to be assessed. To overcome the shortcomings, computer programmed REBA was used to record, analyse and save all data and information regarding working posture analysis [15].

In the programmed REBA, the system has four graphical user interfaces. In the first graphical user interface, it records the profiles of operator to be assessed. This interface captures the information about personal particulars such as operator’s identification card number, operator’s name, position, age, weight, height, gender, marital status, service duration, working mode, alcohol consumption and smoking of cigarettes. The second graphical user interface records information regarding the workstation. This includes the task carried out in the workstation, and description of the task. In this graphical user interface also, the researcher has to tick the evaluation stage: whether the analysis is conducted before, or after ergonomic intervention is carried out in that workstation.

The third graphical user interface captures the information of operator’s body parts. The information includes the movements and postures of six body parts while performing the task in the workstation. The fourth graphical user interface presents the results of analysis. The result is presented in four parts: Part A, Part B, Part C and Part D. Part A presents the personal particulars of operator. This includes name of company, operator’s identification card number, operator’s name, position, and workstation. Part B describes the working posture of the operator while the task is performed. It includes the posture of the body parts such as trunk, neck, legs, upper arm, lower arm, and wrists. Part C presents the working condition of the operator in the workstation such as load handled, coupling condition and the style or movement of operator while performing a task. Part D presents the result of risk levels of ergonomic injury (in terms of REBA score) corresponding to working posture adopted by the operator. The REBA Score is expressed on a scale of 1 to 15, as tabulated in Table 2.

Table 2: Risk levels of ergonomic injury corresponding to REBA score

REBA Score	Risk Levels of Ergonomic Injury
1	Safe
2 - 3	Low
4 – 7	Medium
8 – 10	High
11 – 14	Very High

2.2 Muscle Activity Evaluation

The surface electromyography (SEMG) ME3000P4 (MEGA Electronics, Finland) and MegaWin Software were used to record, store and interpret all the data regarding to muscle activity of the operators. The SEMG system is equipped with surface electrodes attached conscientiously to operator's skin to detect the electromyography signals of operators while the task is performed. Eight muscles were selected for the evaluations: deltoid-medial part (left), deltoid-medial part (right), trapezius muscle (left), trapezius muscle (right), erector spinae muscle (left), erector spinae muscle (right), gastrocnemius muscle (left) and gastrocnemius muscle (right). The location of these muscles is clearly shown in Figure 1.

To ensure that the electrodes are attached properly to the muscles and other SEMG protocols were complied, a physiotherapist was consulted before the evaluation is carried out. The evaluation was performed early in the workday (8:30 am) on the first day of the week (Monday) to ensure the muscles to be analysed are free from the influence of previous task activities. All muscles of the operator were concurrently measured for more than 30 minutes during the performance of the tasks.

Setting of SEMG system was based on Surface EMG for the Non-Invasive Assessment of Muscles (SENIAM) [16]. The settings are as follows:

- EMG electrodes: Surface electrode Ag/AgCl, 20 mm diameter
- Distance between electrodes: 25 mm
- Skin preparation: Shaved, clean, and scrubbed with alcohol
- Common Mode Rejection Rate (CMMR): 110 dB
- Filter: Band pass filter (85 Hz – 500Hz)
- Sampling rate: 1000 Hz

The measurements of muscle activity were conducted based on real time monitoring. All SEMG electrodes were connected to a data logger to record and store the electromyography signals. Then, the data logger was connected to a PC screen using wireless connection to display and monitor the electromyography signals. Before beginning the test, the personal particulars of the operator were recorded in MegaWin Software, and the operator was given sufficient time to get enough practice to familiarise with the SEMG instruments. The operator was also informed that he has to perform the task at his own pace and should immediately report any feeling of pain or discomfort so that the measurement can be terminated. After all the measurement settings are ready, the operator can now start to perform his task.

2.3 Oxygen Consumption Evaluation

In this study, the Metamex Cortex, Germany and MetaSoft® 3 Software were used to measure and analyse operators' oxygen consumption while performing their task at the workstation. During the measurement, the instrument is attached to the operator's body as shown in Figure 1 below.

Figure 1. Selected muscles were attached with Ag-AgCl electrodes: deltoid-medial part (shoulder region); trapezius muscle (neck region); erector spinae (lower back), gastrocnemius muscle (leg region). An operator is equipped with a chest-mounted light-weight oxygen analyzer on his body to measure oxygen consumption (right).

3.0 EXPERIMENTAL STUDY

3.1 Before Modification of the Workstation

Operators perform metal stamping process manually by feeding the workpiece into the stamping machine. The process consists of moving raw materials from the floor to the stamping machine. The operator lifted the materials weighing about 300g each, which are to be stamped at the rate of 5 to 8 movements per minute.

During the process, the operator stands in front of the stamping machine and feeds the raw materials into the machine die using both hands. The starting position was at upright posture (~90 degrees with respect to the body midline) whereby the body is close to the machine. As shown in Figure 2, the raw materials were placed in a bucket located on the floor on the right side of operator. The distance between operator's hand and the raw materials is approximated about 100 cm. The operator has to bend his body downwards to reach the materials as the bucket was in a low level.

At this instant, the distance of his shoulder and the floor is 100 cm as demonstrated in Figure 3. After a raw material has been grabbed, it will be transferred to the machine die for stamping process. As illustrated in Figure 4, operator feeds the raw material to machine die at a distance of 70 cm from his body. The machine which has capacity of 110 tons will shape the raw material according to the geometry or pattern of the die. The finished parts will be thrown into another bucket on the left side of operator. In this condition, the operator is in upright working posture, but he has to slightly bend his body to the left side as shown in Figure

5. The process is repetitive in nature, in that the operator has to perform the task continuously for 8 hours (with stop only for tea break and lunch). The temperature in the work environment was 27ºC to 31ºC.

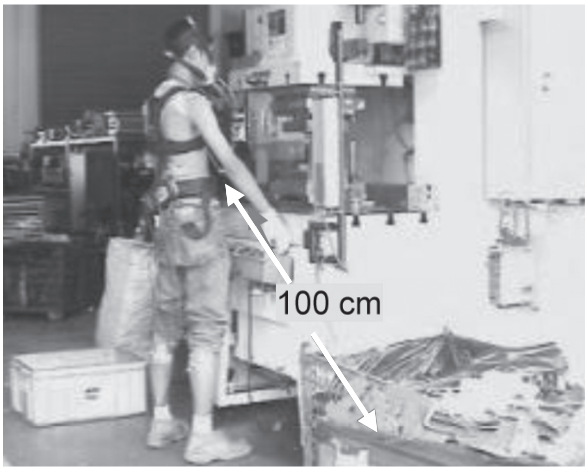

Figure 2: Operator stands in front of the machine

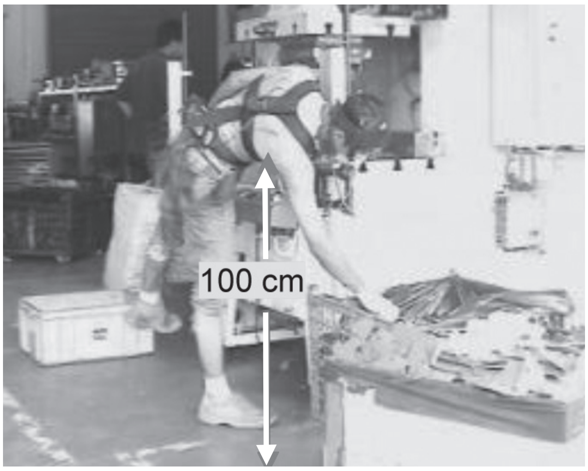

Figure 3: Operator reaches the material

Figure 4: Operator feeds the material into the machine die

Figure 5: Operator throws the finished part

3.2 After Modification of the Workstation

The workstation is later modified to improve the physiological performance of operators. A duration of four months was given to ensure the operators familiar with the new design of workstation. This intervention is essential to reduce muscle fatigue especially in the lower limbs. Two items were introduced to the workstation, namely an adjustable table to place the bucket, and a sit-stand stool.

As illustrated in Figure 6, the adjustable table was used to raise or lower the height of bucket containing the raw materials. When the bucket is at an appropriate level (elbow height), the operator is able to reach easily for the raw material from the bucket to feed them into the machine die. With the bucket at an appropriate level, bending posture has been eliminated. Meanwhile, the sit-stand stool was introduced to enable the operator to work in both sitting and standing postures. The sit-stand stool was also equipped with a foot rest to provide comfort for the operator's legs.

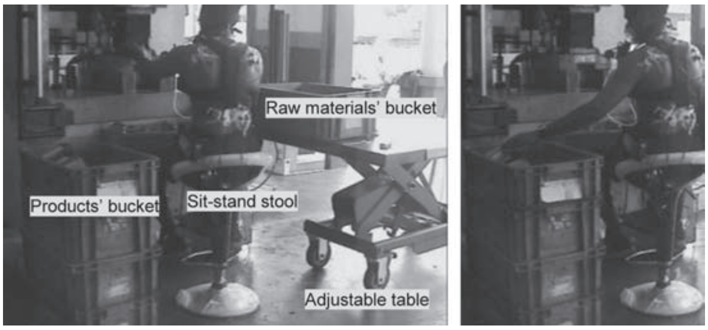

Figure 6: Operator performs metal stamping process at the modified workstation

4.0 RESULTS AND DISCUSSIONS

4.1 Results of Working Posture Evaluation (Before Modification of the Workstation)

At the existing workstation, the operators adopted four working postures while performing metal stamping process which were: standing, bending, feeding and throwing postures. The results of each working posture associated with existing workstation design are presented in Table 1. The results of standing posture show that the first and second operators obtained REBA score of 3, while the third operator acquired a REBA score of 2. According to REBA, such results indicate that the standing posture is safe to the operators as indicated by low REBA scores [7]. While in the standing posture, the operators perform the task with their trunks in upright position with their feet apart. This posture allowed the operators to perform the task in neutral working posture and standing in a stable position.

The results of bending posture found for all operators gave high REBA scores. This is due to bending of the trunk downwards and the left leg is slightly hung. This posture affects the lower back of operators because they have to perform the task in bending and standing in an unstable position. As a consequence, the operators were exposed to a high risk for ergonomic injuries associated with low back pain. REBA suggests that the working posture required further improvement [7].

The results of feeding posture show that the posture of first and third operators were safe as they obtained REBA score of 2. However, the second operator experienced medium risk for ergonomic injuries as he obtained REBA score of 4, and this requires further improvement [7]. While in feeding posture, the operators perform task in a standing posture with their trunks in upright position and their arms slightly extended.

Based on the results of throwing posture, both first and second operators were exposed to high risk for ergonomic injuries as they obtained REBA score of 8. The third operator has a slightly lower REBA score of 7, with medium risk for ergonomic injuries This posture can affect the operators because they have to slightly bend their body to left side while throwing the finished products into the bucket.

Table 3 summarises the results of working posture evaluation for each operator while they perform the task at the existing workstation. From the table, it can be concluded that both bending and throwing postures can contribute significantly to ergonomic injuries as they obtained high REBA scores. The bending and throwing postures may affect the lower back especially the erector spinae muscle.

Table 3: Results of working posture evaluation using REBA (Before modification of the workstation)

Operator	*Standing*	*Bending*	*Feeding*	*Throwing*
Operator 1	3	9	2	8
Operator 2	3	10	4	8
Operator 3	2	10	2	7

4.2 Results of Working Posture Evaluation (After Modification of the Workstation)

The second stage evaluations were conducted four months later after the workstation has been modified. At the modified workstation, the operators adopted four working postures: sitting posture, reaching posture, feeding posture and putting posture. For the sitting posture, the first and second operators obtained REBA score of 3, while the third operator obtained a score of 2. This indicates the sitting posture can be considered safe for the operators. While performing the task in sitting posture, the operators' trunks are in upright position and their legs are well supported by the foot rest of sit-stand stool as shown in Figure 7. Instead of sitting, the sit-stand stool also allowed the operators perform the task in standing posture. They can choose either to stand or to sit, whichever they feel comfortable with. As a consequence of this intervention, the operators' risk for ergonomic injuries has been reduced.

For the reaching posture, the first and third operators acquired a REBA score of 2, while the second operator acquired a score of 3. The results show that the reaching posture can also be considered safe to the operators. The reaching posture showed a positive result because the operators can easily reach the raw materials now. This is due to the adjustment made to the height of raw materials, which has been raised to an appropriate level (elbow height) using an adjustable table.

For the feeding posture, both the first and third operators acquired a REBA score of 3, while the second operator acquired a score of 4. The results indicate that the feeding posture is still safe for the operators. While adopting feeding posture, the operators' hands are parallel to the machine die so that they can feed the raw materials into the machine die easily.

For the putting posture, all operators acquired a REBA score of 2, indicating that the posture is safe for the operators. This is due to the fact that the height of the bucket was adjusted to an appropriate level and positioned as close as possible to the operators to enable them to place the finished products into the bucket easily.

Table 4 summarizes the results of working posture evaluation for each operator while they perform metal stamping process at the modified workstation design. From the tabulated results, it can be concluded that the current working postures are safe, and there is a low risk of ergonomic injuries.

Table 4: Results of working posture evaluation using REBA score (After modification of the workstation)

Operator	*Sitting*	*Reaching*	*Feeding*	*Putting*
Operator 1	3	2	3	2
Operator 2	3	3	4	2
Operator 3	2	2	3	2

4.3 Improvement of Working Posture

This section presents the effectiveness of modified workstation by comparing the results of working posture evaluation. From Figure 7 to Figure 9, it can be observed that the modified workstation can reduce the risk for ergonomic injuries as proved by decrement of REBA score. For the first operator (Figure 7), the modified workstation significantly reduced the REBA score from 9 to 2 when reaching for the raw materials. Meanwhile the REBA score for placing the finished products into finished products' bucket was reduced from 8 to 2. As illustrated in Figure 8, the modified workstation had significantly reduced the REBA score when reaching for the raw materials from 10 to 3 for the second operator. Meanwhile the REBA score for placing the finished products into finished products' bucket was reduced from 8 to 2. Figure 9 shows an improvement for the working posture of third operator was also improved through implementation of the modified workstation. The REBA score when reaching for the raw materials was reduced from 10 to 2. The REBA score when placing the finished products into bucket was also reduced from 7 to 2. The results of these evaluations clearly show that the modified workstation is capable of improving the working posture of operators.third operator was also improved through implementation of the modified workstation. The REBA score when reaching for the raw materials was reduced from 10 to 2. The REBA score when placing the finished products into bucket was also reduced from 7 to 2. The results of these evaluations clearly show that the modified workstation is capable of improving the working posture of operators.

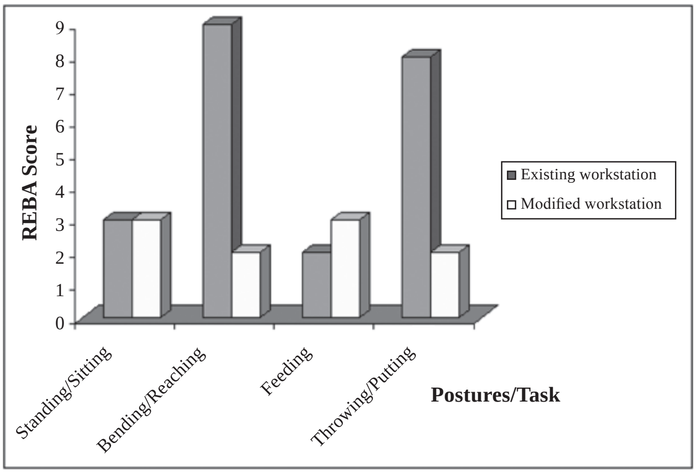

Figure 7: Comparison result of working posture evaluation for the first operator

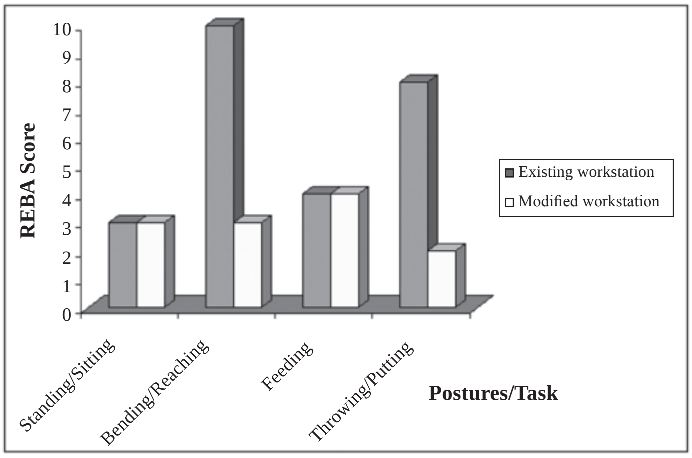

Figure 8: Comparison result of working posture evaluation for the second operator

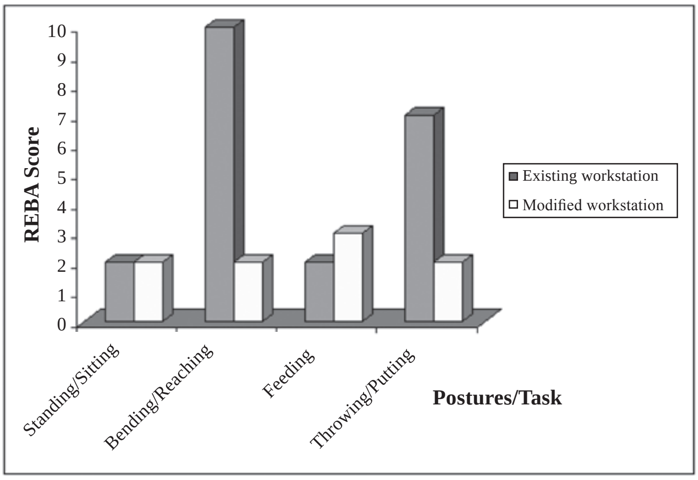

Figure 9: Comparison result of working posture evaluation for the third operator

4.4 Results of Muscle Activity Evaluation (Before Modification of the Workstation)

The following sections discuss the results of muscle activity while the operators perform the task at the existing workstation. These results described the response of operators' muscles corresponding to their working posture and task. Two types of analyses, namely raw signals analysis and work/loading analysis were performed to determine the impact of existing workstation on operators' muscles.

4.4.1 Raw Signal Analysis (before modification of the workstation)

The results of raw signal analysis represent the myoelectric signals from the operators' muscles corresponding to their task load. The myoelectric signals are measured in microvolts (µVs) and they indicate the efforts of the particular muscles to perform the tasks. If the myoelectric signals are high, it means that the muscles require high effort for the particular tasks.

Through visual interpretation, it is easy to determine the muscles that require high effort due to working posture and task. Based on raw signals obtained from the SEMG, it can be observed that the lower limb muscles, namely both left and right trapezius muscle, both left and right rector spinae muscle and both left and right gastrocnemius muscle for the first operator required higher effort than the upper limb's muscles, both left and right deltoid medial part as indicated by the high of myoelectric signals. Also, the side loading of this operator was unbalanced as shown in Table 5.

The right side loading gave on average higher myoelectric signals (486642 µVs or 58.6%) than the left side loading (273624 µVs or 41.4%). The effort required by left gastrocnemius muscle of second operator was slightly higher than the other muscles. However the side loading of this operator was better balanced as indicated by the result in Table 5, whereby the average right side loading of the myoelectric signals was 144000 µVs (48.5%) and the left side loading was152988 µVs (51.5%). Both left and right trapezius muscle and right gastrocnemius muscle of the third operator required higher effort than the other muscles. The side loading of this operator was unbalanced whereby the loading on the left side recorded higher myoelectric signals (251866 µVs or 54.4%) as compared to the right side loading (211210 µVs or 45.6%). From the results of raw signals analysis, it can be summarised that the lower limb muscles require more effort than upper limb muscles while the operators perform tasks at the existing workstation.

Meanwhile, from the comparison of side loading in Table 5, it can be summarised that the operators' muscles loading were unbalanced as indicated by average myoelectric signals and the percentage of side loading. This is due to the particular muscles being stressed significantly while the operators perform the tasks. For instance, when the operators reached for the raw materials placed in the bucket on the floor, they have to bend their body downwards.

Table 5: Results of myoelectric signals and percentage of side loading (Before modification of workstation)

Operator	*myoelectric signals (left side)*	*myoelectric signals (right side)*	*% of loading (left)*	*% of loading (right)*
1	273624 µVs	486642 µVs	41.4%	58.6%
2	152988 µVs	144000 µVs	51.5%	48.5%
3	251866 µVs	211210 µVs	54.4%	45.6%

4.4.2 Work/Loading Analysis (before modification of the workstation)

Table 6 summarises the results of amount work/loading exerted by the operators' muscles. The first operator experienced highest work/loading in the both left and right erector spinae muscle corresponding to myoelectric signals of 90676 µVs and 184665 µVs respectively. In other words, the work/loading exerted on these muscles are higher than the other muscles. The second operator obtained high work/loading in the left and right trapezius muscle with respect to myoelectric signals of 120486 µVs and 66603 µVs respectively.

Meanwhile, the third operator obtained high work/loading in the left and right erector spinae muscle corresponding to myoelectric signals of 46649 µVs and 59518 µVs respectively. It can be summarised that the effort and work/loading were concentrated in the lower limb muscles. This may be due to the bending and throwing postures while the operators reach for the raw materials in the low position and throwing the finished products into the bucket.

Table 6: Results of work/loading exerted in the muscles (Before modification of the workstation)

Operator	*DL*	*DR*	*TL*	*TR*	*EL*	*ER*	*GL*	*GL*
1	49518 µVs	44941 µVs	85453 µVs	84715 µVs	90676 µVs	184665 µVs	47977 µVs	72320 µVs
2	46388 µVs	47521 µVs	120486 µVs	66603 µVs	62529 µVs	55387 µVs	22462 µVs	41698 µVs
3	35341 µVs	29785 µVs	33452 µVs	23273 µVs	46649 µVs	59518 µVs	37546 µVs	31424 µVs

Note: DL- Left deltoid medial part, DR- Right deltoid medial part, TL- Left trapezius, TR- Right trapezius, EL- Left erector spinae, ER- right erector spinae, GL- Left gastrocnemius, GR- Right gastrocnemius.

4.5 Results of Muscle Activity Evaluation (After Modification of the Workstation)

The following sections will discuss the results of muscle activity while the operators perform the task at the modified workstation.

4.5.1 Raw Signal Analysis (After modification of the workstation)

After the workstation has been redesigned, the first operator required less effort in the lower limb muscles, namely erector spinae muscle, gastrocnemius muscle and left deltoid-medial part as indicated by low myoelectric signals. However, the myoelectric signals in the right deltoid-medial part and trapezius muscle showed that these muscles require slightly high effort when compared to other muscles.

In addition, the side loading of this operator was unbalanced whereby the loading in the left side obtained lower myoelectric signals (170054 µVs or 37.6%) when compared to the right side (282696 µVs or 62.4%). For the second operator, both left and right trapezius muscles require slightly higher effort than the other muscles. The side loading was also unbalanced; the loading in the left side acquired higher myoelectric signals (197845 µVs or 62.9%) compared to the right side loading (116462 µVs or 37.1%).

Similarly, the third operator required higher effort in the left and right trapezius muscles than the other muscles. However, the side loading of this operator had better balance; the right side loading obtained myoelectric signals of 144085 µVs (54.6%), while the left side loading acquired myoelectric signals of 119574 µVs (45.4%).

Based on the results of raw signals analysis, it can be summarised that the upper limb muscles required more effort compared to lower limb muscles when the operators perform task at the modified workstation. Furthermore, comparison of side loadings results in Table 7 revealed that the muscle loading were unbalanced.

Table 7: Results of myoelectric signals and percentage of side loading (After modification of workstation)

Operator	myoelectric signals (left side)	myoelectric signals (right side)	% of loading (left)	% of loading (right)
1	170054 µVs	282696 µVs	37.6%	62.4%
2	197845 µVs	116462 µVs	62.9%	37.1%
3	119574 µVs	144085 µVs	45.4%	54.6%

4.5.2 Work/Loading Analysis (After modification of the workstation)

Table 8 presents the average of work/loading exerted to each muscle for all operators when performing tasks at the modified workstation. The work/loading in the lower limb muscles such as erector spinae muscle and gastrocnemius muscle is considered minimum. In contrast, the work/loading in the upper limb muscles such as deltoid medial part and trapezius muscle was greater. This may be due to the operators perform the task in sitting position continuously. As a consequence, the work/loading is concentrated in the upper limb muscles. The first operator experienced high work/loading in the left and right trapezius muscles corresponding to myoelectric signals of 90676 µVs and 184665 µVs respectively. The same result was obtained by the second and third operators.

Table 8: Results of work/loading exerted in the muscles (After modification of the workstation)

Operator	DL	DR	TL	TR	EL	ER	GL	GL
1	24908 µVs	81374 µVs	107447 µVs	113612 µVs	22231 µVs	19763 µVs	4350 µVs	7530 µVs
2	54290 µVs	58717 µVs	109177 µVs	115668 µVs	14372 µVs	15255 µVs	5491 µVs	3394 µVs
3	46665 µVs	48817 µVs	126320 µVs	149759 µVs	12484 µVs	20137 µVs	4450 µVs	6983 µVs

Note: DL- Left deltoid medial part, DR- Right deltoid medial part, TL- Left trapezius, TR- Right trapezius, EL- Left erector spinae, ER- right erector spinae, GL- Left gastrocnemius, GR- Right gastrocnemius.

4.6 Improvement of Muscle Activity

Figure 10 through Figure 12 show an analysis of the results of muscle activity evaluation associated with work/loading for all operators. Figure 10 shows the results of work/loading exerted in the muscles of first operator, Figure 11 for the second operator and Figure 12 for the third. From the analysis, it can be observed that the work/loading in the lower limb muscles has decreased drastically with the implementation of modified workstation in all the three cases. However, the work/loading in the upper limb muscles (left and right trapezius muscles) showed a drastic increment. From the comparison results, the modified workstation can be considered as a potential solution to improve muscle activity of operators.

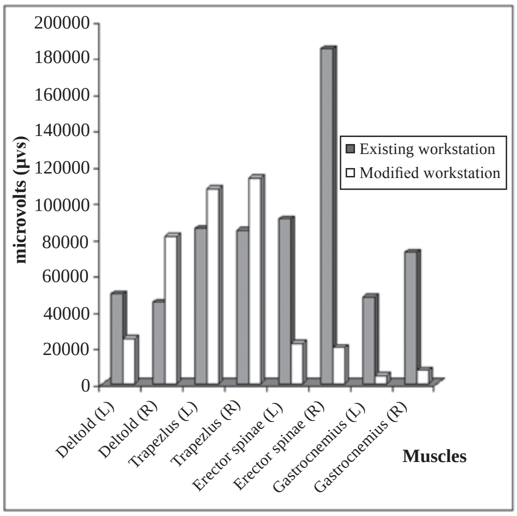

Figure 10: Comparison result of work/loading exerted in the muscles of first operator

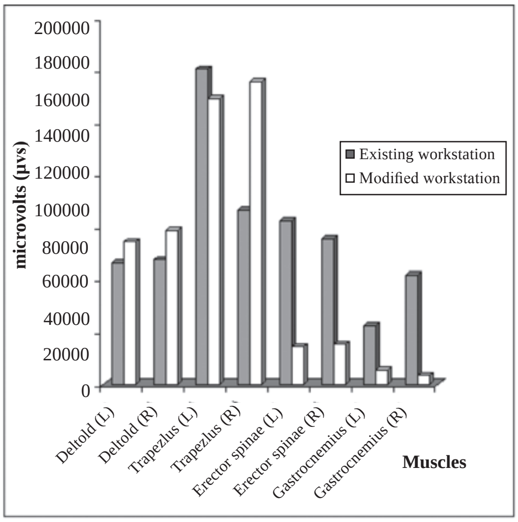

Figure 11: Comparison result of work/loading exerted in the muscles of second operator

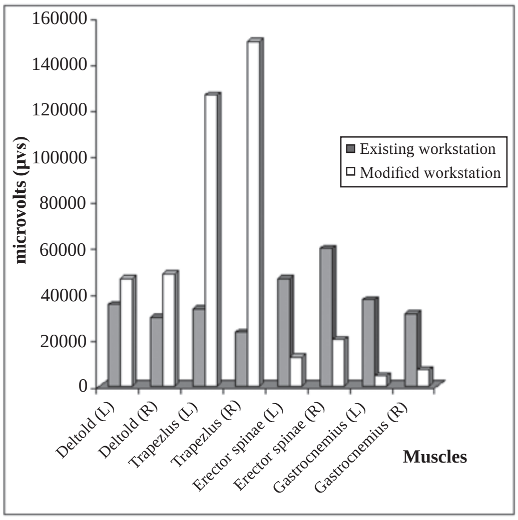

Figure 12: Comparison result of work/loading exerted in the muscles of third operator

4.7 Results of Oxygen Consumption Evaluation (Before Modification of the Workstation)

Table 9 presents the results of oxygen consumption evaluation for each operator while they perform task at the existing workstation. The first operator consumed 0.735 l/min of oxygen, equivalent to a demand for 15.582 kJ/min of energy. The second and third operator recorded lower oxygen consumption and energy demand than the first operator. The second operator consumed 0.465 l/min of oxygen equivalent to a demand for 9.858 kJ/min of energy. The third operator consumed even less oxygen and energy when compared to the first and second operators as indicated by the results presented in Table 9. These results can be taken as the baseline for the oxygen consumption and energy expenditure of operators while performing the task at the existing workstation. It should be noted that these values are still within acceptable limits (about 20 kJ/min for the workload categorised under medium task [14]). However, these consumptions can still be improved to optimize the capability of operators while performing the tasks.

Table 9: Results of oxygen consumption evaluation (Before modification of the workstation)

Operator	*Oxygen consumption (l/min)*	*Energy expenditure (kJ/min)*
Operator 1	0.735	15.582
Operator 2	0.465	9.858
Operator 3	0.295	6.254

4.8 Results of Oxygen Consumption Evaluation (After Modification of the Workstation)

Table 10 presents the results of oxygen consumption evaluation when the operators perform the tasks at the modified workstation. From the tabulated results, it can be summarised that the first operator consumed oxygen of 0.291 l/min equivalent to an energy demand of 6.169 kJ/min. The second and third operators recorded slightly lesser oxygen consumption and energy expenditure than the first operator. The second operator consumed 0.336 l/min of oxygen or demanded 7.123 kJ/min of energy. The third operator recorded even less oxygen consumption when compared to the first and second operators as indicated by results presented in Table 10. From such presented results, it can be summarised that the oxygen consumption and energy expenditure of operators while performing task at the modified workstation are within acceptable limits.

Table 10: Results of oxygen consumption evaluation (After modification of the workstation)

Operator	*Oxygen consumption (l/min)*	*Energy expenditure (kJ/min)*
Operator 1	0.291	6.169
Operator 2	0.336	7.123
Operator 3	0.131	2.777

4.9 Improvement of Oxygen Consumption

A pre-post evaluation on oxygen consumption was conducted to determine the impact of modified workstation in relation to oxygen consumption and energy expenditure of operators. Figure 13 and Figure 14 show the comparison results of oxygen consumption and energy expenditure for all operators. The first operator consumed 0.735 l/min of oxygen while performing the task at the existing workstation, whereas 0.291 l/min of oxygen was consumed while performing the task at the modified workstation. The energy expenditure also showed the improvement, whereby 15.582 kJ/min of energy was demanded while performing the task at the existing workstation, reduced to 6.169 kJ/min while performing the task at the modified workstation.

The second operator consumed 0.465 l/min of oxygen while performing the task at the existing workstation, compared to 0.336 l/min of oxygen while performing the task at the modified workstation. On the other hand, the energy expenditure also showed the improvement, whereby 9.858 kJ/min of energy was demanded while performing the task at the existing workstation, reduced to 7.123 kJ/min at the modified workstation.

The third operator consumed 0.295 l/min of oxygen while performing the task at the existing workstation, reduced to 0.131 l/min of oxygen at the modified workstation. Consequently, the energy expenditure also showed the improvement, whereby 6.254 kJ/min of energy was demanded while performing the task at the existing workstation, decreased to 2.777 kJ/min at the modified workstation.

From the comparison results, it can be summarised that the energy expenditure for all operators are within acceptable limits while performing the task at the modified workstation. The findings showed that the modified workstation is capable of optimising oxygen and energy consumption of operators, thus enabling the operators to perform the given task with minimum oxygen and energy consumption.

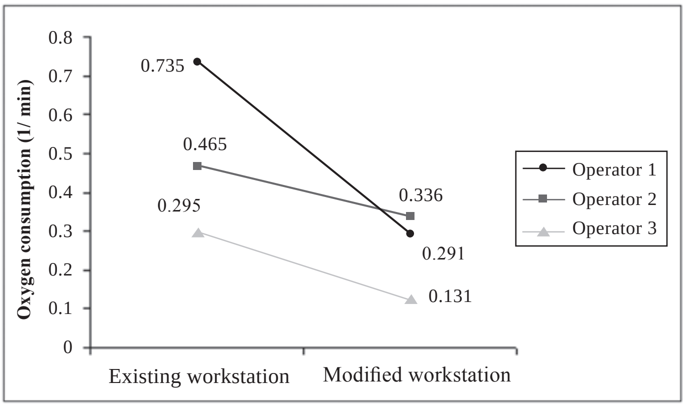

Figure 13: Comparison result of oxygen consumption for all operators

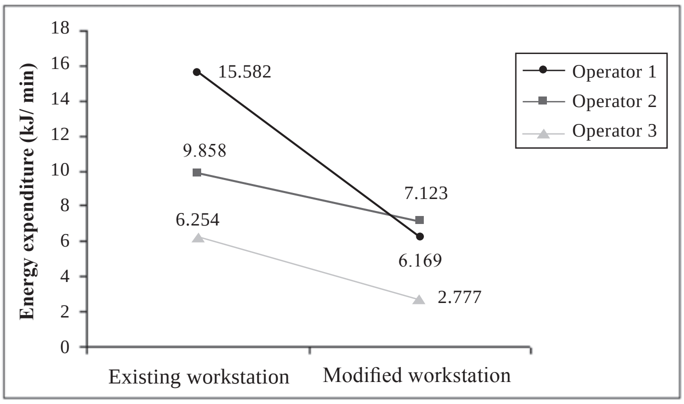

Figure 14: Comparison result of energy expenditure for all operators

5.0 CONCLUSION

This study has conducted two-phase evaluations to determine the impact of workstation design to working posture, muscle activity, and oxygen consumption of metal stamping operators while they perform their tasks. The first phase evaluation was conducted before the workstation was modified, and the second phase evaluation was performed after the modification. From the first phase evaluation, results show that bending posture has potential for significantly causing ergonomic injuries. The lower limb muscles especially the left and right erector spinae muscles are subject to high work/loading. This is due to the extra work/loading exerted on this muscle while the operators perform the task in bending posture. However, evaluation of oxygen consumption indicate the oxygen and energy consumed by the operators while performing the task was still within acceptable limits. Based on second phase evaluation, the results show that the modified workstation has improved the working posture, reduced the work/loading in the lower limb muscles, and required less oxygen and energy while performing the task. In conclusion, this study concluded that the implementation of this modified workstation had a positive impact on the physiological performance of the operators.

6.0 ACKNOWLEDGMENTS

The authors would like to thank the Universiti Teknikal Malaysia Melaka (UTeM), the Universiti Teknologi MARA (UiTM) and Extra-Built Sdn Bhd for the administrative assistance and facilitation of the experimental study. ■

REFERENCES

[1] Razlan M, Win K and Rampal K G (2000). “Work-related musculoskeletal symptoms among batik workers in Kelantan”. Malaysian Journal of Medical Sciences. 7(2): pp13-17.

[2] Nico J D and Jan D (2002). “Sewing machine operation: workstation adjustment, working posture and worker perceptions”. International Journal of Industrial Ergonomics. 30(6): pp341-353.

[3] Konz S (1967). “Design of work stations”. J. Ind. Eng. 18: pp413–428.

[4] Konz S (1990). “Work Design”. Industrial Ergonomics, 3rd Edition. Publishing Horizons, Scottsdale, AZ.

[5] Corlett E N, Bowssenna M and Pheasant S T (1982). Is discomfort related to the postural loading of the joints?. Ergonomics. 25: pp315-322.

[6] McAtamney L and Corlett E N (1993). “RULA: a survey method for the investigation of work-related upper limb disorders”. Applied Ergonomics. 24 (2):pp91-99.

[7] Hignett S and McAtamney L (2000). Rapid entire body assessment (REBA). Applied Ergonomics. 31: pp201-205.

[8] Lone H, Jorgen and W, Kurt J (1998). “Significance of mat and shoe softness during prolonged work in upright position: based on measurements of low back muscle EMG, foot volume changes, discomfort and ground force reactions”. Applied Ergonomics. 29: pp217-224.

[9] Ahmad N, Taha Z and Eu P L (2006). “Energetic requirement, muscle fatigue, and musculoskeletal risk of prolonged standing on female Malaysian operators in the electronics industries: influence of age”. Engineering e-Transaction. 1: pp47-58.

[10] Min-Chi C and Mao-Jiun J W (2007). “Professional footwear evaluation for clinical nurses”. Applied Ergonomics. 38: pp133-141.

[11] Diane E G and Jack P C (2008). “Prolonged standing as a precursor for the development of low back discomfort: an investigation of possible mechanisms”. Gait & Posture. 28: pp86-92.

[12] Goossens R H M, Snijders C J, Roelofs G Y and Buchem F V (2003). “Free shoulder space requirements in the design of high backrests”. Ergonomics. 46(5): pp518-530.

[13] Kamal K and Berman K. (2001). “Workplace layout for seated manual handling tasks: an electromyography study”. International Journal of Industrials Ergonomics. 27(1): pp19-32.

[14] Karl Kroemer, Henrike Kroemer and Katrin Kroemer-Elbert. Ergonomics – How to Design for Ease and Efficiency. Prentice Hall International, Inc. New Jersey, 1994.

[15] Isa Halim (2006). “Ergonomics participatory opportunities for occupational health enhancement in Malaysian SMIs”. The Universiti Teknologi MARA, Malaysia.

[16] Freriks B and Hermens H (2000). “European Recommendation for Surface Electromyography: Result of SENIAM Project”. Roessignh Research and Development, The Netherlands.

PROFILES

EN. ISA HALIM is a lecturer at Faculty of Manufacturing Engineering, Universiti Teknikal Malaysia Melaka (UTeM). He received B. Eng. (Hons.) Mechanical in 2004, MSc. in Mechanical Engineering in 2006, and PhD in Mechanical Engineering in 2011 from the Universiti Teknologi MARA (UiTM). His research interests are Industrial Ergonomics and Occupational Health and Safety.

IR. AHMAD RASDAN ISMAIL is a corporate member of IEM as well as professional engineer registered with the BEM. He holds a Bachelor Mechanical Engineering. (Hons) (UKM) as well as a M.Sc in Manufacturing Systems Engineering (UPM). He is currently a senior lecturer and head of industrial engineering programme at the Faculty of Mechanical Engineering, Universiti Malaysia Pahang. His research interests include industrial ergonomics related to environmental ergonomics. He is also noise competent person registered under DOSH Malaysia and also a registered consultant for Noise and Vibration under DOE Malaysia.

IR. PROF. DR HJ. ABDUL RAHMAN OMAR is Deputy Vice Chancellor (Research and Innovation) of Universiti Teknologi MARA (UiTM). He holds PhD in Computer Integrated Manufacturing (CIM) from the University of Loughborough, U.K in 1997. In addition, he received MSc. in Control Systems (1990) and Advance Diploma in Mechanical Engineering (1984) from the University of Sheffield, U.K and Universiti Teknologi MARA respectively. His areas of expertise include CAD/ CAM, CIM, Concurrent Engineering, Knowledge Based Modelling, Control Systems, and Industrial Ergonomics. He has published more than 70 technical papers in chapter of books, international and national journals as well as conference proceedings.

Subscribe to IEM's Publications Now!

Yes! I would like to be a subscriber of The Institution of Engineers, Malaysia's publications

Name: ______________________________

Mailing Address: ______________________________

______________________________ Country: ______________

Company/Institution: ______________________________

Title: ______________________________

Telephone No: ______________ Fax: ______________ Email: ______________

☐ New Subscriber ☐ Renewal

Please commence my subscription from: ______________(month/year) Signature: ______________

To start your subscription of IEM's publications, complete this form and mail it back to the address below. For faster processing, fax it to: (603) 8070 0047. Thank you.

What is your primary job title?

- ☐ Corporate Management (including chairman, president, proprietor, partner, director, vice president, general manager, division manager, import/export manager, other corporate title)
- ☐ Management (including project/contract/equipment/service/transport district manager, clerk of works, other technical or operating manager)
- ☐ Engineering/Design (including chief engineer, chief designer, civil/highway/mechanical/planning engineer, other engineering/design title)
- ☐ Buying/Purchasing (including chief buyer, buyer, purchasing officer, other buying/purchasing title)
- ☐ Titles allied to the field (architect, consultant, surveyor, research and development professor, lecturer, supervisor, superintendent, inspector or other allied title)
- ☐ Others (please specify) ______________

What type of organisation do you work in? *(Tick one box only)*

- ☐ Contractor
- ☐ Sub-contractor specialist
- ☐ Design and build contractor
- ☐ Consulting engineering/architectural/quantity surveying practice
- ☐ Mining/quarrying/aggregate production company
- ☐ Petroleum producer
- ☐ International/national authorities
- ☐ National/regional/local government
- ☐ Public utilities (electricity, gas, water, deck and harbour, other)
- ☐ Manufacturer
- ☐ Distributor/importer/agent
- ☐ Construction department of large industrial/Commercial concern
- ☐ Association/education establishment/research
- ☐ Construction equipment hire/rental company
- ☐ Project/construction management consultancy
- ☐ Others (please specify) ______________

What are the main activities of your organisation? *(Tick all that apply)*

Constructions of:	Manufacturer of:
☐ Roads/bridges	☐ Construction equipment
☐ Dams/reservoirs/irrigation	☐ Cement
☐ Harbours/offshore structures	☐ Other construction materials
☐ Foundations/tunnels	☐ Distribution
☐ Pipelines/refineries	☐ Construction equipment
☐ Structures/steel work	☐ Construction materials
☐ Building (commercial, industrial)	☐ Hire/rental of construction equipment
☐ Housing	☐ Design
☐ Construction management	☐ Earth-moving/open cast mining
☐ Deep mining	☐ Aggregate production

☐ Others (Please specify) ______________

Rate *(Please tick)*

- ☐ RM192.00 - 12 issues of JURUTERA
- ☐ RM96.00 - 6 issues of JURUTERA.
  Please specify the subscription month ______________
- ☐ RM128.00 - 4 issues of quarterly Journal
- ☐ RM80.00 - Annual IEM Directory (Hardcopy)
- ☐ RM65.00 - Annual IEM Directory (CD-ROM)

Terms and Conditions:

1) The subscription is to be prepaid.
2) Please make cheque payable to **Dimension Publishing Sdn Bhd.**
3) Subscriptions are not refundable.
4) Magazine/s will be sent to the mailing address given.
5) Students are entitled for a 20% discount from the above subscription rate.
6) Students must submit a photocopy of the student identification card together with the payment.
7) The above rate is inclusive of delivery charges and applicable in Malaysia only.
8) Additional delivery charges will apply to overseas subscribers.

For subscription enquiries, please contact 603-8070 9949 or email to subscription@dimensionpublishing.com.

dimensionpublishing
The Choice of Professionals

DIMENSION PUBLISHING SDN. BHD. (449732-T)
Suite 29, 3A Floor, IOI Business Park, 1 Persiaran Puchong Jaya Selatan, Bandar Puchong Jaya, 47100 Puchong, Selangor, Malaysia
Tel +603 8070 9949 **Fax** +603 8070 0047 **Website** www.dimensionpublishing.com

The Institution of Engineers, Malaysia
Bangunan Ingenieur, Lots 60/62, Jalan 52/4, Peti Surat 223 (Jalan Sultan), 46720 Petaling Jaya, Selangor Darul Ehsan
Tel : 03-79684001/2 **Fax :** 03-79577678 **E-mail** : sec@iem.org.my **IEM Homepage :** http://www.myiem.org.my

REFEREES FOR VETTING OF IEM PUBLICATIONS 2011/2012

The Standing Committee on Information and Publications is in the midst of compiling and updating the list of referees to assist in the vetting of articles received from members and non-members. The referees should preferably be at least Corporate Members of The Institution or graduates with higher degrees or with academics background.

The aim of appointing the referee is to ensure and maintain standard in the publication of the IEM quarterly Journal.

Members who are interested to be placed in the ***database of referees*** are to return the registration form to the IEM Secretariat, providing details of their degrees and particular expertise and experience in the engineering fields.

We need your generous services to look into the vetting and improving the IEM Journal articles received for Publications. An acknowledgement would be made at the end of the Sessions in either the Bulletin and Journal. Referees must be committed to return the papers within two weeks or a month from date of appointment made.

Thank you.

Principal Journal Editor
Standing Committee on Information and Publications

All submissions and correspondences are to be addressed to: -

JOURNAL EDITORIAL BOARD
Standing Committee on Information and Publications
The Institution of Engineers, Malaysia
Bangunan Ingenieur, Lots 60 & 62, Jalan 52/4
P.O. Box 223 (Jalan Sultan)
46720 Petaling Jaya, Selangor Darul Ehsan
Tel: 603-7968 4001/2 **Fax:** 603-7957 7678
E-mail: pub@iem.org.my/sec@iem.org.my
Website: http://www.myiem.org.my

DISCIPLINES / SUB-DISCIPLINES OF VETTER

Please tick (✓) the appropriate boxes.

- ❑ Agricultural
- ❑ Aerospace
- ❑ Aeronautical
- ❑ Chemical
- ❑ Civil
- ❑ Communication
- ❑ Electrical
- ❑ Electronics
- ❑ Environmental
- ❑ Industrial
- ❑ Manufacturing
- ❑ Marine
- ❑ Mechanical
- ❑ Mining
- ❑ Naval Architecture
- ❑ Petroleum
- ❑ Production
- ❑ Structural
- ❑ Others (*Please specify*) ____________________

AREAS OF INTEREST FOR VETTING OF PAPERS

Please tick (✓) the appropriate area of interest that you are able to vet the papers

- ❑ Acoustics
- ❑ Aerodynamics
- ❑ Air Conditioning
- ❑ Air Pollution Control
- ❑ Aircraft
- ❑ Airport Engineering
- ❑ Aluminum Design
- ❑ Arbitration
- ❑ Automation
- ❑ Automotive Engineering
- ❑ Biochemical Engineering
- ❑ Biotechnology
- ❑ Boiler Engineering
- ❑ Bridge Engineering
- ❑ Building Services
- ❑ Coastal Engineering
- ❑ Co-Generation
- ❑ Computer Engineering
- ❑ Concrete Design
- ❑ Concrete Technology
- ❑ Construction Management
- ❑ Control Engineering
- ❑ Drainage Engineering
- ❑ Dynamics Design
- ❑ Earthworks
- ❑ Edible Oil Refining
- ❑ Electrical Transmission
- ❑ Electrochemical
- ❑ Electrotechnology
- ❑ Energy Technology
- ❑ Engineering Education
- ❑ Environmental Engineering
- ❑ Fine Chemical
- ❑ Finite Element
- ❑ Fire Detection
- ❑ Fire Engineering
- ❑ Floods
- ❑ Food Processing
- ❑ Foundation Engineering
- ❑ Fuzzy Logic
- ❑ Gas Engineering
- ❑ Geotechnical
- ❑ Heat Exchanger
- ❑ Highway
- ❑ Hydraulics
- ❑ H.V. Electrical Distribution
- ❑ Industrial Engineering
- ❑ Industrial Transport
- ❑ Industrial Ventilation
- ❑ Information Technology
- ❑ Instrumentation
- ❑ Lighting System
- ❑ L.V. Electrical Distribution
- ❑ Management
- ❑ Mass Transit
- ❑ Manufacturing
- ❑ Mechanical Handling Equipment
- ❑ Metal Fabrication
- ❑ Metallurgy
- ❑ Micro Electronics
- ❑ Military Vehicles
- ❑ Mini Pressure Meters
- ❑ Mining Engineering
- ❑ Naval Architecture
- ❑ Navigation
- ❑ Oil and Gas Engineering
- ❑ Operation Research
- ❑ Palm Oil Industries
- ❑ Petrochemicals
- ❑ Petroleum Engineering
- ❑ Pharmaceuticals
- ❑ Piling
- ❑ Plumbing Engineering
- ❑ Pollution Control
- ❑ Ports and Harbor Engineering
- ❑ Power Electronics
- ❑ Power Generation
- ❑ Pressure Vessels
- ❑ Prestressed Concrete
- ❑ Project Management
- ❑ Public Administration
- ❑ Public Health Engineering
- ❑ Quarry Engineering
- ❑ Railways
- ❑ Reclamation Works
- ❑ Refrigeration
- ❑ Reinforced Concrete Beams
- ❑ Road Transport
- ❑ Robotics
- ❑ Roof Structures
- ❑ Room Temperature
- ❑ Safety Engineering
- ❑ Scaffolding Works
- ❑ Seepage
- ❑ Sewerage
- ❑ Shipbuilding
- ❑ Signal Processing
- ❑ Solar Energy Technology
- ❑ Steelworks Design
- ❑ Stream Turbine Power Plant
- ❑ Structural Analysis
- ❑ Structural Rehabilitation
- ❑ Survey Engineering
- ❑ Tailgates
- ❑ Telecommunication
- ❑ Thermal Engineering
- ❑ Timber Design
- ❑ Tool Engineering
- ❑ Transfer Tunnels
- ❑ Transportation Engineering
- ❑ Urban Planning
- ❑ Vehicles
- ❑ Vertical Transportation
- ❑ Waste Treatment
- ❑ Waste Water
- ❑ Water Resources Engineering
- ❑ Water Pollution Control
- ❑ Wind Engineering
- ❑ Others (*please specify*) ____________________

RESEARCHER / REVIEWERS DETAILS

Name : ____________________

Membership No. : ____________________ (*if applicable*)

Grade :
- ❑ Graduate
- ❑ Member
- ❑ Fellow
- ❑ Affiliate
- ❑ Non-member
- ❑ Others (*please specify*) ____________________

Qualifications : ____________________

Addresses

(*Office*) : ____________________

(*Residence*) : ____________________

Contact No.

Handphone : ____________________ **Office** : ____________________ **Residence** : ____________________

E-mail Address : ____________________

Please mail all correspondences to the below. Please tick (✓) the appropriate boxes.

Mail to : ❑ **Office** ❑ **Residence**

Brief biodata (not longer than 50 words) (*to be appended with this Reply Slip*).

Have you ever reviewed submissions for publication in any Journal(s) before?

❑ **Yes** ❑ **No**

If YES, name the Journal(s) : Do you have papers published in any Journal(s)?

❑ **Yes** ❑ **No**

If YES, name the Journal(s) : ____________________

Date : ____________________ **Signature** : ____________________

CALL FOR SUBMISSION OF IEM JOURNAL

The **IEM Journal** is an Engineering peer-reviewed journal published quarterly by The Institution of Engineers Malaysia. IEM Journal is dedicated to increasing the depth of research across all areas of engineering field: http://www.MyIEM.org.my/content/journal-122.aspx.

IEM Journal welcomes the submission of manuscripts that meet the general criteria of significance and scientific excellence in any of the Engineering field, and will publish:

- ❑ Original articles in basic and applied research
- ❑ Case studies
- ❑ Critical reviews, surveys, opinions, commentaries and essays

We invite you to submit your manuscript(s) in Times New Roman (12 point double spacing) to:

The Principal Journal Editor
Standing Committee on Information and Publications
The Institution of Engineers, Malaysia
Bangunan Ingenieur, Lots 60 & 62, Jalan 52/4
P.O. Box 223 (Jalan Sultan)
46720 Petaling Jaya, Selangor Darul Ehsan
Tel: 603-7968 4001/2 **Fax:** 603-7957 7678
E-mail: pub@iem.org.my/sec@iem.org.my **Website:** www.myiem.org.my

EDITORIAL ADVISORY BOARD FOR IEM JOURNAL (MAY 2011 TO MARCH 2013)

We are pleased to announce that the articles in the IEM Journals have been indexed by other organisation *i.e. Linda Hall Library of Science, Engineering and Technology, Kansas City.*

THE INSTITUTION OF ENGINEERS, MALAYSIA
Bangunan Ingenieur, Lots 60 & 62, Jalan 52/4, P.O.Box 223, (Jalan Sultan) 46720 Petaling Jaya, Selangor.
Tel: 03-7968 4001/4002 Fax: 03-7957 7678 E-mail: sec@iem.org,my Homepage: http://www.MyIEM.org.my